University of Alberta

Implications of rapid rotation for pulse profile models of millisecond-period X-ray pulsars

by

Coire Cadeau

A thesis submitted to the Faculty of Graduate Studies and Research in partial fulfillment of the requirements for the degree of Doctor of Philosophy

Department of Physics

Edmonton, Alberta
Spring 2007

Library and Archives Canada

Published Heritage Branch

395 Wellington Street
Ottawa ON K1A 0N4
Canada

Bibliothèque et Archives Canada

Direction du Patrimoine de l'édition

395, rue Wellington
Ottawa ON K1A 0N4
Canada

Your file Votre référence
ISBN: 978-0-494-29654-7
Our file Notre référence
ISBN: 978-0-494-29654-7

NOTICE:
The author has granted a non-exclusive license allowing Library and Archives Canada to reproduce, publish, archive, preserve, conserve, communicate to the public by telecommunication or on the Internet, loan, distribute and sell theses worldwide, for commercial or non-commercial purposes, in microform, paper, electronic and/or any other formats.

The author retains copyright ownership and moral rights in this thesis. Neither the thesis nor substantial extracts from it may be printed or otherwise reproduced without the author's permission.

AVIS:
L'auteur a accordé une licence non exclusive permettant à la Bibliothèque et Archives Canada de reproduire, publier, archiver, sauvegarder, conserver, transmettre au public par télécommunication ou par l'Internet, prêter, distribuer et vendre des thèses partout dans le monde, à des fins commerciales ou autres, sur support microforme, papier, électronique et/ou autres formats.

L'auteur conserve la propriété du droit d'auteur et des droits moraux qui protège cette thèse. Ni la thèse ni des extraits substantiels de celle-ci ne doivent être imprimés ou autrement reproduits sans son autorisation.

In compliance with the Canadian Privacy Act some supporting forms may have been removed from this thesis.

While these forms may be included in the document page count, their removal does not represent any loss of content from the thesis.

Conformément à la loi canadienne sur la protection de la vie privée, quelques formulaires secondaires ont été enlevés de cette thèse.

Bien que ces formulaires aient inclus dans la pagination, il n'y aura aucun contenu manquant.

Canada

The Sprawl's geodesics were lightening into predawn grey as Case left the building... Vibrations beneath his feet as a train hissed past. Sirens dopplered in the distance.

—William Gibson, *Neuromancer*

To my family, Mom, Dad, and Charmaine,
and to Dale,
with love.

Abstract

The rapid rotation of recycled neutron stars in accretion-powered millisecond-period X-ray pulsars has important consequences for models of their pulsed emission, and by extension, the analysis of observations of these objects. We begin by considering the problem of calculating the time-varying bolometric flux arising due to emission from a bright spot on the surface of a rapidly rotating neutron star, with rotational period on the order of a millisecond. We restrict to the case of isotropic emission from an infinitesimal emission zone, but carry out the calculations with sufficient generality to incorporate a precisely solved spacetime metric and stellar structure. The geodesic equation is integrated numerically.

Using the computer code developed for this work, we investigate the effect that commonly-used simplifying approximations have on the shape of the pulse profile compared to the full calculation. In particular, we consider the effect of neglecting the phase-dependent travel time of photons, approximating the exterior metric as either Schwarzschild or Kerr, and neglecting the rotation-induced oblateness of the neutron star.

We also consider the consequences that result when approximate pulse profiles are used to obtain neutron star parameters such as mass, radius, emission inclination, and observer inclination via least squares fitting. Specifically, we look at fitting light curves calculated using the Schwarzschild metric and a spherical star to a light curve calculated using a precisely-solved metric and stellar structure. We are able to conclude that, in an idealised case where there is no random noise component and all light curves are for bolometric fluxes from isotropic emission, neglecting photon times-of-flight or stellar oblateness in model light curves used for fitting can introduce errors at the level of several tens of percent on the determination of mass and radius individually. However, these errors will often offset each other such that the fitted parameters will yield better determinations of the compactness.

To facilitate the inclusion of oblateness effects in other codes, we give a single polynomial which describes the oblate shape of stars for a range of masses and rotation periods for three separate equations of state.

Acknowledgements

This work would not have been possible without the support, guidance, and friendship I have received from many people during my time in the Physics Department, and throughout my entire education.

I am grateful to my supervisor, Dr. Sharon Morsink, for her advice, generous support, and patience during my studies. She introduced me to neutron star physics, and gave timely advice on questions I should address during the development of this work. The result has been a fruitful and engaging programme of research. I am especially appreciative of having been afforded the opportunity to concentrate on this work full-time during many academic terms, and for annual travel opportunities, all of which was made possible by a grant she held from the Natural Sciences and Engineering Research Council of Canada.

I have benefited from substantial collaboration with Dr. Denis Leahy in the Department of Physics and Astronomy at the University of Calgary, which resulted in the main conclusions arrived at in this dissertation. I learned a lot from our discussions, and looked forward to the meetings we had a few times per year.

I am thankful for the advice I have received from the members of my committee on the text of my dissertation, and for their guidance during my studies.

I have enjoyed camarderie with many fellow students at the University, both within the Department and outside it. I'm also glad that I've been able to stay in touch with my friends Jade, Jeff, and Michelle, who live in Ontario. My longtime friend Jade carefully read the prose of Chapter 1 and suggested numerous improvements. The friends and acquaintances I have made in the downtown Edmonton community, especially at Our Urban Eden community garden on Bellamy Hill, have made my day-to-day life colourful.

I have dedicated this work to those upon whom I have drawn most heavily for personal support and encouragement. The love of my family, Mom, Dad, and Charmaine, inspires me and helped make this possible. Finally, Dale's love and friendship brightened my time in Edmonton. I am thankful that she shared her family with me, and for all that she's done to help me along.

Table of Contents

1 Introduction **1**
- 1.1 Neutron stars . . . 2
- 1.2 X-ray binaries . . . 4
- 1.3 Pulsars and accretion-powered recycling . . . 6
  - 1.3.1 Introduction and observational history . . . 6
  - 1.3.2 LMXBs and accretion-induced recycling . . . 10
  - 1.3.3 Evolution of X-ray binaries . . . 14
  - 1.3.4 X-ray pulsation mechanisms . . . 18
- 1.4 Organisation of the dissertation . . . 25
  - 1.4.1 Notes on the text . . . 26

2 Calculating the light curve **27**
- 2.1 Introduction . . . 27
- 2.2 Stationary axisymmetric spacetimes in general relativity . . . 29
  - 2.2.1 Special cases: Schwarzschild & Kerr metrics . . . 31
- 2.3 Null geodesics of the stationary axisymmetric spacetime . . . 33
  - 2.3.1 Equations of motion . . . 33
  - 2.3.2 Initial conditions for null geodesics . . . 35
  - 2.3.3 Redshift . . . 39
  - 2.3.4 Zenith angle . . . 40
- 2.4 Calculation of light curve . . . 44
  - 2.4.1 Solid angle . . . 44
  - 2.4.2 Calculation of light curve including arrival time effects . . . 47
- 2.5 Calculating the light curve in the Schwarzschild metric . . . 54
  - 2.5.1 The Doppler factor and times-of-flight in Poutanen and Gierliński (2003) . . . 60

3 Numerical procedure **62**
- 3.1 Introduction . . . 62
  - 3.1.1 Details of metric and stellar surface descriptions . . . 63
- 3.2 Integration of rays . . . 64
  - 3.2.1 Calculating the time-of-flight . . . 65
- 3.3 Interpolation of rays . . . 66
  - 3.3.1 Shepard's Interpolation of Scattered Data . . . 67

3.4 Calculating the light curve 70
3.5 Verifying the implementation 72
3.5.1 Checking $\bar{r}_s(\theta)$ 73
3.5.2 Comparison with Schwarzschild light curves 73
3.5.3 Checking Carter's constant 81
3.5.4 Checking time-of-flight & future improvements 81

4 Results **83**
4.1 Introduction 83
4.2 Choice of neutron star models 87
4.3 The effect of neglecting time-of-flight 88
4.3.1 Introduction 88
4.3.2 Equations of motion 90
4.3.3 Times-of-flight 91
4.3.4 Redshift 93
4.3.5 Angles between Photons 95
4.3.6 Outline of Numerical Method 96
4.3.7 Light curve calculations 99
4.3.8 Fit results 101
4.3.9 Conclusion 107
4.4 The applicability of other approximate techniques 108
4.4.1 Methods comparison 109
4.4.2 Fits to obtain parameters 118
4.4.3 Conclusion 121
4.5 Modelling oblateness: Model of Schwarzschild radius 126
4.5.1 Adaptation of Schwarzschild light curve calculation to incorporate oblateness 129

5 Conclusion **136**

References **140**

List of Tables

1.1 The seven known accreting millisecond-period X-ray pulsars 10

2.1 Christoffel symbols for the stationary axisymmetric spacetime. . . . 36

4.1 Neutron Star Models with Mass = $1.4\,M_\odot$ 88
4.2 Fits to exact 1-D light curves using an approximate technique 103
4.3 True values of $R(\theta_e)$, $GM/(c^2R(\theta_e))$ for fitted light curves 119
4.4 Fits to light curves using SS method to extract parameters, part 1 . 122
4.5 Fits to light curves using SS method to extract parameters, part 2 . 123
4.6 Quadratic fit to oblateness coefficients 127

List of Figures

2.1 Initial conditions for null geodesics originating from an oblate star . 38
2.2 Solid angle projection is calculated for an infinitesimal region 45
2.3 Description of an extended emission region 49
2.4 Projection of emitting region onto observer's sky in Schwarzschild case 55

3.1 Comparing direct Schwarzschild calculation of bolometric flux to SS approximation in the general code 75
3.2 Comparison of $(1+z)$ in spherical and oblate codes 76
3.3 Comparison of $\mathrm{d}t_r/\mathrm{d}t_e$ in spherical and oblate codes 77
3.4 Comparing $k\mathrm{d}\Omega_{\mathrm{SS}}/\mathrm{d}\Omega_{\mathrm{OS}}$ with $\cos\alpha_{\mathrm{SS}}/\cos\alpha_{\mathrm{OS}}$ 79
3.5 Checking constantness of $\bar{r}_f^2\mathrm{d}\Omega/\cos\alpha$ 80
3.6 Verification of time-of-flight via its numerical derivative 82

4.1 Angles in the simplified 1-D case 91
4.2 Bending angle $\psi(b)$ and $\mathrm{d}\psi/\mathrm{d}b$ for photons 92
4.3 Times-of-flight as a function of bending angle 94
4.4 Light curves for 1-D emitting region 100
4.5 Distortion introduced by not including all time-of-flight effects . . . 102
4.6 Fitted 1-D light curves for EOS A models 104
4.7 Fitted 1-D light curves for EOS L models 105
4.8 Contours of sum of squared differences for fit 106
4.9 Oblateness becomes important as $\Omega_\star$ increases 110
4.10 Qualitative changes in lightcurves when oblateness is accounted for . 112
4.11 Different rays reach the observer in oblate calculation 113
4.12 Exact method allows for rays with $\dot{\bar{r}}_i < 0$ 114
4.13 Determining the worst-case scenario for approximate calculations . . 115
4.14 Example of worst- and best-case scenarios for approximate calculations 116
4.15 Comparing light curves with fitted parameters to true values 124
4.16 Quadratic polynomial models for oblateness coefficients a_{2n} 128
4.17 Leading truncation term in polynomal oblateness model, a_6 129
4.18 Oblateness model in worst-performing case 130
4.19 Incorporating oblateness model into calculations 134

Chapter 1

Introduction

The rapid rotation of neutron stars in millisecond-period X-ray pulsars has important consequences for models of the pulsed emission, and by extension, the analysis of observations of these objects. Motivated by the "classical" slowly-rotating X-ray pulsars, models of pulsed X-ray emission from near the surfaces of neutron stars have been pursued since the 1980s. The earliest treatment of this problem did not account for the effect of gravity on the path followed by the emitted light (Wang and Welter, 1981), but a formalism set out by Pechenick *et al.* (1983), which included gravitational effects, established the basic framework used in most treatments of this problem even today. Such models yielded a tool with which to analyse X-ray pulsars, since by comparing calculations of model light curves to observations, it became possible to draw conclusions about the properties of the underlying neutron star and the emission mechanisms. These models were originally developed to describe situations where the rotational period of the star was on the order of several seconds, which for typical neutron star radii ~ 10 km imply non-relativistic velocities at the surface of the star, negligible light-crossing times compared to the rotational period, and insignificant rotational effects on the stellar structure. In this situation, a number of simplifications result. For example, the "light bending" caused by the neutron star can be included by assuming that the star is spherically symmetric, and that the exterior spacetime is Schwarzschild. Additionally, the Doppler boosting of photon energies, and the phase-dependent times-of-flight of photons can also be neglected. With the recent discovery of millisecond-period X-ray pulsars, of which the 2.5 ms pulsar SAX J1808.4-3658 was the first example (Wijnands and van der Klis, 1998), a natural question arises: to what extent can the methods developed for longer-period X-ray pulsars be applied to this new class of objects? This dissertation seizes upon answering this question from two points

of view: from the modelling perspective, and from the data analysis perspective. Although a precise treatment of millisecond X-ray pulsars is more complicated than for the classical X-ray pulsars, this work argues the necessity of incorporating new effects in models of millisecond X-ray pulsars, and concludes with a suggestion of a *practical* way forward. In this chapter, the millisecond-period X-ray pulsars which motivated this work are described and placed in a broader context. The chapter concludes with an outline of the remainder of the dissertation.

1.1 Neutron stars

Neutrons were discovered by Chadwick (1932), who was awarded the 1935 Nobel Prize in Physics for the discovery. The possibility of neutron stars as the remnant of a massive star which had exhausted its nuclear fuel and exploded as a supernova was first proposed by Baade and Zwicky (1934) (also see Oppenheimer and Volkoff (1939) for early theoretical work). Neutron stars represent a middle ground between the endpoint of massive stars with initial masses of $\gtrsim 25\,M_\odot$, which will collapse to form black holes at the end of their lives, and lighter stars with initial masses $\lesssim 8\,M_\odot$, which end their lives as white dwarfs (Tauris and van den Heuvel, 2006). The first observational evidences of these objects, first as members in some X-ray binaries, and shortly thereafter as pulsars, were not discovered until more than three decades later.

An interesting counterpoint to this story is the case of white dwarf stars (for example, Sirius B, a white dwarf in a binary) which were known by observation to have masses $\sim M_\odot$, and luminosities $\sim L_\odot/300$, but radii $\sim R_\oplus \approx 10^{-2}\,R_\odot$. Eddington (1924) pointed out that Sirius B was incredibly dense, but paradoxically "much too faint for its mass," and it was unclear how such a star could support itself against gravity. It wasn't until the development of Fermi-Dirac statistics (Dirac, 1926), that the eventual resolution of this problem by Fowler (1926) was possible. White dwarfs are now known to be supported by electron degeneracy pressure.

The name "neutron star" is appropriately given to the remnants of massive stars formed during the collapse of their iron cores, but which are too light to collapse to black holes, since the matter passes through a phase where it becomes dense enough that the inverse beta decay reaction

$$e^- + p \rightarrow n + \nu \tag{1.1}$$

converts much of the matter to neutrons, roughly in the ratio $n_e : n_p : n_n = 1 : 1 : 8$

(Shapiro and Teukolsky, 1983). This is not the complete story, however, as the core continues to collapse reaching densities ranging from several to tens of times that of ordinary nuclear matter ($\rho_{\rm nuc} \sim 10^{14}\,{\rm g/cm^3}$), at which point degeneracy pressure acts to arrest the core collapse. The final state of matter comprising the core of a neutron star is poorly understood, since at the implied distance scale the strong nuclear force becomes important. As a result, neutron degeneracy pressure alone does not determine the state of matter, and a full treatment would require a better understanding of multibody processes in quantum chromodynamics (QCD). It is clear that the detailed equation of state of this matter, specified by $p(\rho)$, determines the mass-radius relation obeyed by neutron stars. Shapiro and Teukolsky (1983) and Glendenning (2000) are texts which include a thorough discussion of neutron star equations of state. Modern candidate equations of state, including some strange quark matter (SQM) models, are discussed by Lattimer and Prakash (2001), while older candidate equations of state were catalogued by Arnett and Bowers (1977). Lattimer and Prakash (2004) provide a short overview on neutron star structure and equations of state. One potential application of neutron star observations is the empirical constraint of the state of matter at these densities. There are now also terrestrial experiments that can probe these densities, for example the Relativistic Heavy Ion Collider (RHIC) at Brookhaven National Laboratory (BNL) in New York, USA (Ludlam and McLerran, 2003). Experiments at RHIC may also help to constrain the state of matter at these densities. However, it should be noted that these experiments primarily probe the physics of hot ($\sim 10^{12}\,{\rm K}$) dense matter, and in particular the state of hot quark-gluon plasma and the phase transition to hadronic matter as the plasma cools (Schiffer *et al.*, 1999). In old neutron stars, the temperatures are much lower ($\sim 10^5$–$10^6\,{\rm K}$) than the temperatures probed by RHIC (Lattimer and Prakash, 2004). For neutron star equations of state, the temperature dependence is usually left out since the fluid is assumed to be in thermal equilibrium, and at these temperatures the neutrons have energies below the Fermi energy.

Typical models of neutron stars will have masses on the order of $1.4\,M_\odot$ and radii on the order of 10 km, or a few times the Schwarzschild radius, so that their gravitational field requires a general relativistic description. In the sections that follow, we discuss the two main astrophysical manifestations of neutron stars: a class of X-ray binaries, and radio pulsars. Then we consider a category of neutron stars which not only have relativistic gravitational fields, but are also rotating at relativistic speeds; these are the main class of neutron stars which are under

consideration in this dissertation.

1.2 X-ray binaries

The observation of X-rays from cosmic sources must be carried out above the atmosphere. Some of the earliest experiments took place using captured V-2 rockets fitted with proportional counters launched in White Sands, New Mexico, USA, in 1949. The first extra-solar cosmic X-ray source, Sco X-1, was discovered by Riccardo Giacconi in 1961 during an attempt to observe solar X-rays reflected by the moon (Giacconi *et al.*, 1971). Today, the field of X-ray astronomy represents a significant fraction of the total endeavour in physics by humankind. Consider that in 2002, Giacconi was awarded 1/2 of the Nobel Prize for Physics "for pioneering contributions to astrophysics, which have led to the discovery of cosmic X-ray sources." In the same year, some 20% of the papers published in The Astrophysical Journal, Monthly Notices of the Royal Astronomical Society, and Astronomy and Astrophysics contained the word "X-ray" in their abstract (Barcons and Negueruela, 2003). Using space-based instruments, a variety of astrophysical phenomena are visible in the X-ray sky, among them active galactic nuclei (AGNs) and clusters of galaxies, and within our Galaxy (and, increasingly, elsewhere in the local group) X-ray binaries and supernova remnants. The brightest class of these objects, of which Sco X-1 is an example, are the X-ray binaries, which consist of a neutron star or black hole accreting matter from a companion star (White *et al.*, 1995). A similar situation can occur for accretion onto white dwarfs, but these objects are generally weaker X-ray sources, and are usually referred to as cataclysmic variables.

If we denote the radius of the compact object as $R = \tilde{r}R_s$, where the gravitational radius $R_s = 2GM/c^2$, then the gravitational potential energy liberated by an infalling nucleon of mass $m_p \approx 940\,\mathrm{MeV}/c^2$ is

$$\Delta E = \frac{1}{2\tilde{r}}(c^2 m_p), \tag{1.2}$$

in the non-relativistic limit $1/\tilde{r} \ll 1$. For an order-of-magnitude calculation, the typical radii of the neutron stars and black holes have $1 \leq \tilde{r} \leq 5$, so that a single infalling nucleon must liberate on the order of several times 10^{-1} GeV on its journey into the compact object's gravitational well. This is about ten times more energy per nucleon than can be achieved by nuclear fusion: the binding energy per nucleon for stable nuclei is at most about 9 MeV (for a ^{56}Fe nucleus). The typical lumi-

nosities of X-ray binaries are within an order of magnitude of $10^{37}\,\mathrm{erg\,s^{-1}}$ (White *et al.*, 1995), or around one thousand times the luminosity of the Sun. Clearly accretion onto compact objects is a potent source of astrophysical energy, a fact first realised by Salpeter (1964), Zel'dovich (1964), and Zel'dovich and Novikov (1964) with application to quasars and AGNs (accreting supermassive black holes), and by Zel'dovich and Guseynov (1966), Novikov and Zel'dovich (1966), and Shklovskii (1967) in the context of X-ray binaries (Tauris and van den Heuvel, 2006).

Continuing this order-of-magnitude energetics calculation, the typical luminosity of X-ray binaries is powered by accretion rates $\dot{M}$ within an order of

$$\begin{aligned}\dot{M} &\approx (L/10^{37}\,\mathrm{erg\,s^{-1}}) \times (10^{37}\,\mathrm{erg/s}) \times (6.24 \times 10^{5}\,\mathrm{MeV/erg}) \times (3.16 \times 10^{7}\,\mathrm{s/a}) \\ &\quad \times ((2\tilde{r}/940)\,\text{accreted nucleons/MeV}) \times (8.35 \times 10^{-58}\,M_{\odot}/\text{nucleon}) \\ &\approx \left(3.5 \times 10^{-10}\,M_{\odot}/\mathrm{a}\right)\left(\frac{L}{10^{37}\,\mathrm{erg\,s^{-1}}}\right)\tilde{r}. \end{aligned} \tag{1.3}$$

This is approximately an order of magnitude smaller than the Eddington rate. The Eddington rate is defined as the point at which the radiation pressure of the accretion-powered luminosity disrupts the infalling matter stream (Shapiro and Teukolsky, 1983). To calculate it, one balances the force generated by radiation pressure on electrons with the gravitational force on the infalling protons, which gives the Eddington luminosity

$$L_{\mathrm{Edd}} = \frac{4\pi GM}{\sigma_T}(m_p c) = \left(1.8 \times 10^{38}\,\mathrm{erg/s}\right)\left(\frac{M}{1.4\,M_{\odot}}\right), \tag{1.4}$$

where $\sigma_T = 0.66 \times 10^{-24}\,\mathrm{cm^2}$ is the Thomson cross section for the scattering of photons by electrons. The Eddington accretion rate $\dot{M}_{\mathrm{Edd}}$ is the accretion rate which would yield this luminosity; applying Equation 1.3 yields

$$\dot{M}_{\mathrm{Edd}} = \left(1.5 \times 10^{-8}\,M_{\odot}/\mathrm{a}\right)\left(\frac{R}{10^{6}\,\mathrm{cm}}\right). \tag{1.5}$$

In practise, X-ray binaries are classified according to the mass of the companion star: high-mass X-ray binaries (HMXBs) have a companion star with mass $M_c \gtrsim 10M_{\odot}$; low-mass X-ray binaries (LMXBs) have a companion star with mass $M_c \lesssim 1M_{\odot}$ (Verbunt and van den Heuvel, 1995). Determining which class a given X-ray binary falls into usually relies on one or more of the following (White *et al.*, 1995; Lewin *et al.*, 1995; Verbunt and van den Heuvel, 1995):

Identification of companion In LMXBs, the donor star is typically optically

faint (if it is observable at all), while in HMXBs the optical luminosity of the companion star dominates the total emission from the system. The donor star in an HMXB is typically two orders of magnitude brighter than the donor in an LMXB, and can often be identified.

Luminosities The ratio of X-ray to optical luminosities in LMXBs ranges from $\sim 10^2$ to $\sim 10^4$; for HMXBs the ratio ranges from $\sim 10^{-3}$ to $\sim 10^1$.

X-ray spectra The X-ray spectra of LMXBs are typically softer than those of HMXBs.

Bursting behaviour LMXBs might exhibit X-ray bursts, which are sudden rises in the X-ray activity which fades away over several minutes.

Orbital period LMXBs will typically have orbital periods ranging from minutes to several days, while HMXBs typically do not have orbital periods less than 12 hours.

In LMXBs, the accretion typically occurs via Roche lobe overflow, where matter from the donor star is driven through the inner Lagrange point, and enters an accretion disk around the accreting object. In HMXBs, the orbit is usually wide and the donor star does not overflow its Roche lobe. Instead, matter is captured from the donor star's stellar wind. The typical lifetime of an HMXB is on the order of 10^5–10^7 a, which is determined by the lifespan of the high-mass donor. LMXBs have lifetimes about two orders of magnitude larger, 10^7–10^9 a, which is determined by the mass-transfer process (Psaltis, 2006).

1.3 Pulsars and accretion-powered recycling

1.3.1 Introduction and observational history

Rotating neutron stars with relatively strong magnetic fields reveal themselves as pulsars, the hallmark of which is the extremely regular pulsation of electromagnetic radiation, especially in the radio part of the spectrum. The first pulsar was discovered by Hewish *et al.* (1968), and Anthony Hewish was awarded half of the 1974 Nobel Prize in Physics "for his decisive role in the discovery of pulsars." Initially it was not clear what mechanism was producing the pulsed radiation, and several proposals were made that it was the signature of radial pulsations of a degenerate star. One such model was advanced by Israel (1968), who posited that the pulsed radiation was the signature of a neutron star on the brink of collapsing to

a black hole. In this model, a thin hydrogen-rich envelope collected on the surface of such a neutron star, which forced the neutron star to begin collapsing. In so doing, the accreted envelope would heat up—perhaps by nuclear burning—enough to blow off enough of the accreted matter to stop the collapse. Then the neutron star core would snap back, propelling the remaining matter away from the star at relativistic velocities, causing synchrotron radiation. In this model, the period of the pulsations was related to the time interval required for the envelope to re-settle on the neutron star, beginning the whole process again. Gold (1968) was the first to suggest the currently accepted model, where the rotation of a magnetised neutron star powers synchrotron emission from a sparse plasma located near the star's light cylinder (i.e., the radius at which co-rotation with the star requires travel at the speed of light). The pulsed radio emission is interpreted as a directed beam of radiation pointing in the direction of the star's magnetic field, which is not aligned with its spin axis. As a result, the radiation beam periodically cuts across the line-of-sight as the star rotates. There are now approximately 1700 known *radio* pulsars (Lorimer, 2005). Gold (1968) hypothesised that there should be a measurable period derivative resulting from the conversion of rotational energy to electromagnetic radiation due to magnetic dipole radiation, and an analysis of this suggestion was first carried through by Pacini (1968). This led directly to the standard model of dipole braking by pulsars (Gunn and Ostriker, 1969, 1970): as newly-born isolated pulsars age, the period of the pulsations gradually lengthens. Measurements of the period derivative $\dot{P}$ can be used to infer the magnetic field strength of the neutron star by attributing the lost rotational energy of the neutron star to dipole radiation. One can obtain the surface magnetic field strength $B \propto \sqrt{P\dot{P}}$ and a characteristic age $\tau_c = P/(2\dot{P})$. The derived magnetic field for typical radio pulsars is $\sim 10^{12}$ G, with characteristic age $\sim 10^7$ a (Lorimer, 2005).

It was the discovery of the 1.6 ms radio pulsar PSR 1937+21 in 1982 (Backer *et al.*, 1982) which pointed to the existence of a new class of much older pulsars with weak magnetic fields. In a review of millisecond pulsars, Bhattacharya (1995) points out that these new objects were immediately thought to be old neutron stars which had been "spun up" by accreting mass and angular momentum from a companion star (Alpar *et al.*, 1982). This was not a new idea, as the Hulse-Taylor binary pulsar PSR 1913+16 (Hulse and Taylor, 1975) had been discovered some eight years prior, and it was conjectured to be a highly-evolved binary system (Flannery and van den Heuvel, 1975; Smarr and Blandford, 1976). However, the first millisecond pulsar was the first evidence that such neutron stars could be

spun up to large fractions of their theoretical maximum frequency. One problem with this picture was that there was no evidence for a companion star in this new system and so if it had evolved from a binary, it must have lost its companion in some way. Soon after this discovery, the 6 ms *binary* radio pulsar PSR 1953+29 was discovered (Boriakoff *et al.*, 1983) which solidified the case for the "recycling" of old neutron stars by capturing angular momentum in binary systems (Savonije (1983); Paczyński (1983); and more recently, Tauris and Savonije (1999)). It is possible that these recycled pulsars eventually destroy their companions by electromagnetic radiation. The "evaporation" of the companion by electromagnetic radiation has been observed in the famous 1.6 ms "Black Widow" pulsar, PSR 1957+20 (Fruchter *et al.*, 1988). To date, the fastest known radio pulsar has $P = 1.4$ ms, which was discovered by a radio survey of the globular cluster Terzan 5 (Hessels *et al.*, 2006). Today there are approximately 160 known recycled radio pulsars; of these, the typical derived fields and ages are $B \sim 10^8$ G and $\tau_c \sim 10^9$ a (Lorimer, 2005).

Upon the discovery of the first millisecond radio pulsar, there were perhaps 20 or so known X-ray pulsars in X-ray binaries. These are systems that exhibit pulsations in the X-ray flux corresponding to the rotation rate of the underlying neutron star. The first X-ray pulsar to be discovered was Cen X-3, a 4.8 s pulsar in a 2.1 d orbital period HMXB (Giacconi *et al.*, 1971). Most known X-ray pulsars tended to occur in HMXBs, although not exclusively so. For example, the 1.24 s X-ray pulsar Her X-1 was discovered in 1972 (Tananbaum *et al.*, 1972) and is one of approximately five examples of X-ray pulsars in low (or intermediate) mass X-ray binaries (Psaltis, 2006). If it was true that recycled radio pulsars were formed by the evolution of neutron stars in LMXBs, then it was a puzzle why there were no known millisecond-period X-ray pulsars, a situation which continued for some time in spite of several efforts made to search for them (among them Leahy *et al.* (1983), Mereghetti and Grindlay (1987), Wood *et al.* (1991), and Vaughan *et al.* (1994), as is pointed out by Wijnands and van der Klis (1998)).

The discovery in 1996 (Strohmayer *et al.*, 1996) of coherent millisecond-period brightness oscillations during Type I X-ray bursts resolved the long-standing problem of the absence of evidence for accretion-induced spin-up of neutron stars in LMXBs (Strohmayer and Lee, 1996). Type I X-ray bursts are thermonuclear flashes occurring on the surface of weakly-magnetic accreting neutron stars in LMXBs, and the frequency of the brightness oscillations is understood as arising from rotational modulation of a hot spot on the surface of the neutron star. Bursts are discussed in more detail in Section 1.3.4. The discovery and study of these burst oscillations

was made possible after the launch of the Rossi X-ray Timing Explorer (RXTE) satellite in December 1995 which had unprecedented sensitivity, timing resolution, and pointing flexibility (Bradt *et al.* (1993); also see Jahoda *et al.* (1996) which discusses the on-board proportional counting array (PCA)).

It wasn't until 1998 that the first persistent millisecond-period X-ray pulsar, SAX J1808.4-3658, was discovered (Wijnands and van der Klis, 1998) in a 2.01 h orbital period LMXB (Chakrabarty and Morgan, 1998). This provided further evidence of the evolutionary link to the old millisecond radio pulsars. While RXTE observations revealed the pulsar nature of SAX J1808.4-3658, its initial identification was made following an observation in September 1996 by the Wide Field Cameras on board BeppoSAX, which observed two type I X-ray bursts. This source was classified as an LMXB at a distance of approximately 4 kpc (in 't Zand *et al.*, 1998). There are now seven known millisecond X-ray pulsars, which are listed in Table 1.1 with their rotational and orbital periods. It is difficult to find millisecond-period X-ray pulsars and it is still a puzzle how these seven examples differ from other LMXBs which do not exhibit persistent X-ray pulsations. The review by Psaltis (2006) (also see Chakrabarty (2005)) discusses the two main suggestions that have been made to resolve this problem, but these proposals have significant shortcomings. First, upon the discovery of SAX J1808.4-3658 it was suggested that perhaps the detection of pulsations was made possible by viewing SAX J1808.4-3658 at small inclinations to the plane of the binary, preventing the X-ray pulses from being blocked by the accretion flow (Psaltis and Chakrabarty, 1999). This seems less likely now with the discovery of more millisecond X-ray pulsars, and with the detection of an arrival time modulation in all of these systems. Second, it was suggested that since these pulsars all have relatively low accretion rates, that perhaps in the non-pulsing LMXBs the accretion rates are high enough to make the magnetic field dynamically unimportant (Cumming *et al.*, 2001); see Equation 1.9 and the related discussion below for an illustration of the importance of the accretion rate. If this was the case, the accreted matter would not be funnelled to polar caps on the surface, and persistent pulsed X-rays would not be detected. However, the similarity between these pulsars and non-pulsing LMXBs in terms of their spectra and aperiodic variability makes it hard to accept this suggestion as the resolution of this puzzle (Psaltis, 2006).

In the sections that follow, it is shown in more detail how LMXBs provide the correct conditions for recycling of neutron stars. Then some remarks about the population of LMXBs are in order, as the evolutionary history of these systems has

Name	Ω_* (Hz)	T (ms)	Orbital period (hr)	Selected references to observations
SAX J1808.4-3658	400	2.5	2.01	Wijnands and van der Klis (1998), Chakrabarty and Morgan (1998), Papitto *et al.* (2005)
XTE J1751-305	435	2.3	0.7	Markwardt *et al.* (2002)
XTE J0929-314	185	5.4	0.73	Galloway *et al.* (2002)
XTE J1807-294	191	5.2	0.67	Markwardt *et al.* (2003b), Markwardt *et al.* (2003a)
XTE J1814-338	314	3.2	4.28	Markwardt and Swank (2003) Markwardt *et al.* (2003c)
IGR J00291+5934	599	1.67	2.46	Markwardt *et al.* (2004), Galloway *et al.* (2005)
HETE J1900.1-2455	377.3	2.65	1.39	Kaaret *et al.* (2006)

Table 1.1: The seven known accretion-powered millisecond-period X-ray pulsars with their spin and orbital periods in the order of their discovery.

not been firmly established.

1.3.2 LMXBs and accretion-induced recycling

In neutron star LMXBs, a neutron star accretes matter from a low mass companion which is overflowing its Roche lobe. The infalling matter forms an accretion disk where the matter orbits at the local Keplerian speed with a relatively small inward drift velocity. Angular momentum and approximately half of the available accretion energy is dissipated in the disk through stresses arising from turbulent flow. The basic picture of *thin* accretion disks was pioneered by Shakura and Sunyaev (1973) and Lynden-Bell and Pringle (1974). The central dynamical issue in accretion disk flows is the transport of angular momentum, but the thin disk models do not specify the mechanism for this—its effect is inserted in an *ad hoc* manner. More recently, a promising candidate for the angular momentum transport mechanism, known as the weak-field magnetorotational instability (MRI), was proposed by Balbus and Hawley (1991). This mechanism is driven by a magnetic field which is too weak to affect the orbital dynamics of the matter, but the disk shear winds up the field and transports angular momentum outwards. Reconnection limits the field growth and results in dissipation (King, 2006). Currently, there are efforts to use 3-D magnetohydrodynamics codes to model the turbulent flow in accretion disks (e.g., Miller and Stone (2000), Hawley and Krolik (2001), Krolik and Hawley (2002), and Hirose *et al.* (2006)). A pedagogical treatment of accretion physics is Frank *et al.* (2002); reviews of accretion disk physics include King (1995), Balbus and Hawley

(1998), and King (2006).

The accreting matter eventually reaches the inner edge of the disk where the flow is disrupted by the magnetic field of the star, and the infalling matter follows the magnetic field lines down to the neutron star's surface. The difference between the Keplerian orbital frequency at the inner edge of the disk and the star's spin frequency determines the fate of the accreting matter: if the orbit at the inner edge of the disk is faster than the star, the matter binds to the field lines and a magnetic torque acts to spin up the star (Ghosh and Lamb, 1978). On the other hand, if the orbit at the inner edge of the disk is slower than the star, a torque acts to spin down the star. In this situation the infalling matter may be flung away from the star since it cannot penetrate the centrifugal barrier. This is called the "propeller mechanism" after Illarionov and Sunyaev (1975). Over time, one expects the frequency of the inner edge of the disk and the neutron star to equalise. To calculate this equilibrium frequency, one first requires an estimate of where the magnetic field disrupts the disk; this is known as the Alfvén radius R_A. Although we are considering disk accretion, estimates of R_A are usually obtained by considering spherical accretion onto the star, and obtaining the point at which the ram pressure of the fluid flow is equalised by the magnetic pressure on the infalling matter (Davidson and Ostriker (1973), but we have referred to a textbook replication of this argument in §6.3 of Frank *et al.* (2002)). The ram pressure is ρv^2, where ρ is the mass density of the fluid, and at the inner edge of the disk the velocity $v \approx v_{\rm ff} = (2GM/r)^{1/2}$, the free-fall velocity. For spherical accretion, we have

$$\rho v = \frac{\dot{M}}{4\pi r^2}, \tag{1.6}$$

so that the ram pressure at radius r is

$$p_{\rm ram} = \rho v^2 = \frac{(2GM)^{1/2}\dot{M}}{4\pi r^{5/2}}. \tag{1.7}$$

Assuming a dipole field, the magnetic field density B at radius r is roughly $\sim \mu/r^3$, where μ is the magnetic dipole moment of the star. It is related to the surface field density and stellar radius by $\mu = B_\star R_\star^3$. The magnetic pressure exerted on the infalling plasma is

$$p_{\rm mag} = \left[\frac{4\pi}{\mu_0}\right]\frac{B^2}{8\pi} = \left[\frac{4\pi}{\mu_0}\right]\frac{\mu^2}{8\pi r^6}. \tag{1.8}$$

The pressures equalise at R_A, giving

$$R_A = (2.6 \times 10^6\,\mathrm{cm}) \left(\frac{\dot{M}}{\dot{M}_{\mathrm{Edd}}}\right)^{-2/7} \left(\frac{M}{1.4\,M_\odot}\right)^{-1/7} \left(\frac{B_\star}{10^9\,\mathrm{G}}\right)^{4/7} \left(\frac{R_\star}{10^6\,\mathrm{cm}}\right)^{10/7}, \tag{1.9}$$

where we have used Equation 1.5 to establish the scale of $\dot{M}$ in terms of the Eddington rate $\dot{M}_{\mathrm{Edd}}$. To get the steady state of the star's rotation period, we compute the orbital period of the infalling matter at the Alfvén radius; no angular momentum transfer occurs when the matter at the Alfvén radius is co-rotating with the star. The period P and radius R of a circular orbit about a mass M are related by

$$P^2 = \frac{4\pi^2}{GM} R^3. \tag{1.10}$$

Putting $R = R_A$, we obtain the equilibrium spin period of the star (this is Equation 5.3 of Bhattacharya (1995) except a typo is corrected):

$$P_{\mathrm{eq}} = (1.9\,\mathrm{ms}) \left(\frac{\dot{M}}{\dot{M}_{\mathrm{Edd}}}\right)^{-3/7} \left(\frac{M}{1.4\,M_\odot}\right)^{-5/7} \left(\frac{B_\star}{10^9\,\mathrm{G}}\right)^{6/7} \left(\frac{R_\star}{10^6\,\mathrm{cm}}\right)^{15/7}. \tag{1.11}$$

This treatment is a considerable idealisation, but it shows the basic dependence on the equilibrium period with the four basic quantities describing the situation. It shows, for example, that in order to spin up to millisecond periods, the magnetic field strength at the surface of the neutron star must be relatively weak: closer to 10^9 G than 10^{12} G. This agrees with the magnetic field strengths inferred from the spin-down of recycled radio pulsars. It is also consistent with the bursting behaviour in many LMXBs, as higher magnetic field strengths have been shown to suppress the thermonuclear instability (Joss and Li, 1980). Furthermore, it is a reason why millisecond-period X-ray pulsations are difficult to detect, as weaker magnetic fields lead to larger polar caps as well as weaker binding of the infalling matter to the magnetic field lines. While it is apparent from Equation 1.11 that relatively weak magnetic fields are necessary for accretion-powered recycling to millisecond periods, it is not well-established how these neutron stars come to have magnetic fields so weak compared to the larger population of conventional pulsars. Models of the origin and evolution of neutron star magnetic fields are reviewed by Bhattacharya and Srinivasan (1995) and Bhattacharya (2002). Some modern models of magnetic field evolution in neutron stars suggest that long-term accretion leads to the decay of the magnetic field strength of the neutron star, a possibility

first suggested by Bisnovatyi-Kogan and Komberg (1974). Urpin *et al.* (1998) have developed a model of neutron star evolution including accretion effects on the magnetic field (and period) evolution of an accreting neutron star in an LMXB. In their calculations it is not just the amount of accreted mass that determines the final magnetic field, but the accretion *rate* and the length of the accretion phase (also see Urpin and Geppert (1995)). The lower the accretion rate, the weaker the magnetic field for a given ΔM.

Completing the order-of-magnitude estimates, we can also make an estimate of the amount of matter that needs to be accreted to spin up to the steady state. The specific angular momentum of the matter at the Alfvén radius is $2\pi R_A^2/P$. Using Equation 1.10, the rate of angular momentum accretion is therefore

$$\dot{J} = \dot{M}\sqrt{GMR_A}. \tag{1.12}$$

The moment of inertia of the star is $I_\star \sim M_\star R_\star^2$, and $J_\star \sim I_\star \Omega_\star$. The time scale for spin-up to $P_{\rm eq}$ is:

$$\tau_{\rm spin-up} = \frac{J_\star}{\dot{J}} = \frac{2\pi R_\star^2 \sqrt{M}}{P_{\rm eq}\dot{M}\sqrt{GR_A}} \approx 1.4 \times 10^7\,{\rm a}, \tag{1.13}$$

where we have assumed $P_{\rm eq} = 1.9\,{\rm ms}$, $R_A = 2.6{\times}10^6\,{\rm cm}$, $\dot{M} = \dot{M}_{\rm Edd} = 1.5 \times 10^{-8}\,M_\odot/{\rm a}$, $R_\star = 10^6\,{\rm cm}$, and $M = 1.4\,M_\odot$. Over this length of time, the neutron star will accrete about $0.1\,M_\odot$. Such long-term accretion can only take place in LMXBs. In an HMXB, the separation of the system is either such that the neutron star only accretes via a wind (a less efficient means of transferring angular momentum and mass), or else the donor star *is* overflowing its Roche lobe, which for HMXBs is unstable and does not persist for longer than about 10^3–10^4 a, at the end of which tides bring the system into close enough contact that a common envelope forms (Bhattacharya, 1995; Tauris and van den Heuvel, 2006).

It is theoretically possible for the spin periods of neutron stars to be in the sub-millisecond range since the breakup speed of neutron stars can exceed 1000 Hz (see Table 4.1 for the breakup speeds of $1.4\,M_\odot$ neutron star models computed using two different equations of state, also Cook *et al.* (1994a) and Cook *et al.* (1994c)). However, no observation of any object which has been recycled by accretion flow (X-ray and radio millisecond pulsars, and type I bursters) has yet ruled out even the largest realistic models of neutron stars, corresponding to the lowest breakup speeds and stiffest equation of state candidates. This might be explained by typi-

cal LMXB properties being such that the steady-state spin period of Equation 1.11 never reaches the bound imposed by the breakup speed of neutron stars. On the other hand, an exciting possibility is that gravitational radiation provides an angular momentum sink beyond about 700 Hz (Bildsten, 1998). Two possibilities that would provide the necessary time-dependent mass quadrupole for gravitational radiation are anisotropies in the temperatures in the surface layers of the neutron star, resulting in anisotropies in the matter (Bildsten, 1998), or the excitation of non-radial stellar oscillations (Andersson, 1998; Friedman and Morsink, 1998; Andersson *et al.*, 1999). Heyl (2002) suggested that the gravitational radiation from such oscillations may be detectable with LIGO.

1.3.3 Evolution of X-ray binaries

The total number of X-ray binaries in the Galaxy is thought to be on the order of several hundred (Psaltis, 2006), and there are about 160 known recycled millisecond radio pulsars (Lorimer, 2005). The relatively small total number of these objects implies that they are the byproduct of rare evolutionary scenarios, and their concentration in old stellar populations towards the galactic centre and in globular clusters implies that the processes leading to their formation take very long to conclude. Models of X-ray binary formation and evolution are reviewed by Verbunt (1993), Verbunt and van den Heuvel (1995) and Tauris and van den Heuvel (2006); only a very brief overview of the main formative processes thought to be involved in the evolution of LMXBs is given here.

First, it is relatively straightforward to see why one needs to appeal to exotic formation processes, especially in the case of LMXBs. The standard picture of binary evolution involves two stars in a binary of masses M_1 and M_2, separated in a circular orbit of diameter a. Suppose that $M_1 > M_2$, so that M_1 evolves faster and and is massive enough to leave behind a neutron star or black hole of mass M_r after the supernova at the end of its life. For the system to be initially gravitationally bound, the energy $E_i = \mathrm{KE} + \mathrm{PE} < 0$. The initial energy in terms of the masses is

$$E_i = \frac{1}{2}M_1 v_1^2 + \frac{1}{2}M_2 v_2^2 - \frac{GM_1M_2}{a}. \tag{1.14}$$

Since the stars orbit about their mutual centre of mass, we know that $M_1|v_1| = M_2|v_2|$. Then

$$E_i = \frac{1}{2}M_2 v_2^2 \left(1 + \frac{M_2}{M_1}\right) - \frac{GM_1M_2}{a}. \tag{1.15}$$

The virial theorem of Clausius (see Clausius (1870); Goldstein (1950) includes a

proof as does a short online article by Baez (2000) and other mechanics texts; other applications to astrophysics are discussed in Saslaw (1985), and Binney and Tremaine (1987)) says that this gravitationally bound system satisfies

$$E_i = \frac{1}{2}\mathrm{PE}; \tag{1.16}$$

therefore,

$$M_2 v_2^2 = \frac{GM_1M_2}{a}\frac{1}{1+M_2/M_1}. \tag{1.17}$$

For the purpose of this argument, we make the unrealistic assumption that the core collapse and resulting explosion is spherically symmetric, and that M_2 is neither significantly ablated nor propelled by the explosion. Then the final energy E_f is

$$\begin{aligned} E_f &= \frac{1}{2}M_r v_r^2 + \frac{1}{2}M_2 v_2^2 - \frac{GM_rM_2}{a} \\ &= \frac{GM_2}{2a(M_1+M_2)}\left[M_1^2 - M_r(2M_1+M_2)\right], \end{aligned} \tag{1.18}$$

where we have made use of Equation 1.17. For the system to remain bound after the supernova, $E_f < 0$. Then Equation 1.18 implies that for the binary to survive the explosion

$$M_r > M_1\frac{1}{2+M_2/M_1}. \tag{1.19}$$

Consider that the formation of a neutron star by an isolated star is the endpoint of main sequence stars with initial masses $8\,M_\odot < M_1 < 25\,M_\odot$, which during their evolution obtain He cores with masses between 2.1–8 $M_\odot$ (Tauris and van den Heuvel, 2006). In an LMXB, $M_2 \lesssim 1\,M_\odot$. In the cases we are interested in, the mass of the remnant must be more than about $M_1/2$ in order for the binary to remain bound. But surely, this condition is never satisfied since the canonical neutron star mass is $M_r \sim 1.4\,M_\odot$, much less than half the initial mass M_1. Therefore, as pointed out by Tauris and van den Heuvel (2006), a necessary ingredient to explain the existence of LMXBs must be one or more of the factors we have neglected: the possibility of large scale mass transfer prior to the supernova (discussed below), ablation of the companion by the supernova, or the possibility of asymmetric core collapse which imparts a "kick" to the resulting neutron star. The importance of supernova kicks for the formation of short-period LMXBs is discussed by Kalogera and Webbink (1998), and their dynamical consequences have been analysed by Hills (1983), and Tauris and Takens (1998) (Tauris and van den Heuvel, 2006). Modern models of binary evolution must include some consideration of all of these effects

in order to allow for a non-zero birthrate of LMXBs.

LMXBs might be formed by several different processes. The standard picture is as the product of common envelope (CE) evolution of an extreme mass ratio main sequence binary, but several other scenarios might also form LMXBs which are mentioned at the end of the section. The CE evolution scenario was first proposed by Paczyński (1976) and Ostriker (1976), and is discussed in detail in the aforementioned reviews and their accompanying references. A typical picture of CE evolution (Tauris and van den Heuvel, 2006) of a binary with an LMXB as the endpoint involves two main sequence stars, one with mass $M_1 \gtrsim 10\,M_\odot$, the other with mass $M_2 \sim 1\,M_\odot$. The more massive star evolves faster, and if the binary is close enough M_1 will fill its Roche lobe when it enters the red giant phase of its evolution and begin transferring mass to M_2. The transfer of mass drives the inspiral of the binary. This is easy to see in the framework of a conservative system (Verbunt and van den Heuvel, 1995): if the total mass $M_1 + M_2$ is always conserved, then

$$M_{1f} = M_{1i} - (\Delta M) \tag{1.20}$$

$$M_{2f} = M_{2i} + (\Delta M). \tag{1.21}$$

The total angular momentum J of the system is also conserved, with value

$$J = M_1 M_2 \left(\frac{Ga}{M_1 + M_2}\right)^{1/2}. \tag{1.22}$$

This leads to the following expressions for the change in the separation a and period P of the binary in terms of the initial masses and the size of the mass transfer ΔM (Kepler's third law is invoked for the result involving P):

$$\frac{a_i}{a_f} = \left(1 + (\Delta M)\frac{M_{1i} - M_{2i}}{M_{1i}M_{2i}} + \frac{(\Delta M)^2}{M_{1i}M_{2i}}\right)^2 \tag{1.23}$$

$$\frac{P_i}{P_f} = \left(1 + (\Delta M)\frac{M_{1i} - M_{2i}}{M_{1i}M_{2i}} + \frac{(\Delta M)^2}{M_{1i}M_{2i}}\right)^3. \tag{1.24}$$

So it is clear that mass transfer in a binary leads to inspiral of the stars. In the case we are considering, the inspiral will eventually bring the lower mass star inside the Roche lobe of the giant, and the CE evolution phase begins. In CE evolution (Tauris and van den Heuvel, 2006), the inspiral accelerates due to the drag on the lower mass star. At the same time, the deposition of the orbital energy within the

envelope leads to relatively rapid dissipation of the envelope of the giant's He core. At the end of this phase of evolution, a naked He star is in a small orbit with a main sequence star. Eventually the He star evolves resulting in a supernova and formation of a neutron star. At this stage of evolution, the binary will have evolved for on the order of several times 10^7 a, set by the nuclear timescale of the initially more massive star, $\tau_{\rm nuc} \simeq 10\,{\rm Ga}(M/M_\odot)^{-2.5}$.

If the binary remains bound after the supernova, then under certain conditions a subsequent phase of inspiral lasting on the order of several times 10^9 a (Tauris and van den Heuvel, 2006) may take place which brings the binary back into contact for another period of mass transfer, resulting in the formation of an LMXB. Detailed models of CE evolution solve the problem of bringing the progenitors of the LMXB into a close enough orbit that the second phase of mass transfer begins within the Hubble time.[1] The evolution of the bound post-supernova binary is determined largely by detailed models of the mechanisms which can dissipate orbital angular momentum. These mechanisms can include magnetic braking of the binary, the possible exchange of angular momentum between the star spin and the orbit by expansion or contraction of the non-degenerate star, mass loss, and gravitational wave radiation (Tauris and van den Heuvel, 2006). Gravitational wave radiation is only important in close binaries, and would not necessarily be the dominant mechanism initially driving the inspiral after the supernova of the more massive star. During this second inspiral phase, the stars may again be brought into contact and the remaining main sequence star begins mass transfer through its Roche lobe to the neutron star (in the opposite direction of the initial mass transfer!), and the system manifests itself as an LMXB. When the system is in contact, the mass transfer is driven by the continued loss of angular momentum via magnetic braking (discussed in §16.4.1 of Tauris and van den Heuvel (2006)), or gravitational wave radiation, the importance of which was recognised by Faulkner (1971) who considered the similar scenario of white dwarf stars accreting matter by Roche lobe overflow of a red main sequence companion.

Other processes leading to the formation of LMXBs have been suggested as well (Verbunt and van den Heuvel, 1995). In one scenario, suggested by Whelan and Iben (1973), Canal and Schatzman (1976), and Canal *et al.* (1990), one begins again with a high-mass binary of extreme mass ratio but this time the massive star evolves to a relatively massive white dwarf instead of a neutron star. The inspiral phase

[1] A rough estimate of the age of the universe is given by the inverse of the Hubble constant, $H_0 = 100h\,{\rm Mpc}^{-1}\,{\rm km\,s}^{-1}$. The three year WMAP results have $h = 0.73 \pm 0.03$ (Spergel *et al.*, 2006); the corresponding rough estimate of the universe's age is 1.3×10^{10} a.

after the formation of the white dwarf leads to mass transfer from the remaining main sequence star, which pushes the white dwarf over the Chandrasekhar limit, resulting in the formation of a neutron star binary. This process is called "accretion-induced collapse." One advantage of this scenario is that the resulting supernova may be less disruptive to the system than the direct formation of a neutron star by the evolution of a massive He core.

In globular clusters, capture scenarios may contribute to the formation of LMXBs (Verbunt and van den Heuvel (1995) point out Clark (1975), Fabian *et al.* (1975), Sutantyo (1975), and Verbunt (1988); Verbunt and Lewin (2006) review the globular cluster X-ray sources). X-ray binaries are over-represented in globular clusters compared to the Galaxy: consider that some 10% of known X-ray binaries are in globular clusters which contain on the order of 10^{-4} as many stars as the Galaxy (Verbunt and van den Heuvel, 1995), so it seems reasonable to suggest additional evolutionary scenarios that enhance the birth of LMXBs in globular clusters. The reviews by Verbunt and van den Heuvel (1995) and Verbunt and Lewin (2006) discuss these scenarios in detail: First, it has been suggested that single neutron stars can pass a binary in globular clusters, forming a triple. Triples are unstable, and typically the lowest mass member is ejected, which may leave behind a neutron star binary. The other scenario that has been suggested is the tidal capture of a main sequence or giant star by a neutron star, or possibly direct collisions between giant stars and neutron stars. These scenarios may be problematic owing to the possible destruction of the companion by tides (McMillan *et al.*, 1987; Ray *et al.*, 1987).

1.3.4 X-ray pulsation mechanisms

The remaining chapters are primarily concerned with the interpretation of millisecond-period pulsed X-ray light from a region on (or close to) the surface of neutron stars. In the context of LMXBs containing a rapidly-rotating neutron star, the broad category of "X-ray variability" encompasses the seven millisecond-period X-ray pulsars, the aforementioned type I X-ray burst oscillations, and there is also a category of oscillations known as (kilohertz) quasi-periodic oscillations (QPOs). The work in this thesis was primarily motivated by the prospect of analysing the pulse profiles of the millisecond X-ray pulsars. This is a very young field of endeavour, as the only published phase-resolved spectra of such systems with persistent pulsations are for the first millisecond X-ray pulsar, SAX J1808.4-3658 (see Cui *et al.* (1998), Gierliński *et al.* (2002) and Papitto *et al.* (2005)). Like radio pulsars, the pulse profile of X-ray pulsars can be determined by sufficiently long observation, so for

the sort of analysis we envision it is important to consider mainly sources with persistent pulsations and stable frequencies. There is also direct applicability of this work to the analysis of type I X-ray burst light curves, since this phenomenon also arises from the rotational modulation of a bright spot on the surface of a neutron star. In comparison with the persistent millisecond X-ray pulsars, pulse profiles of X-ray burst oscillations are somewhat more readily available, but present other analysis challenges arising in part from their necessarily short observation time. An additional complication is that these sources do not have stable (brightness) oscillation frequencies, although they are approximately so, and the phenomenology of the frequency evolution is mostly well-described (Strohmayer and Markwardt, 1999). The QPO phenomenon is thought to be a completely separate issue and the chapters that follow have no obvious applicability to this category of variability. In this section we give a very brief overview of these separate categories.

X-ray pulsars

After the discovery of the first long-period X-ray pulsar in an HMXB (Giacconi *et al.*, 1971), it was quickly understood that these pulsars came about by accretion of matter directed onto the magnetic poles of a rotating neutron star. In this situation, the heating of the neutron star surface caused by the funnelling of hot plasma to the magnetic poles produced a bright spot which rotates through the line-of-sight of the observer, which is observed as pulsed X-ray light.

A variety of models of accretion geometries near the surface of the neutron star have been developed to provide a theoretical basis for the interpretation of the phase-resolved spectroscopy of X-ray pulsar observations. For example, Nagel (1981) used radiative transfer calculations to investigate the emitted spectrum and anisotropy in two different accretion geometries: a slab perpendicular to the magnetic field, and a cylindrical accretion column with its axis parallel to the magnetic field. The slab geometry is most applicable in low luminosity sources when the accreting matter is decelerated close to the star; in this case radiation was preferentially emitted along the magnetic axis (a "pencil beam"). In the accretion column case, a radiative shock forms far from the star beneath which the accreting matter settles onto the star via a stagnant flow, and radiation escaped from the sides of the resulting column (a "fan beam" emitted preferentially away from the radial direction). More complicated accretion geometries can be envisaged. For example, Kraus *et al.* (2003) investigated the pulse profile produced by a dipole-shaped accretion funnel with a blackbody "halo" around the base of the funnel on

the surface of the neutron star, and others have proposed that the accretion flow forms a "mound" shape under the shock.

In addition to the accretion geometry, the spectrum of the emitted light is also important. A realistic description of the spectrum of accreting X-ray pulsars depends on the energies being considered. A blackbody component of the spectrum describes soft X-rays, which may be X-rays emitted from the surface of the neutron star which is heated by the accretion flow (see, e.g., Zavlin *et al.* (1995) for a detailed treatment of this point, and Kraus *et al.* (2003)). The spectrum of hard X-rays is described by a power law with an exponential cutoff at high energies; this radiation is understood as originating in the accreted matter and "Comptonized" by hot electrons before leaving the accreting system. This is understood by considering radiation passing through an optically thick cloud of hot, completely ionized plasma, where the photons and plasma interact only by Compton scattering. Multiple scatterings of X-ray photons on thermal electrons result in the distortion, or Comptonization, of the input spectrum, since in each scattering the frequency of the photon changes due to the Doppler and recoil effects (Sunyaev and Titarchuk (1980); also see Rybicki and Lightman (1979)).

Additionally, there may be discrete spectral features in the phase-averaged spectrum such as cyclotron resonance scattering features, or spectral lines. Ibrahim *et al.* (2002) discuss observational evidence of a cyclotron resonance feature in SGR 1806-20, and Heindl *et al.* (2004) review this phenomenon in the context of classical X-ray pulsars. Considering the spectral lines, Cottam *et al.* (2002) observed a gravitationally-redshifted absorption line from a neutron star, and Chang *et al.* (2006) is a recent theoretical treatment of the effects of rotation on such spectral lines. These discrete spectral features in neutron star spectra may permit a direct measurement of the total redshift (and therefore the compactness), and in the case of the cyclotron lines, the magnetic field.

With a model of the emission region and a model of the emitted spectrum, general relativity can be used to calculate the path taken by photons from the emission region to the observer, and an observed pulse profile calculated, which generally depends on the observed energy band. The simplest case of such a calculation which included relativistic light deflection was carried out by Pechenick *et al.* (1983) for emission from polar caps, with application to the slow X-ray pulsars. Using this basic method to compute model light curves, perhaps with different accretion geometries and model spectra, fits to observations of the slow X-ray pulsars have yielded constraints on the compactness of the neutron star and the nature of the

emitted radiation; this is discussed in more detail in the introduction to Chapter 4. The first, and so far only, application of this kind of analysis for persistent millisecond X-ray pulsars was carried through by Poutanen and Gierliński (2003), which yielded a loose constraint on the mass and radius of the neutron star and the inclination of the system. This particular analysis used phase-resolved spectroscopy of the pulsar in the soft and hard bands together with a two component spectral model of the beamed emission. However, it is straightforward to see how the mass and radius of the neutron star can be encoded in a simplified version of the situation, where the pulsed light arises from isotropic emission, and one observes only the bolometric light curve. In this situation, the (relativistic) velocity of the emission region (which scales with R) determines the asymmetry of the light curve due to Doppler boosting, while the compactness M/R determines the degree to which light can "bend" around the star. By fitting model light curves with observations, a set of parameters consistent with the data can be obtained. In a standard application of the framework provided by Pechenick *et al.* (1983), the star's surface and the exterior spacetime is assumed to be spherically-symmetric, and the variation of the time-of-flight of photons with phase is neglected. The overarching goal of this dissertation is to show that such *computational approximations which are useful for slower pulsars, such as using an approximate spacetime, neglecting some time delay effects, or neglecting stellar oblateness, can lead to significant failures in interpreting the pulse profiles of millisecond pulsars.*

Type I X-ray bursts: "nuclear-powered" pulsars

The discovery of coherent X-ray pulsations in the cooling tails of type I X-ray bursts provided the first evidence that neutron stars in LMXBs could be spun up by accretion to millisecond periods. The bursting behaviour of LMXBs was not a new phenomenon, having first been observed in 1976 (Grindlay *et al.*, 1976; Belian *et al.*, 1976), and the physics which gives rise to the bursts is relatively well understood. A recent review of type I X-ray bursts is given by Strohmayer and Bildsten (2006); also see Lewin *et al.* (1995).

These flashes are a manifestation of the "thin shell" instability of Schwarzschild and Härm (1965), which was originally discovered as an instability in the thin helium shell residing above the carbon/oxygen core during the asymptotic giant branch of stellar evolution (Strohmayer and Bildsten, 2006). In this situation, the rate of thermonuclear burning is more temperature sensitive than the rate of radiative cooling. Hansen and van Horn (1975) showed that the same instability

can apply to the accreted hydrogen and helium on the surface of a neutron star. X-ray bursts arising from the unstable burning of accreted matter are known as "type I" bursts. The physics of the burning of the accreted material depends not only on the composition of the matter being accreted, but also on the accretion rate. For low accretion rates, unstable hydrogen burning ignites a hydrogen/helium mixture. At higher rates, the accreted hydrogen burns stably via the CNO cycle (although at the highest accretion rates, it may not burn completely off) and the burst is fuelled by the unstable ignition of helium. Strohmayer and Bildsten (2006) point out some relevant papers discussing the accretion-rate dependence of nuclear burning by Fujimoto *et al.* (1981), Fushiki and Lamb (1987), and Cumming and Bildsten (2000). Bursts are not observed from classical high magnetic field X-ray pulsars, because the accreted matter is strongly channelled to the magnetic poles resulting in a high local accretion rate which leads to stable burning (Joss and Li, 1980).

There is also a recently-discovered class of related bursts called "superbursts" (the first such burst was discovered by Cornelisse *et al.* (2000) (Strohmayer and Bildsten, 2006)) which are much rarer, with recurrence interval of years, versus days or months for type I bursts. These bursts are thought possibly to be the result of unstable burning of carbon deeper down in the surface layers of the neutron star. "Type II" bursts are an unrelated, and poorly understood, phenomenon thought to be related to an accretion instability which leads to a rapidly varying rate of mass deposition on the neutron star. In 2003 there were only two known examples of type II bursters. We will always mean the nuclear-powered bursts when we refer to X-ray bursts.

In 2003 there were about 160 known LMXBs, 70 of which were bursting sources, and approximately eleven of these had been observed to exhibit coherent burst oscillations with frequencies ranging between 270–620 Hz (Strohmayer and Bildsten, 2006). Muno (2002) undertook a systematic analysis of all type I X-ray bursts from eight LMXBs in public RXTE data as of September 2001, and identified 68 oscillation trains detected in a search of 159 separate bursts. The main results of this work were published as Muno *et al.* (2000), Muno *et al.* (2002a), and Muno *et al.* (2002b). A common feature of burst oscillations is an observed increase in frequency by several Hz during the burst, but the mechanism producing this effect is not well-established. The phenomenology of the frequency evolution is often well-described as an exponential "chirp," with the asymptotic frequency in the cooling tail being a stable characteristic of the bursting source and is taken to be the rotation frequency

of the neutron star. Strohmayer *et al.* (1997) suggested that this phenomenon might be understood as the combined effect of angular momentum conservation and expansion of the burning matter. In this model, a "shell" of accreted matter expands (e.g., hydrostatically) as energy is released by the burning. The expanded shell of the burning matter initially rotates with a longer rotational period than that of the underlying star, owing to the larger radius of rotation and conservation of angular momentum. The subsequent cooling and contraction of the shell, still governed by the conservation of angular momentum, produces the observed increase in the frequency of the oscillations in the tail of the burst. A theoretical analysis of this process was carried out by Cumming *et al.* (2002), where it was shown that this basic model cannot account for the size of the observed frequency shifts. Other work (e.g., Spitkovsky *et al.* (2002)) on understanding the frequency evolution of X-ray burst oscillations has concentrated on modelling the evolution of the burning front on the surface of the rotating neutron star, by considering the Coriolis force and nuclear physics effects on the propagation of the "thermonuclear flame." Heyl (2004) has considered the possibility that the burst oscillations arise from modes of the neutron star atmosphere excited by the thermonuclear detonation.

As applications, X-ray bursts may have the potential to constrain the radius of neutron stars loosely. The basic technique is to fit the observed spectrum with a blackbody and assume isotropic emission to obtain the surface area of the star. The main problem with this is that the radiation is not isotropic and perhaps only a fraction of the surface is emitting (van Paradijs, 1979). X-ray bursts that exhibit radius expansion, also revealed through spectral fits taken over different times, may also give an approximate standard candle for distance measurements, as radius expansion is expected to occur when the luminosity of the burst exceeds the Eddington limit (van Paradijs, 1978). The theoretical Eddington luminosity is known given at least the mass of the accreting neutron star by Equation 1.4, which applies to the non-relativistic limit $1/\tilde{r} \ll 1$ and spherical accretion of hydrogen plasma. In practice, more complex treatments are used which account for relativistic effects, the composition of the accreted material, and anisotropy of the accretion (e.g., van Paradijs and Lewin (1987)). Therefore, if reasonable values of the parameters which determine the Eddington luminosity are known, the observed flux can be used to obtain the implied distance to the source. van Paradijs (1979) recognised that this simple interpretation could also be problematic in practice. For example, a recent examination by Kuulkers *et al.* (2003) of X-ray burst oscillations showed that these bursts are not perfect standard candles since the peak

luminosities of Eddington-limited X-ray bursts are not exactly constant, but can vary by about 15%.

The basic physical process envisioned in this dissertation concerns the rotational modulation of X-ray light emitted from a region on the surface of a neutron star, which is how X-ray burst oscillations come about. While phase-resolved spectroscopy of X-ray burst oscillations is made more difficult by their intermittent nature, there has been some work on using formalisms similar to Pechenick *et al.* (1983) to compute model pulse profiles for X-ray burst oscillations which have been used to constrain neutron star parameters (see Weinberg *et al.* (2001), Nath *et al.* (2002), Muno (2002), and Bhattacharyya *et al.* (2005)). As a result, the work carried out in this dissertation is also relevant to similar analyses of burst oscillation pulse profiles.

Kilohertz Quasi-periodic oscillations (QPOs)

Another phenomenon associated with millisecond variability of X-ray light from LMXBs are kilohertz QPOs; this and other phenomena associated with X-ray variability are reviewed by van der Klis (1995) and van der Klis (2006). QPOs are generally defined as broad peaks revealed in the Fourier power spectra of X-ray timing observations. For the kHz QPOs in LMXBs, the Fourier spectra often indicate significant power at frequencies typically between 200–1200 Hz, but the broadness of the peaks in the power spectrum indicate that the oscillations are not coherent as in the case of the X-ray burst oscillations and X-ray pulsars. A lot of attention has been paid to the fact that often there are two peaks in the power spectrum in LMXBs, an upper QPO centred on $\nu_{\rm hi}$ and a lower QPO at $\nu_{\rm lo}$. Méndez *et al.* (2001) and the references they cite give a concise description of kilohertz QPO phenomenology: in a given binary, during observations over timescales of a day or less, a QPO frequency versus intensity diagram tends to display a set of almost parallel tracks, i.e., tracks separated by nearly constant $\Delta\nu = \nu_{\rm hi} - \nu_{\rm lo}$. On this timescale, QPO frequency and X-ray count are positively correlated, with the peak locations changing by typically a few hundred Hertz, but their separation $\Delta\nu$ changing by only tens of Hertz. However, in observations separated by a few days the source occupies different tracks in such a diagram, and QPO frequency and X-ray count rate are now known to be uncorrelated over the long term (Méndez *et al.*, 2001). The early realisation that $\Delta\nu$ appeared to be nearly constant led to suggestions that the upper QPO is associated with the orbital motion at the inner edge of the accretion disk, with the lower QPO a beat between the upper

QPO and the neutron star rotation frequency (Miller *et al.* (1998), but see Morsink (2000) for a popular description of the QPO beat frequency model). While the phenomenology of these QPOs is interesting (for example, it has been suggested that they may contain an observational signature of the innermost stable circular orbit (ISCO) predicted by general relativity by Barret *et al.* (2006)), it seems likely that a complete understanding will involve detailed modelling of the star-disk interaction. Recent progress has been made on modelling the magnetohydrodynamics of the accretion flow with application to kilohertz QPOs by Romanova *et al.* (2006). We mention the kilohertz QPOs only to distinguish them from the phenomena that this work directly applies to.

1.4 Organisation of the dissertation

This work is carried out in two phases. The first phase is constructive, where a means by which to compute a pulse profile is established within the framework of a precisely solved spacetime metric and stellar structure, with all photon time-of-flight effects included. We also need to be able to carry out approximate versions of this calculation which have direct analogies in the literature in order to make statements about the degree by which the full calculation differs from its approximations. The analytical framework for this is set out in Chapter 2 which begins with a discussion of the general stationary axisymmetric spacetime metric and its special cases, through to the integration of null geodesics in using this metric, and a careful discussion of the effects introduced by rapid motion of the emission region. The chapter concludes with an analytical comparison of the proposed "full" calculation, with an extant adaptation of the method described by Pechenick *et al.* (1983) designed for millisecond period X-ray pulsars. The constructive phase concludes in Chapter 3, where the computer code that was developed for this work is described and verified.

The next phase of the work, Chapter 4, is inductive. We make substantial use of the developed computer code in a variety of cases to determine the level at which commonly-used simplifying approximations change the calculated pulse profiles, and the impact this will have on conclusions arrived at by fitting model pulse profiles to X-ray observations. In the first part of this work, we consider a simple model where light is emitted and observed in the equatorial plane, and the phase-dependent time-of-flight of photons from the emission region to the observer is discarded in the approximate calculation. In the next part of the work, we allow

the inclinations of the observer and emission regions to be general, and we consider the effects of approximating the spacetime and discarding the rotation-induced deformation of the star's surface. The result of this work provides compelling evidence that the techniques which have been developed for slower pulsars (which use approximate spacetimes, neglect some time delay effects, and neglect stellar oblateness) cannot be directly applied to the interpretation of the pulse profiles of accretion-powered millisecond X-ray pulsars.

Finally, we set the stage for future work at the end of Chapter 4 by giving a simple model of rotation-induced oblateness which does not require the user to perform a full stellar structure calculation, and we make a demonstration that this oblateness model can be used to substantially improve extant codes which are optimised for fitting quickly-computed pulse profiles to data.

1.4.1 Notes on the text

The major conclusions of this research have been published or accepted for publication as Cadeau *et al.* (2005) and Cadeau *et al.* (2006). Some figures and text from these papers are reproduced here; material appearing in Cadeau *et al.* (2005) is "©2005. The American Astronomical Society. All rights reserved.", and material appearing in Cadeau *et al.* (2006) is "©2007. The American Astronomical Society. All rights reserved." The Society grants a standard non-exclusive license to authors to republish their material if appropriate credit is given to the Journal and the copyright notice is reproduced.

The oblateness model and suggested adaptation of simpler pulse profile codes which is given at the end of Chapter 4 only appears here and is the subject of ongoing work. The constructive part of this work was carried out independently. For the inductive part, I calculated the "non-approximate" versions of the pulse profiles using the code I developed, while D. A. Leahy calculated the fitted sets of parameters using a computer code which employed an "approximate" calculation for the forward calculation of the pulse profile. I was also fortunate to be able to both contribute to, and benefit from, collaboration with D. A. Leahy in the verification phases of our respective codes.

Chapter 2

Calculating the light curve

2.1 Introduction

In this chapter we devise a means to calculate the light curve, or pulse profile, of a rapidly-rotating neutron star which emits light from a small patch on its surface. To begin with, consider a two-dimensional area of a non-rotating star which emits light with frequency ν_e, with specific intensity I_{ν_e}. An observer far from the star sees that the area of the emitting region subtends a solid angle $\mathrm{d}\Omega_o$ on the sky, and the received photons have an observed frequency ν_o. Without relativistic effects, the received light will have the same frequency as the emitted light, and the received specific intensity is independent of the distance to the source (Shu, 1991). When relativistic effects such as Doppler boosting or gravity act to change the frequency of the observed light, one defines the redshift z through the relation $1+z = \nu_e/\nu_o$. In this case, making use of conservation of photon number density in phase space, the intensity reaching the observer can be shown to transform as $I_{\nu_o} = I_{\nu_e}/(1+z)^3$ (Misner *et al.*, 1973; Shapiro and Teukolsky, 1983). The element of observed specific flux is

$$\mathrm{d}F_{\nu_o} = I_{\nu_o}\mathrm{d}\Omega_o = I_{\nu_e}\left(\frac{1}{1+z}\right)^3 \mathrm{d}\Omega_o. \tag{2.1}$$

The total flux registered by a detector is given by the frequency integral over the detector's sensitivity band. If the detector is sensitive to all frequencies, then the integrated flux is called the *bolometric flux*. The integral is

$$\mathrm{d}F = \int_{\nu_{o_{\mathrm{lo}}}}^{\nu_{o_{\mathrm{hi}}}} \mathrm{d}\nu_o I_{\nu_e}\left(\frac{1}{1+z}\right)^3 \mathrm{d}\Omega_o$$

$$= \int_{(1+z)\nu_{o_{\rm lo}}}^{(1+z)\nu_{o_{\rm hi}}} \mathrm{d}\nu_e I_{\nu_e} \left(\frac{1}{1+z}\right)^4 \mathrm{d}\Omega_o. \tag{2.2}$$

In general, the radiation may be beamed, and the intensity I_{ν_e} will depend on the initial direction rays take to reach the observer. If α_e is the angle the observed rays form with the normal to the surface of the star, then the shape of the beam is given by specifying $I_{\nu_e}(\alpha_e)$. In this work we will show how our calculation can be easily extended for beamed emission, but our main results will be presented in the context of isotropic emission and bolometric flux. We wish to study fundamental issues concerning pulse profile calculations and their applications for the millisecond-period X-ray pulsars. Considering the uncertainty in the correct models for the energy and direction dependence of I, our calculations have been limited to bolometric, isotropic flux for the results presented in this dissertation.

At this stage we have not yet introduced the rotation of the star, but a few things are already intuitively obvious: in order to calculate the received flux by an observer far from the star, we will need to know about the particular light rays which reach the observer. For example, as the emission region rotates around the star, we know that:

1. The redshift z may depend on phase if the speeds at the star's surface are relativistic, since in this case the photon energies will be Doppler boosted.

2. As the emission region moves around the star, its orientation along the observer's line-of-sight, and therefore its projection on the observer's sky, will be changing. Thus $\mathrm{d}\Omega_o$ is phase-dependent.

3. The times-of-flight for photons to reach the observer will generally be phase dependent, and in the case of the fastest millisecond-period X-ray pulsars, this variation becomes an appreciable fraction of the rotation period. Thus the time-of-arrival of flux at the observer is phase-dependent.

In order to quantify these effects, we need to be able to calculate a description of the light rays connecting the emission region on the star and the observer. This is the basic idea behind the pulse shape codes developed for slowly-rotating neutron stars by Pechenick *et al.* (1983), where the main effect being investigated is the effect of gravitational "bending" of light around neutron stars on the observed pulse profile. In contrast to this treatment, for rapidly-rotating neutron stars the spacetime is no longer spherically symmetric, nor analytically specified, which complicates the problem.

In relativity, light rays follow (null) geodesic paths. Solving for the null geodesics of precisely-solved neutron star spacetimes, discussed below, is not a new problem. Nollert *et al.* (1989) presented computer graphic images of neutron stars which included the effect of light bending in accurate spacetimes. Bhattacharyya *et al.* (2001) used a code which implemented ray-tracing in accurate neutron star spacetimes to calculate the spectra of accretion disks. Campbell (2003) developed a code to calculate null geodesics and studied the effect of neutron star mass, radius, and spin frequency on the thermal emission from neutron stars. In the context of pulsed emission from neutron stars, Bhattacharyya *et al.* (2005) acknowledge that it is desireable to carry out pulse profile computations in the framework of a precisely solved spacetime.

In this chapter, we begin by setting out the description of the spacetime metric Section 2.2. In Section 2.3 we write out the equations describing the general null geodesics, and give the equations for the redshift of photons and the emission direction. The use of the calculated null geodesics to obtain the pulse profile is discussed in Section 2.4. To assist with code verification, in Section 2.5 we obtain independent formulas for the pulse profile in the case of a spherical star and the Schwarzschild spacetime, and discuss an extant method which employs a similar method in the context of accurate spacetimes.

2.2 Stationary axisymmetric spacetimes in general relativity

The metric for the general stationary axisymmetric spacetime is described by the line element

$$\mathrm{d}s^2 = -e^{\gamma+\rho}\mathrm{d}t^2 + e^{\gamma-\rho}\bar{r}^2\sin^2\theta(\mathrm{d}\phi - \omega\mathrm{d}t)^2 + e^{2\alpha}(\mathrm{d}\bar{r}^2 + \bar{r}^2\mathrm{d}\theta^2). \qquad (2.3)$$

In stationary axisymmetry, there are two symmetries of the spacetime given by the Killing vectors t^a and ϕ^a. The potentials α, γ, ρ, and ω will generally depend on $\bar{r}$ and θ. It should be noted that this metric is specified in quasi-isotropic coordinates, and circles centred on the axis of symmetry have proper length $2\pi e^{(\gamma-\rho)/2}\bar{r}\sin\theta$, and so $\bar{r}$ should not be interpreted like the usual Schwarzschild areal r coordinate. In Section 2.2.1 we will give the expressions for the metric potentials for the Kerr and Schwarzschild spacetimes.

A precise computation of the metric potentials for a rapidly rotating neutron star must be carried out numerically. Stergioulas (2003) describes the various numerical techniques that have been used. In this work, we have made use of

a public-domain computer code called RNS to accomplish this (Stergioulas and Friedman, 1995). The code assumes that the star is a rigidly-rotating perfect fluid, with four-velocity $u^a \propto (t^a + \Omega_\star \phi^a)$. The angular velocity of the star as measured at infinity is the constant $\Omega_\star$. The Einstein field equations for the metric potentials are given by Butterworth and Ipser (1976), and are a set of three elliptic PDEs for the potentials γ, ρ, and ω. The potential α is determined by solving a first-order ODE involving the other three potentials. The basic method used to solve these equations in RNS was originally devised by Komatsu *et al.* (1989). The method was subsequently improved upon by Cook *et al.* (1992) who applied their code to calculations of rapidly-rotating stars with polytropic equations of state (also see Cook *et al.* (1994b)). Cook *et al.* (1994a) extended this code to use tabulated realistic equations of state, where the function $p(\varepsilon)$ describing the compressibility of neutron star matter is determined by interpolation of datapoints corresponding to realistic equation of state candidates. RNS is an independent implementation of a method similar to the one used by Cook *et al.* (1994a), with additional improvements.

The basic tactic proposed by Komatsu *et al.* (1989) is to convert the elliptic field equations into integral equations using appropriate Green's functions. The user specifies parameters describing the desired neutron star model, which in the case of standard RNS are the ratio of the polar to equatorial radius of the star $\bar{r}_p/\bar{r}_e$, and the central energy density, which are held fixed. The code computes an initial guess for the metric potentials by solving the Tolman-Oppenheimer-Volkoff equations for hydrostatic equilibrium of a non-rotating star, and successive improvements to the computed metric potentials are obtained by iterating on the integral equations for the new set of potentials. This procedure eventually converges, resulting in the potentials describing the desired model. In addition to the metric potentials, integral equations can similarly be added to RNS to accurately compute the first partial derivatives, and the second mixed partial derivative of the metric potentials (Morsink, 2005a). This assists with accurate interpolation of the metric values between gridpoints, using bicubic spline interpolation (Press *et al.*, 1988). We have made independent modifications to RNS so that it automatically converges on models of a specified mass and angular velocity. Additionally, the location of the surface at all latitudes is computed by locating the zero of enthalpy, which is the boundary condition for the star's surface (Haensel and Potekhin, 2004). All useful quantities are output to computer files which are read by the computer code developed for this work, which is described in Chapter 3.

2.2.1 Special cases: Schwarzschild & Kerr metrics

The coordinates used to express the line element in Equation 2.3 are known as "quasi-isotropic" coordinates. When the Schwarzschild metric is expressed in these coordinates, the metric is

$$\mathrm{d}s^2 = -\frac{(1-M/2\bar{r})^2}{(1+M/2\bar{r})^2}\mathrm{d}t^2 + (1+M/2\bar{r})^4\left(\mathrm{d}\bar{r}^2 + \bar{r}^2\mathrm{d}\theta^2 + \bar{r}^2\sin^2\theta\mathrm{d}\phi^2\right), \qquad (2.4)$$

which has the property that surfaces of constant t are conformally Euclidean. These coordinates are known as "isotropic coordinates." The quasi-isotropic coordinates of the general metric in Equation 2.3 are a generalisation of the usual Schwarzschild isotropic coordinates.

In the limit of zero rotation, the following combinations of metric functions are:

$$\lim_{\Omega_\star\to 0} e^{\frac{1}{2}(\gamma+\rho)} = \left(1-\frac{2M}{r}\right)^{1/2}, \qquad (2.5)$$

$$\lim_{\Omega_\star\to 0} \bar{r}e^{-\rho} = r\left(1-\frac{2M}{r}\right)^{-1/2}, \text{ and} \qquad (2.6)$$

$$\lim_{\Omega_\star\to 0} e^{\alpha-\frac{1}{2}(\gamma+\rho)}\mathrm{d}\bar{r} = \left(1-\frac{2M}{r}\right)^{-1}\mathrm{d}r, \qquad (2.7)$$

where $\Omega_\star$ is the star's angular velocity, as measured by an observer at infinity.[1]

The Kerr metric for a black hole without an electromagnetic field in Boyer-Lindquist coordinates is (Boyer and Lindquist, 1967):

$$\mathrm{d}s^2 = \Sigma\left(\frac{\mathrm{d}r^2}{\Delta} + \mathrm{d}\theta^2\right) + (r^2+a^2)\sin^2\theta\mathrm{d}\phi^2 - \mathrm{d}t^2 + \frac{2Mr}{\Sigma}(a\sin^2\theta\mathrm{d}\phi - \mathrm{d}t)^2, \qquad (2.8)$$

with $\Sigma \equiv r^2 + a^2\cos^2\theta$ and $\Delta \equiv r^2 - 2Mr + a^2$. The parameter a is called the specific angular momentum, and is the ratio of the total angular momentum to mass, $a \equiv J/M$. Our goal in this section is to express this metric in the form of Equation 2.3.

The $a = 0$ case is the Schwarzschild metric, but not in isotropic coordinates, so the first step is to find the appropriate transformation $r = \bar{r}f(\bar{r})$ to express this metric in quasi-isotropic coordinates. Looking at the (r,θ) plane, and putting

[1] Note that the unbarred r appearing on the right-hand side of Equations 2.5–2.7 refer to the areal Schwarzschild r coordinate, where circles centred on the axis of symmetry have proper length $2\pi r\sin\theta = 2\pi e^{(\gamma-\rho)/2}\bar{r}\sin\theta$.

$\mathrm{d}r = (f + \bar{r}f')\mathrm{d}\bar{r}$, we have:

$$\mathrm{d}\sigma^2 = \Sigma\left(\frac{\mathrm{d}r^2}{\Delta} + \mathrm{d}\theta^2\right) \tag{2.9}$$

$$= \frac{(\bar{r}f)^2 + a^2\cos^2\theta}{(\bar{r}f)^2 - 2M\bar{r}f + a^2}(f + \bar{r}f')^2\mathrm{d}\bar{r}^2 + \left[(\bar{r}f)^2 + a^2\cos^2\theta\right]\mathrm{d}\theta^2 \tag{2.10}$$

$$= \frac{(\bar{r}f)^2 + a^2\cos^2\theta}{\bar{r}^2}\left[\frac{\bar{r}^2(f + \bar{r}f')^2}{(\bar{r}f)^2 - 2M\bar{r}f + a^2}\mathrm{d}\bar{r}^2 + \bar{r}^2\mathrm{d}\theta^2\right]. \tag{2.11}$$

This is of the required form $\mathrm{d}\sigma^2 = e^{2\alpha}(\mathrm{d}\bar{r}^2 + \bar{r}^2\mathrm{d}\theta^2)$ if $f(\bar{r})$ satisfies

$$\bar{r}^2(f + \bar{r}f')^2 = (\bar{r}f)^2 - 2M\bar{r}f + a^2, \tag{2.12}$$

or

$$(\bar{r}f')^2 + (2\bar{r}f)f' = -\frac{2Mf}{\bar{r}} + \frac{a^2}{\bar{r}^2}. \tag{2.13}$$

A solution to this equation is

$$r = \bar{r}f(\bar{r}) = (M + \bar{r}) + \frac{M^2 - a^2}{4\bar{r}} \tag{2.14}$$

$$= \bar{r}\left(1 + \frac{M + a}{2\bar{r}}\right)\left(1 + \frac{M - a}{2\bar{r}}\right), \tag{2.15}$$

with constant rescalings of $\bar{r}$ providing the other solutions in general. In the $a = 0$ case, this reduces to the well-known transformation for putting the Schwarzschild metric in isotropic form, $r = \bar{r}(1 + M/2\bar{r})^2$.

After a coordinate change of the Kerr metric in Equation 2.8, we can read off the form of the α potential directly. The remaining potentials are solved for by equating the g_{tt}, $g_{t\phi}$, and $g_{\phi\phi}$ metric components of the transformed Kerr metric and the general metric in Equation 2.3. They are:

$$\alpha = \frac{1}{2}\ln\left[\left(1 + \frac{M + a}{2\bar{r}}\right)^2\left(1 + \frac{M - a}{2\bar{r}}\right)^2 + \frac{a^2}{\bar{r}^2}\cos^2\theta\right] \tag{2.16}$$

$$\gamma = \ln\left[1 - \frac{M^2 - a^2}{4\bar{r}^2}\right] \tag{2.17}$$

$$\rho = \ln\left[\frac{\Sigma r\bar{r}\left(1 - 2M/r + a^2/r^2\right)^{1/2}}{r^4 + a^2\left(\Sigma + r^2\cos^2\theta + 2Mr\sin^2\theta\right)}\right] \tag{2.18}$$

$$\omega = \frac{2Mar}{r^4 + a^2\left(\Sigma + r^2\cos^2\theta + 2Mr\sin^2\theta\right)}. \tag{2.19}$$

Take note that in the above expressions for ρ and ω, both r and $\bar{r}$ appear, which are related by Equation 2.15.

We also need the $\bar{r}$ and θ derivatives of the metric potentials. These are:

$$\alpha_{,\bar{r}} = -\frac{\frac{a^2\cos^2\theta}{\bar{r}^3} + \left(1+\frac{M+a}{2\bar{r}}\right)\left(1+\frac{M-a}{2\bar{r}}\right)\left(\frac{M}{\bar{r}^2}+\frac{M^2-a^2}{2\bar{r}^3}\right)}{\left(1+\frac{M+a}{2\bar{r}}\right)^2\left(1+\frac{M-a}{2\bar{r}}\right)^2 + \frac{a^2}{\bar{r}^2}\cos^2\theta} \tag{2.20}$$

$$\gamma_{,\bar{r}} = \frac{1}{2\bar{r}^3}\left[\frac{M^2-a^2}{1-(M^2-a^2)/(4\bar{r}^2)}\right] \tag{2.21}$$

$$\begin{aligned}\rho_{,\bar{r}} = {} & \frac{2rr_{,\bar{r}}}{\Sigma} + \frac{r_{,\bar{r}}}{r} + \frac{1}{\bar{r}} + \frac{\left(\frac{r_{,\bar{r}}}{r}\right)\left(\frac{M}{r}-\frac{a^2}{r^2}\right)}{1-\frac{2M}{r}+\frac{a^2}{r^2}} \\ & - \frac{r_{,\bar{r}}\left(4r^3+2a^2\left(r(1+\cos^2\theta)+M\sin^2\theta\right)\right)}{r^4+a^2\left(\Sigma+r^2\cos^2\theta+2Mr\sin^2\theta\right)}\end{aligned} \tag{2.22}$$

$$\omega_{,\bar{r}} = -2Mar_{,\bar{r}}\frac{\left[3r^4+a^2\left(r^2+(r^2-a^2)\cos^2\theta\right)\right]}{\left[r^4+a^2\left(\Sigma+r^2\cos^2\theta+2Mr\sin^2\theta\right)\right]^2}, \tag{2.23}$$

with

$$r_{,\bar{r}} = 1-\left(\frac{M+a}{2\bar{r}}\right)\left(\frac{M-a}{2\bar{r}}\right), \tag{2.24}$$

and

$$\alpha_{,\theta} = -\frac{a^2\sin(2\theta)}{2\bar{r}^2\left[\left(1+\frac{M+a}{2\bar{r}}\right)^2\left(1+\frac{M-a}{2\bar{r}}\right)^2+\frac{a^2\cos^2\theta}{\bar{r}^2}\right]} \tag{2.25}$$

$$\gamma_{,\theta} = 0 \tag{2.26}$$

$$\rho_{,\theta} = -a^2\sin(2\theta)\left[\frac{1}{\Sigma}-\frac{r^2+a^2-2Mr}{r^4+a^2\left(\Sigma+r^2\cos^2\theta+2Mr\sin^2\theta\right)}\right] \tag{2.27}$$

$$\omega_{,\theta} = 2Ma^3r\sin(2\theta)\frac{r^2+a^2-2Mr}{\left[r^4+a^2\left(\Sigma+r^2\cos^2\theta+2Mr\sin^2\theta\right)\right]^2}. \tag{2.28}$$

2.3 Null geodesics of the stationary axisymmetric spacetime

2.3.1 Equations of motion

In this section, we discuss how to obtain the description of the light rays from the star's surface to the observer. First we consider the calculation of the null geodesics of the general stationary axisymmetric spacetime of Section 2.2. For a given ray, we wish to obtain the curve $x^a(\lambda)$ describing its path through the spacetime. In

relativity, such curves are geodesics, i.e., they parallel transport their own tangent vectors $\ell^a \equiv \mathrm{d}x^a/\mathrm{d}\lambda$, which means that for an arbitrary parameter λ

$$\ell^a \nabla_a \ell^b \propto \ell^b. \tag{2.29}$$

Such curves can always be reparameterised so that the constant of proportionality in Equation 2.29 is 0,

$$\ell^a \nabla_a \ell^b = 0. \tag{2.30}$$

Equation 2.30 is known as the *geodesic equation.*

Recalling the line element of Equation 2.3,

$$\mathrm{d}s^2 = -e^{\gamma+\rho}\mathrm{d}t^2 + e^{\gamma-\rho}\bar{r}^2 \sin^2\theta(\mathrm{d}\phi - \omega \mathrm{d}t)^2 + e^{2\alpha}(\mathrm{d}\bar{r}^2 + \bar{r}^2 \mathrm{d}\theta^2),$$

we know that since the metric components are independent of the coordinates t and ϕ that the corresponding four-momenta are conserved, $\ell_t \equiv -E$ and $\ell_\phi \equiv L$. This yields the first two equations describing the curves:

$$\ell^t = g^{ta}\ell_a = -e^{-(\gamma+\rho)}\ell_t - \omega e^{-(\gamma+\rho)}\ell_\phi \tag{2.31}$$

$$\ell^\phi = g^{\phi a}\ell_a = -\omega e^{-(\gamma+\rho)}\ell_t + \left[\frac{e^{-\gamma+\rho}}{\bar{r}^2 \sin^2\theta} - \omega^2 e^{-\gamma+\rho}\right]\ell_\phi. \tag{2.32}$$

Defining the "impact parameter" $b \equiv L/E$, and setting $E = 1$ without loss of generality, Equations 2.31 and 2.32 can be written

$$\frac{\mathrm{d}t}{\mathrm{d}\lambda} = e^{-(\gamma+\rho)}(1 - \omega b) \tag{2.33}$$

$$\frac{\mathrm{d}\phi}{\mathrm{d}\lambda} = e^{-(\gamma+\rho)}\left[\omega(1-\omega b) + \frac{b}{e^{-2\rho}\bar{r}^2 \sin^2\theta}\right]. \tag{2.34}$$

The remaining equations are obtained by writing Equation 2.30 in a coordinate basis using the Christoffel symbols Γ^a_{bc}:

$$\ell^a \nabla_a \ell^b = \frac{\mathrm{d}^2 x^b}{\mathrm{d}\lambda^2} + \Gamma^b_{mn}\frac{\mathrm{d}x^m}{\mathrm{d}\lambda}\frac{\mathrm{d}x^n}{\mathrm{d}\lambda} = 0, \tag{2.35}$$

and the Christoffel symbols Γ^a_{bc} are

$$\Gamma^a_{bc} = \frac{1}{2}g^{am}\left(g_{mb;c} + g_{mc;b} - g_{bc;m}\right). \tag{2.36}$$

The Christoffel symbols for the metric we are considering, Equation 2.3, are dis-

played in Table 2.1. Making use of Equations 2.33 and 2.34, we obtain the following two equations from Equation 2.35:

$$\frac{\mathrm{d}^2\theta}{\mathrm{d}\lambda^2} = \alpha_{,\theta}\left(\frac{\dot{\bar{r}}^2}{\bar{r}^2} - \dot{\theta}^2\right) - 2\left(\alpha_{,\bar{r}} + \frac{1}{\bar{r}}\right)\dot{\bar{r}}\dot{\theta} + \frac{1}{2\bar{r}^2}e^{-2\alpha}\mathcal{B}_{,\theta} \tag{2.37}$$

$$\frac{\mathrm{d}^2\bar{r}}{\mathrm{d}\lambda^2} = -\alpha_{,\bar{r}}\left(\dot{\bar{r}}^2 - \bar{r}^2\dot{\theta}^2\right) - 2\alpha_{,\theta}\dot{\bar{r}}\dot{\theta} + \bar{r}\dot{\theta}^2 + \frac{1}{2}e^{-2\alpha}\mathcal{B}_{,\bar{r}}\,, \tag{2.38}$$

where $\dot{\theta} = (\mathrm{d}\theta/\mathrm{d}\lambda)$, and similarly for $\bar{r}$, and we have defined

$$\mathcal{B}(\bar{r},\theta) \equiv e^{-(\gamma+\rho)}(1-\omega b)^2 - \frac{b^2 e^{\rho-\gamma}}{\bar{r}^2\sin^2\theta}. \tag{2.39}$$

With appropriate initial conditions, integration of the Equations 2.33, 2.34, 2.37 and 2.38 yields the points along the curve defining the path of a light ray through the spacetime. These equations are overspecified since we have not yet invoked that the curves must be null, so up to this point these equations are also applicable to both timelike and spacelike geodesics. The question of appropriate initial conditions is addressed in Section 2.3.2.

2.3.2 Initial conditions for null geodesics

We can now specialise to the case of null geodesics by picking appropriate initial conditions. We wish to consider rays which are initially *null*, that is, $\ell^a\ell_a = 0$. This constraint leads to the equation

$$\dot{\bar{r}}^2 + \bar{r}^2\dot{\theta}^2 = e^{-2\alpha}\mathcal{B}(\bar{r},\theta) \equiv \mathcal{A}(\bar{r},\theta). \tag{2.40}$$

When initial conditions for the geodesic are set to obey this *momentum constraint*, the geodesic is initially null and therefore will be null at every point along its path.[2]

In practice, we will have in hand a description $\bar{r}_s(\theta)$ of the location of the star's surface as a function of the colatitude θ. With initial values of $\theta = \theta_i$ and $\bar{r} = \bar{r}_i = \bar{r}_s(\theta_i)$ in hand, the positivity of the right-hand side of Equation 2.40 yields

[2]Differentiating $\ell^b\ell_b$ along the geodesic, we apply the Leibnitz rule to obtain

$$\begin{aligned}\ell^a\nabla_a(\ell^b\ell_b) &= \ell^a\nabla_a\ell^b + \ell^a\nabla_a\ell_b \\ &= \ell^a\nabla_a\ell^b + \ell^a\nabla_a(g_{bc}\ell^c) \\ &= (\ell^a\nabla_a\ell^b) + g_{bc}(\ell^a\nabla_a\ell^c) + \ell^c(\ell^a\nabla_a g_{bc}),\end{aligned}$$

where the first two terms in parentheses are 0 by application of the geodesic equation, and the last is zero by compatibility of the metric with ∇_a.

$$
\begin{aligned}
\Gamma^{t}_{t\bar{r}} &= \frac{1}{2}\left(\gamma_{,\bar{r}} + \rho_{,\bar{r}} - \omega\omega_{,\bar{r}}\, e^{-2\rho}\bar{r}^2 \sin^2\theta\right) \\
\Gamma^{t}_{\bar{r}\phi} &= \frac{1}{2}\omega_{,\bar{r}}\, e^{-2\rho}\bar{r}^2 \sin^2\theta \\
\Gamma^{t}_{\theta\phi} &= \frac{1}{2}\omega_{,\theta}\, e^{-2\rho}\bar{r}^2 \sin^2\theta \\
\Gamma^{\bar{r}}_{tt} &= \frac{1}{2}e^{\gamma+\rho-2\alpha}\left[\gamma_{,\bar{r}}\left(1-\omega^2 e^{-2\rho}\bar{r}\sin^2\theta\right) + \rho_{,\bar{r}}\left(1+\omega^2 e^{-2\rho}\bar{r}\sin^2\theta\right)\right. \\
&\qquad \left. -2\omega e^{-2\rho}\bar{r}^2\sin^2\theta\left(\omega_{,\bar{r}} + \frac{\omega}{\bar{r}}\right)\right] \\
\Gamma^{\bar{r}}_{t\phi} &= \frac{1}{2}e^{\gamma-\rho-2\alpha}\bar{r}^2\sin^2\theta\left[\omega\left(\gamma_{,\bar{r}} - \rho_{,\bar{r}}\right) + \omega_{,\bar{r}} + \frac{2\omega}{\bar{r}}\right] \\
\Gamma^{\bar{r}}_{\bar{r}\bar{r}} &= \alpha_{,\bar{r}} \\
\Gamma^{\bar{r}}_{\bar{r}\theta} &= \alpha_{,\theta} \\
\Gamma^{\bar{r}}_{\phi\phi} &= -\frac{1}{2}e^{\gamma-\rho-2\alpha}\bar{r}^2\sin^2\theta\left(\gamma_{,\bar{r}} - \rho_{,\bar{r}} + \frac{2}{\bar{r}}\right) \\
\Gamma^{\bar{r}}_{\theta\theta} &= -\bar{r}\left(1 + \bar{r}\alpha_{,\bar{r}}\right) \\
\Gamma^{\phi}_{t\bar{r}} &= \omega\left(\rho_{,\bar{r}} - \frac{1}{\bar{r}}\right) - \frac{1}{2}\omega_{,\bar{r}}\left(1+\omega^2 e^{-2\rho}\bar{r}^2\sin^2\theta\right) \\
\Gamma^{\phi}_{t\theta} &= \omega\left(\rho_{,\theta} - \cot\theta\right) - \frac{1}{2}\omega_{,\theta}\left(1+\omega^2 e^{-2\rho}\bar{r}^2\sin^2\theta\right) \\
\Gamma^{\phi}_{\bar{r}\phi} &= \frac{1}{2}\left(\omega\omega_{,\bar{r}}\, e^{-2\rho}\bar{r}^2\sin^2\theta + \gamma_{,\bar{r}} - \rho_{,\bar{r}} + \frac{2}{\bar{r}}\right) \\
\Gamma^{\phi}_{\theta\phi} &= \frac{1}{2}\left(\omega\omega_{,\theta}\, e^{-2\rho}\bar{r}^2\sin^2\theta + \gamma_{,\theta} - \rho_{,\theta} + 2\cot\theta\right) \\
\Gamma^{\theta}_{tt} &= \frac{1}{2\bar{r}^2}e^{\gamma+\rho-2\alpha}\left[\gamma_{,\theta}\left(1-\omega^2 e^{-2\rho}\bar{r}^2\sin^2\theta\right) + \rho_{,\theta}\left(1+\omega^2 e^{-2\rho}\bar{r}^2\sin^2\theta\right)\right. \\
&\qquad \left. -2\omega e^{-2\rho}\bar{r}^2\sin^2\theta\left(\omega_{,\theta} + \omega\cot\theta\right)\right] \\
\Gamma^{\theta}_{t\phi} &= \frac{1}{2}e^{\gamma-\rho-2\alpha}\sin^2\theta\left[\omega\left(\gamma_{,\theta} - \rho_{,\theta}\right) + 2\omega\cot\theta + \omega_{,\theta}\right] \\
\Gamma^{\theta}_{\bar{r}\bar{r}} &= -\frac{\alpha_{,\theta}}{\bar{r}^2} \\
\Gamma^{\theta}_{\bar{r}\theta} &= \frac{1}{\bar{r}} + \alpha_{,\bar{r}} \\
\Gamma^{\theta}_{\phi\phi} &= \frac{1}{2}e^{\gamma-\rho-2\alpha}\sin^2\theta\left(-\gamma_{,\theta} + \rho_{,\theta} - 2\cot\theta\right) \\
\Gamma^{\theta}_{\theta\theta} &= \alpha_{,\theta}
\end{aligned}
$$

Table 2.1: Christoffel symbols for the stationary axisymmetric spacetime.

a constraint on the allowed values of b, $b_- \leq b \leq b_+$, with

$$b_\pm = \pm \frac{e^{-\rho}\bar{r}_i \sin\theta_i}{1 \pm \omega e^{-\rho}\bar{r}_i \sin\theta_i}, \tag{2.41}$$

where the metric potentials are to be evaluated at the initial coordinate. With an initial point and a value of b in hand, we can carry on to calculate the allowed values of $\dot{\theta}_i$. Rewriting the left-hand side of Equation 2.40, we have that

$$\dot{\theta}^2 \left[\left(\frac{\mathrm{d}\bar{r}}{\mathrm{d}\theta} \right)^2 + \bar{r}^2 \right] = \mathcal{A}(\bar{r}, \theta), \tag{2.42}$$

where $\dot{\bar{r}}/\dot{\theta} = \mathrm{d}\bar{r}/\mathrm{d}\theta$. To discover the allowed values of $\dot{\theta}$ requires finding the extremes of the term in parentheses on the left-hand side of Equation 2.42; typically one expects $\dot{\bar{r}} \geq 0$ for outgoing rays, but since we are considering stars that are (perhaps very slightly) oblate, there are certain "glancing" rays with $\dot{\bar{r}}_i < 0$. Figure 2.1 shows the situation for points above and below the equatorial plane in four separate regions where rays can be defined. Using the quantity $\mathcal{A}(\bar{r}, \theta)$ defined in Equation 2.40, choosing the sign of $\pm$ in what follows to match the sign of $\cos\theta_i$, and evaluating all quantities at the initial point, we have the following situations in Figure 2.1:

Region I. Rays with $\dot{\bar{r}}_i < 0$ and $\pm\dot{\theta}_i < 0$. In this region we have

$$\frac{\mathcal{A}}{\bar{r}^2 + (\mathrm{d}\bar{r}_s/\mathrm{d}\theta)^2} \leq \dot{\theta}_i^2 \leq \frac{\mathcal{A}}{\bar{r}^2}. \tag{2.43}$$

This region contains the rays that would be prohibited if the surface of the star was "spherical" with coordinate radius $\bar{r}_s = \text{const}$.

Region II. Rays with $\dot{\bar{r}}_i > 0$ and $\pm\dot{\theta}_i < 0$. In this region,

$$0 \leq \dot{\theta}_i^2 \leq \frac{\mathcal{A}}{\bar{r}^2}. \tag{2.44}$$

Region III. Rays with $\dot{\bar{r}}_i > 0$ and $\pm\dot{\theta}_i > 0$. In this region,

$$0 \leq \dot{\theta}_i^2 \leq \frac{\mathcal{A}}{\bar{r}^2 + (\mathrm{d}\bar{r}_s/\mathrm{d}\theta)^2}. \tag{2.45}$$

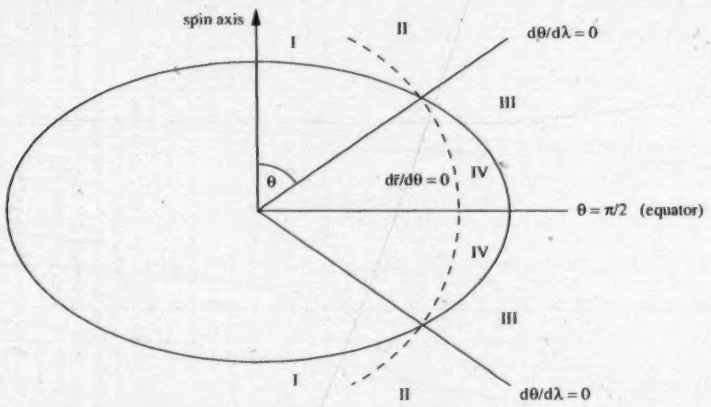

Figure 2.1: Initial conditions for null geodesics originating from an oblate star: This figure is of the $(\bar{r}, \theta)$ plane, where the shaded region represents the volume occupied by an oblate star. The radial coordinate is $\bar{r}$, and the dashed line represents a surface of constant $\bar{r}$. As discussed in the text, determining the allowed values of $\dot{\theta}_i$ and $\dot{\bar{r}}_i$ requires knowing which region, I, II, or III, the particular ray resides in. Region IV describes the initial conditions corresponding to rays which cannot reach the observer since they are initially directed into the star. This figure appears as Figure 1 of Cadeau *et al.* (2006).

Region IV. Rays with $\dot{\bar{r}}_i > 0$ and $\pm\dot{\theta}_i > 0$ are *not* received by the observer when

$$\frac{\mathcal{A}}{\bar{r}^2 + (\mathrm{d}\bar{r}_s/\mathrm{d}\theta)^2} \leq \dot{\theta}_i^2 \leq \frac{\mathcal{A}}{\bar{r}^2}. \tag{2.46}$$

This is the region between a constant $\bar{r}$ surface and the oblate surface of the star where rays would be initially directed into the star and do not reach the observer. The values of $\dot{\theta}_i$ in this region are excluded from the calculation of rays reaching the observer.

With a value of $\dot{\theta}_i$ in hand, the corresponding value of $\dot{\bar{r}}_i$ is fixed by Equation 2.40. If necessary, the sign of $\dot{\bar{r}}_i$ is disambiguated according to which region in Figure 2.1 one is considering.

Integration of a single null ray proceeds by setting the initial coordinates $\bar{r}_i$ and θ_i, selecting an allowed value of b, selecting an allowed value $\dot{\theta}_i$ according to the above prescription of the geometric constraints, and fixing $\dot{\bar{r}}_i^2$ and the sign of $\dot{\bar{r}}_i$ by the momentum and geometric constraints. The differential equations 2.33, 2.34, 2.37, and 2.38 are then integrated numerically. In principle it would be possible to reduce the number of equations to be integrated by computing $\dot{\bar{r}}$ from $\dot{\theta}$ via

the momentum constraint. However, it is a useful diagnostic to keep track of the momentum constraint as a check on the integration code.

2.3.3 Redshift

The redshift, z, of photons is defined as

$$1 + z = \frac{\nu_{\rm emit}}{\nu_{\rm obs}}, \tag{2.47}$$

where the energies of emitted and received photons are $h\nu_{\rm emit}$ and $h\nu_{\rm obs}$ respectively. Suppose that a photon is emitted at coordinates $\theta = \theta_i$ and $\bar{r} = \bar{r}_s(\theta_i)$ in a frame with four-velocity u^a, and received at coordinates $\theta = \theta_f$, $\bar{r} = \bar{r}_f$ in a frame with four-velocity w^a. Then if p^a is the four-momentum of the photon, $h\nu_{\rm emit} = -u^a p_a$, with the inner product evaluated at the emission point. Similarly, $h\nu_{\rm obs} = -w^a p_a$, with the inner product evaluated at the observation point. In practice we are concerned with photons emitted from a frame with $u^a \propto (t^a + \Omega_\star \phi^a)$, where $\Omega_\star$ is the angular velocity of the star as measured at infinity. If $u^a = (t^a + \Omega_\star \phi^a)/V$, then using the normalisation $u^a u_a = -1$ we have

$$V^2 = e^{\gamma+\rho}\left[1 - (\Omega_\star - \omega)^2\, e^{-2\rho}\bar{r}^2 \sin^2\theta\right]. \tag{2.48}$$

Similarly, the observation frame has $w^a = t^a/W$, with

$$W^2 = e^{\gamma+\rho}\left[1 - \omega^2 e^{-2\rho}\bar{r}^2 \sin^2\theta\right]. \tag{2.49}$$

Evaluating the inner products, we have that along a null ray with impact parameter b that the redshift is

$$1 + z = (1 - b\Omega_\star)\left\{\frac{e^{(\gamma+\rho)_{\rm obs}}\left[1 - \omega^2 e^{-2\rho}\bar{r}^2 \sin^2\theta\right]_{\rm obs}}{e^{(\gamma+\rho)_{\rm emit}}\left[1 - (\Omega_\star - \omega)^2\, e^{-2\rho}\bar{r}^2 \sin^2\theta\right]_{\rm emit}}\right\}^{1/2}. \tag{2.50}$$

A zero angular momentum observer (ZAMO) will measure the velocity of the fluid at the star's surface to have speed

$$v_Z = (\Omega_\star - \omega) e^{-\rho}\bar{r} \sin\theta, \tag{2.51}$$

and in the case of a distant observer, the numerator of Equation 2.50 goes to 1. So

for a distant observer, the redshift can be written

$$1 + z = e^{-(\gamma+\rho)} \frac{1 - \Omega_\star b}{\sqrt{1 - v_Z^2}}. \tag{2.52}$$

2.3.4 Zenith angle

In general the intensity I_{ν_e} will depend on the *zenith angle* of the emitted photons, α_e; this is the angle the emitted ray forms with the normal n^a to the star's surface in the emission frame. In the case where we have solved for the stellar structure and metric potentials exactly, n^a is parallel to the four-acceleration of a fluid element at the surface.[3] However, we will also be considering cases where we invoke approximate solutions for the metric and stellar structure, and in these cases we will want to consider n^a as arising solely from where we are positing the location of the $p = 0$ surface without relying on Euler's equation being satisfied; we will call this the *geometric normal* to the star's surface. In the following sections we will develop these two different notions of the normal vector at the surface, establish how they differ, and set out the definition of the zenith angle.

Four-acceleration of fluid elements

The four-acceleration $a^b \equiv u^c \nabla_c u^b$ can be calculated by using the fact that the four-velocities of the fluid elements u^a are proportional to the Killing vector field $\xi^a \equiv (t^a + \Omega_\star \phi^a)$, with $u^a = \xi^a / V$ and V defined by $V^2 = -\xi^a \xi_a$, which is written in terms of the metric components and $\Omega_\star$ in Equation 2.48. The Killing vector ξ^a satisfies Killing's Equation:

$$\nabla_a \xi_b + \nabla_b \xi_a = 0. \tag{2.53}$$

Starting with the definition of a^b, we have:

$$\begin{aligned}
a^b &= u^a \nabla_a u^b \\
(u^a \text{ is parallel to } \xi^a) \quad &= \left(\frac{1}{V}\xi^a\right) \nabla_a \left(\frac{1}{V}\xi^b\right) \\
(\text{Leibnitz rule for } \nabla) \quad &= \frac{1}{V}\xi^a \left(\xi^b \nabla_a \frac{1}{V} + \frac{1}{V}\nabla_a \xi^b\right) \\
&= \frac{1}{V}\xi^b \xi^a \nabla_a \frac{1}{V} + \frac{1}{V^2}\xi^a \nabla_a \xi^b
\end{aligned}$$

[3] This is a consequence of Euler's equation for perfect fluids, $-(\rho + p)u^a \nabla_a u^b = \nabla^b p + (u^a \nabla_a p)\, u^b$. The left-hand side concerns the four-acceleration $u^a \nabla_a u^b$. In an equilibrium configuration, the pressure does not change along a flow line, so $u^a \nabla_a p = 0$. Therefore the four-acceleration is proportional to the gradient of pressure, which is the same as saying that the four-acceleration is parallel to the normal n^a.

$$\begin{aligned}
\text{(Chain rule)} \quad &= \frac{1}{V}\xi^b\xi^a\left(-\frac{1}{V^2}\nabla_a V\right)+\frac{1}{V^2}\xi^a\nabla_a\xi^b \\
&= -\frac{1}{V^3}\xi^b\xi^a\nabla_a V+\frac{1}{V^2}\xi^a\nabla_a\xi^b. \qquad (2.54)
\end{aligned}$$

Let us consider the terms in Equation 2.54 separately. First, we know that the term containing

$$\xi^a\nabla_a V=0, \qquad (2.55)$$

since ξ^a generates isometries of the spacetime, and V involves only metric components and quantities that don't change in the direction of ξ^a (i.e., V does not depend on either t or ϕ). Next we work out the second term in Equation 2.54:

$$\begin{aligned}
\frac{1}{V^2}\xi^a\nabla_a\xi^b &= \frac{1}{V^2}\xi^a\nabla_a\left(g^{bc}\xi_c\right) \\
\text{(Leibnitz and compatibility of } g_{ab} \text{ and } \nabla) \quad &= \frac{1}{V^2}\xi^a g^{bc}\nabla_a\xi_c \\
\text{(Applying Killing's Equation)} \quad &= -\frac{1}{V^2}\xi^a g^{bc}\nabla_c\xi_a \\
&= -\frac{1}{V^2}\xi^a\nabla^b\xi_a. \qquad (2.56)
\end{aligned}$$

From here in, rather than saying "Leibnitz and compatibility of g_{ab} and ∇," notice that these rules amount to a statement of commutativity of g_{ab} with ∇. Consider the term $\xi^a\nabla^b\xi_a$:

$$\begin{aligned}
\xi^a\nabla^b\xi_a &= \frac{1}{2}\xi^a\nabla^b\xi_a+\frac{1}{2}\xi^a\nabla^b\xi_a \\
\text{(Inserting Kronecker)} \quad &= \frac{1}{2}\xi^a\nabla^b\xi_a+\frac{1}{2}g^a{}_c\xi^c\nabla^b\xi_a \\
\text{(Expanding Kronecker)} \quad &= \frac{1}{2}\xi^a\nabla^b\xi_a+\frac{1}{2}g^{ad}g_{dc}\xi^c\nabla^b\xi_a \\
(g_{ab} \text{ and } \nabla \text{ commute}) \quad &= \frac{1}{2}\xi^a\nabla^b\xi_a+\frac{1}{2}g_{dc}\xi^c\nabla^b\left(g^{ad}\xi_a\right) \\
&= \frac{1}{2}\xi^a\nabla^b\xi_a+\frac{1}{2}\xi_d\nabla^b\xi^d \\
\text{(Relabelling)} \quad &= \frac{1}{2}\xi^a\nabla^b\xi_a+\frac{1}{2}\xi_a\nabla^b\xi^a \\
\text{(Leibnitz rule)} \quad &= \frac{1}{2}\nabla^b\left(\xi^a\xi_a\right) \\
\text{(Definition of } V^2) \quad &= -\frac{1}{2}\nabla^b\left(V^2\right) \\
\text{(Chain rule)} \quad &= -V\nabla^b V. \qquad (2.57)
\end{aligned}$$

Inserting Equation 2.57 into Equation 2.56, we obtain:

$$\begin{aligned} \frac{1}{V^2}\xi^a\nabla_a\xi^b &= -\frac{1}{V^2}\xi^a\nabla^b\xi_a \\ &= \frac{1}{V}\nabla^b V \\ \text{(Chain rule)} &= \nabla^b(\ln V)\,. \end{aligned} \tag{2.58}$$

Inserting Equations 2.55 and 2.58 into Equation 2.54, one obtains

$$a^b = \nabla^b(\ln V)\,. \tag{2.59}$$

This is the four-acceleration of a fluid element (or co-rotating observer), with V defined in Equation 2.48. For the general stationary axisymmetric metric, Equation 2.3, the components of the four-acceleration are:

$$\begin{aligned} a^{\bar{r}} &= \frac{g^{\bar{r}\bar{r}}}{2V^2}\nabla_{\bar{r}}(V^2) \\ &= \frac{1}{2}e^{-2\alpha}\left(\gamma_{,\bar{r}}+\rho_{,\bar{r}}\right) \\ &\quad +\frac{1}{V^2}e^{\gamma+\rho-2\alpha}\left[(\Omega_\star-\omega)e^{-2\rho}\bar{r}\sin^2\theta\left(\bar{r}\omega_{,\bar{r}}+(\Omega_\star-\omega)(\bar{r}\rho_{,\bar{r}}-1)\right)\right] \end{aligned} \tag{2.60}$$

$$\begin{aligned} a^{\theta} &= \frac{g^{\theta\theta}}{2V^2}\nabla_{\theta}(V^2) \\ &= \frac{1}{2\bar{r}^2}e^{-2\alpha}\left(\gamma_{,\theta}+\rho_{,\theta}\right) - \frac{1}{V^2}e^{\gamma-\rho-2\alpha} \\ &\quad \times\left[(\Omega_\star-\omega)\sin\theta\left(\omega_{,\theta}\sin\theta+(\Omega_\star-\omega)(\cos\theta-\rho_{,\theta}\sin\theta)\right)\right]. \end{aligned} \tag{2.61}$$

Direction of normal as defined by surface

We define the geometric normal to the surface by starting with the coordinate position of the surface $\bar{r}_s(\theta)$. A tangent to this surface is the vector s^a with non-zero components

$$s^{\bar{r}} = \frac{\mathrm{d}\bar{r}_s}{\mathrm{d}\theta} \tag{2.62}$$

$$s^{\theta} = 1. \tag{2.63}$$

The geometric normal to this surface is defined via $s_a n^a = 0$; non-zero components of the normal vector are therefore

$$n^{\bar{r}} = 1 \tag{2.64}$$

$$n^\theta = -\frac{1}{\bar{r}_s^2}\frac{\mathrm{d}\bar{r}_s}{\mathrm{d}\theta}. \tag{2.65}$$

With two methods available to determine the direction of the normal at the surface of the star, we obtain a check on subsequent numerical calculations by ensuring that these directions do coincide in the exact case, since they come from quantities that will be independently specified. In some of the approximate treatments we will investigate, we will break the solution of Euler's equation and one needs to be careful about which direction is meant by the normal, i.e., whether it should be defined by the direction of force at the star's surface, or whether it should be defined by the shape of the embedded surface.

Angle between null geodesic and the normal n^a in the co-rotating frame (Zenith angle)

Once a specification for the direction of the normal n^a is chosen, we wish to know the angle α_e formed between the ray ℓ^a and the normal in the emission frame so that anisotropic emissitivities can, in principle, be included in the calculation. The measurement of angles is an observer dependent procedure. In this case, we wish to know the angle measured by an observer with $u^a = (t^a + \Omega_\star \phi^a)/V$, i.e., one co-rotating with the star. The angle α_e between these is given by the usual "cos angle" relation where

$$\cos\alpha_e = \frac{\tilde{\ell}^a \tilde{n}_a}{|\tilde{\ell}^a||\tilde{n}^a|}, \tag{2.66}$$

and the tildes indicate that the vectors have been projected into the space orthogonal to u^a by contracting with the projection operator $h_{ab} \equiv u_a u_b + g_{ab}$. A more compact way of writing this is by noticing that h_{ab} is just the metric on the three-surface orthogonal to u^a, so we can write

$$\cos\alpha_e = \frac{h_{ab}\ell^a n^b}{|\ell^a|_h |n^a|_h}, \tag{2.67}$$

where the subscripted h in the denominator serves to remind that we want the lengths of the projected vectors. This simplifies to

$$\cos\alpha_e = V e^\alpha \frac{\dot{\bar{r}} n^{\bar{r}} + \bar{r}^2 \dot{\theta} n^\theta}{(1 - \Omega_\star b)\left((n^{\bar{r}})^2 + \bar{r}^2 (n^\theta)^2\right)^{1/2}}, \tag{2.68}$$

where everything is evaluated at the emission point and the dotted quantities refer to the initial conditions for the null geodesic as discussed in Section 2.3.2, and the

components of n^a are obtained by one of the two methods given above.

Angle between null geodesic and the normal n^a in the observer's frame

In a similar fashion to what was done for the zenith angle as measured in the emission frame, another calculation can be carried out for an observer with four-velocity $w^a = t^a/W$ at the surface, where W^2 is defined in Equation 2.49. One obtains

$$\cos\alpha_o = We^\alpha \frac{\dot{\bar{r}}n^{\bar{r}} + \bar{r}^2\dot{\theta}n^\theta}{((n^{\bar{r}})^2 + \bar{r}^2(n^\theta)^2)^{1/2}}. \tag{2.69}$$

2.4 Calculation of light curve

To complete our treatment of the light curve calculation, we devise a means by which to determine the solid angle $\mathrm{d}\Omega$ subtended by an emission region in a distant observer's sky for a non-moving emitter (Section 2.4.1), and the manner in which Equation 2.1 should be adjusted to account for the motion of an emitting region around the star (Section 2.4.2). The section concludes with a listing of the steps we will follow to compute the light curve.

2.4.1 Solid angle

Consider a distant observer who sees an infinitesimal rectangular emission region as described in Figure 2.2 and the accompanying caption. We take each side of the emission region to appear as a line segment in the observer's sky; the length of the line segment $\mathrm{d}l = D\,\mathrm{d}\varepsilon$, where D is the radius of the observer's sky and $\mathrm{d}\varepsilon$ is the angle formed between the two corresponding rays as measured by the distant observer. Since we can calculate the length of each side, it is possible to calculate the apparent area $\mathrm{d}A$ of the emission region; the solid angle subtended by the emission region $\mathrm{d}\Omega = \mathrm{d}A/D^2$.

To begin with we need to establish the angle between two null rays ℓ^a and m^a as measured by a distant observer with four-velocity $u^a = t^a/W$, where W is defined by $W^2 = -g_{tt}$. Say that $\ell_\phi/(-\ell_t) = b$, and $m_\phi/(-m_t) = c$. Starting with the same relation as with the zenith angle calculation, we have that

$$\begin{aligned}\cos\mathrm{d}\varepsilon &= \frac{h_{ab}\ell^a m^b}{|\ell^a|_h|m^a|_h} \\ &= 1 + (-g_{tt})\left[g^{tt} - (b+c)g^{t\phi} + bcg^{\phi\phi} + g_{\bar{r}\bar{r}}\left(\frac{\ell^{\bar{r}}}{-\ell_t}\right)\left(\frac{m^{\bar{r}}}{-m_t}\right)\right.\end{aligned}$$

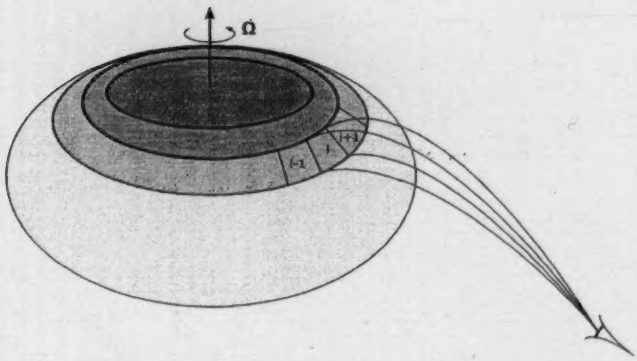

Figure 2.2: To calculate the solid angle subtended by the emission region in the observer's sky, we consider a small rectangle of angular size $\mathrm{d}\theta \times \mathrm{d}\phi$. If we know which rays reach from the corners of the rectangle to the observer, it is possible to calculate the area of the rectangle as seen by the observer. Labels $i-1$, i, and $i+1$ indicate neighbouring regions with the same angular size in anticipation of the eventual discretisation of the calculation.

$$+g_{\theta\theta}\left(\frac{\ell^\theta}{-\ell_t}\right)\left(\frac{m^\theta}{-m_t}\right)\Bigg]. \tag{2.70}$$

Now let $c = b+\mathrm{d}b$, $m^{\bar{r}}/(-m_t) = (\ell^{\bar{r}}/(-\ell_t))+\mathrm{d}\ell^{\bar{r}}$, and $m^\theta/(-m_t) = (\ell^\theta/(-\ell_t)) + \mathrm{d}\ell^\theta$. Continuing on from Equation 2.70, we have

$$\begin{aligned}\cos\mathrm{d}\varepsilon &= 1+(-g_{tt})\Bigg[\underline{g^{tt}-2bg^{t\phi}} - \mathrm{d}bg^{t\phi}\underline{+b^2g^{\phi\phi}} + b\mathrm{d}bg^{\phi\phi}\underline{+\left(\frac{\ell^{\bar{r}}}{-\ell_t}\right)^2 g_{\bar{r}\bar{r}}} \\ &\quad +\mathrm{d}\ell^{\bar{r}}\left(\frac{\ell^{\bar{r}}}{-\ell_t}\right)g_{\bar{r}\bar{r}}\underline{+\left(\frac{\ell^\theta}{-\ell_t}\right)^2 g_{\theta\theta}} + \mathrm{d}\ell^\theta\left(\frac{\ell^\theta}{-\ell_t}\right)g_{\theta\theta}\Bigg]. \end{aligned}\tag{2.71}$$

The underlined terms in this equation are essentially $\ell_a\ell^a$, so they vanish. Equation 2.71 is exact; we haven't done anything that is only first-order in $\mathrm{d}b$, $\mathrm{d}\ell^{\bar{r}}$, or $\mathrm{d}\ell^\theta$. To simplify the remaining terms square brackets, we start with $m_am^a = 0$, which after using $\ell_a\ell^a = 0$ again, becomes

$$\begin{aligned}0 &= -2\mathrm{d}bg^{t\phi} + 2b\mathrm{d}bg^{\phi\phi} + (\mathrm{d}b)^2g^{\phi\phi} + g_{\bar{r}\bar{r}}\left[2\mathrm{d}\ell^{\bar{r}}\left(\frac{\ell^{\bar{r}}}{-\ell_t}\right) + (\mathrm{d}\ell^{\bar{r}})^2\right] \\ &\quad +g_{\theta\theta}\left[2\mathrm{d}\ell^\theta\left(\frac{\ell^\theta}{-\ell_t}\right) + (\mathrm{d}\ell^\theta)^2\right]. \end{aligned}\tag{2.72}$$

We expect $\mathrm{d}\varepsilon$ to be small for a distant observer, so it is appropriate to use the approximation $\cos\mathrm{d}\varepsilon = 1 - \mathrm{d}\varepsilon^2/2 + \mathcal{O}(\mathrm{d}\varepsilon^4)$. Together, Equations 2.71 and 2.72 yield

$$\mathrm{d}\varepsilon^2 + \mathcal{O}(\mathrm{d}\varepsilon^4) = (-g_{tt})\left[g^{\phi\phi}(\mathrm{d}b)^2 + g_{\bar{r}\bar{r}}(\mathrm{d}\ell^{\bar{r}})^2 + g_{\theta\theta}(\mathrm{d}\ell^\theta)^2\right]. \tag{2.73}$$

Finally, we can use the momentum constraint $m_am^a = 0$ to eliminate one of the quantities $\mathrm{d}b$, $\mathrm{d}\ell^{\bar{r}}$ or $\mathrm{d}\ell^\theta$. Since far from the star most of the motion will be radial, it is best to write $\mathrm{d}\ell^{\bar{r}}$ in terms of the other quantities. To first order in the differentials, the relation between these quantities is

$$\mathrm{d}\ell^{\bar{r}} = -\frac{1}{(\ell^{\bar{r}}/(-\ell_t))}\left[\bar{r}^2\left(\frac{\ell^\theta}{-\ell_t}\right)\mathrm{d}\ell^\theta + e^{-\gamma-\rho-2\alpha}\left(\omega(1-\omega b) + \frac{b}{(e^{-\rho}\bar{r}\sin\theta)^2}\right)\mathrm{d}b\right]. \tag{2.74}$$

Considering Figure 2.2, Equation 2.73 allows us to calculate six lengths (four sides, and two diagonals) in the observed image of the emission region by calculating the angles formed by pairs of null rays as measured by the observer. The observed area of the emission region can be calculated by choosing a diagonal of the emission region and calculating the areas of the two triangles which comprise the image using, e.g., Heron's formula for the area of a triangle, which says that a triangle with side

lengths u, v, w and semi-perimeter $s \equiv (u+v+w)/2$ is

$$A = \sqrt{s(s-u)(s-v)(s-w)}. \tag{2.75}$$

Equivalently, the solid angle subtended by the triangle can be calculated using this formula where u, v, and w are angles computed via Equation 2.73.

2.4.2 Calculation of light curve including arrival time effects

For a precise calculation of the light curve, one must account for the fact that the time-of-flight of photons from the star to a distant observer is not constant over the visible surface of the star. This is particularly important for the case of the millisecond-period pulsars, as the light-crossing time of the neutron star reaches a significant fraction of the rotational period—up to about 5% for a pulsar with the shortest known rotational period, and the maximum likely size of neutron stars. A second effect that needs to be considered results from the motion of the emitting area, as one needs to account for the difference between emitted and observed time intervals. The first problem is easy to deal with since the times-of-flight are calculable from the equations of motion. The second problem is more subtle, and impacts the manner in which the observed flux should be calculated. It was similar considerations that led Penrose (1959) and Terrell (1959) to observe nearly 50 years after the publication of the theory of special relativity that rapidly moving extended objects in flat space are not observed contracted, but rotated, contrary to the expectations of Einstein and Lorentz. This result can be arrived at by carefully considering which photons from the object are arriving at an observer at a given instant. In this section we discuss the effect of the motion of the emitting region on the observed light curve.

To calculate the flux arriving at the observer at time t_o, we need to integrate the flux arriving from the visible part of the emission region at the instant the observation is made; that is,

$$F_{\nu_o}(t_o) = \int \mathrm{d}\phi \frac{\mathrm{d}\Omega}{\mathrm{d}\phi} \frac{I_{\nu_e}}{(1+z)^3}, \tag{2.76}$$

where the integral is taken over those coordinates on the star labelled by ϕ which are visible to the observer at the instant of observer proper time t_o.

To determine which regions of the star are visible to the observer at a given instant, we consider an emission region comoving with the star which has constant angular width $\Delta\phi'_e$ in the star's rest frame, located at some constant latitude θ.

In the observer's frame, the emission region is seen to be moving with angular velocity $\Omega_\star$ as measured at infinity. In the observer's frame *at the surface*, the emission region is Lorentz contracted and an observer at the surface will infer that the emission region has width $\Delta\phi_e = (\Delta\phi'_e)/\Gamma$, where the boost factor Γ and the observed speed v of the star at the emission region are

$$\Gamma = (1-v^2)^{-1/2}, \text{and} \tag{2.77}$$

$$v = \frac{\Omega_\star e^{-\rho}\bar{r}\sin\theta}{1+\omega(\Omega_\star-\omega)e^{-2\rho}\bar{r}^2\sin^2\theta}. \tag{2.78}$$

As depicted in Figure 2.3, in the observer's frame at the surface of the star, such an emission region has the property that points located at the coordinate ϕ are illuminated between coordinate times $t_{e_1} \le t \le t_{e_2}$, with

$$t_{e_1} \equiv \Omega_\star^{-1}(\phi - (\Delta\phi_e/2)), \text{ and} \tag{2.79}$$

$$t_{e_2} \equiv \Omega_\star^{-1}(\phi + (\Delta\phi_e/2)). \tag{2.80}$$

Denoting by $T(\phi)$ the lapse of coordinate time required for a photon to travel between the emission point at ϕ and the observer, we have that the light emitted from ϕ is observed between coordinate times (and so, observer proper times) $t_{o_1} \le t \le t_{o_2}$, with $t_{o_1} = t_{e_1} + T(\phi)$ and similarly for t_{o_2}. To determine what portion of the emission region is visible to an observer at time t_o, we need to determine the set of points labelled by ϕ that satisfy the inequalities

$$T(\phi) + \Omega_\star^{-1}(\phi - (\Delta\phi/2)) \le t_o \le T(\phi) + \Omega_\star^{-1}(\phi + (\Delta\phi/2), \tag{2.81}$$

i.e., those points which are emitting light over an interval which will be received in an interval containing $t = t_o$. To solve for these points, first consider that $T(\phi)$ can be approximated by

$$T(\phi) \approx T(\phi_o) + \left.\frac{\mathrm{d}T}{\mathrm{d}\phi}\right|_{\phi=\phi_o} (\phi - \phi_o), \tag{2.82}$$

where ϕ_o is defined as the solution to

$$t_o = \Omega_\star^{-1}\phi_o + T(\phi_o); \tag{2.83}$$

ϕ_o corresponds to the ϕ coordinate that continues to be observable at time t_o in

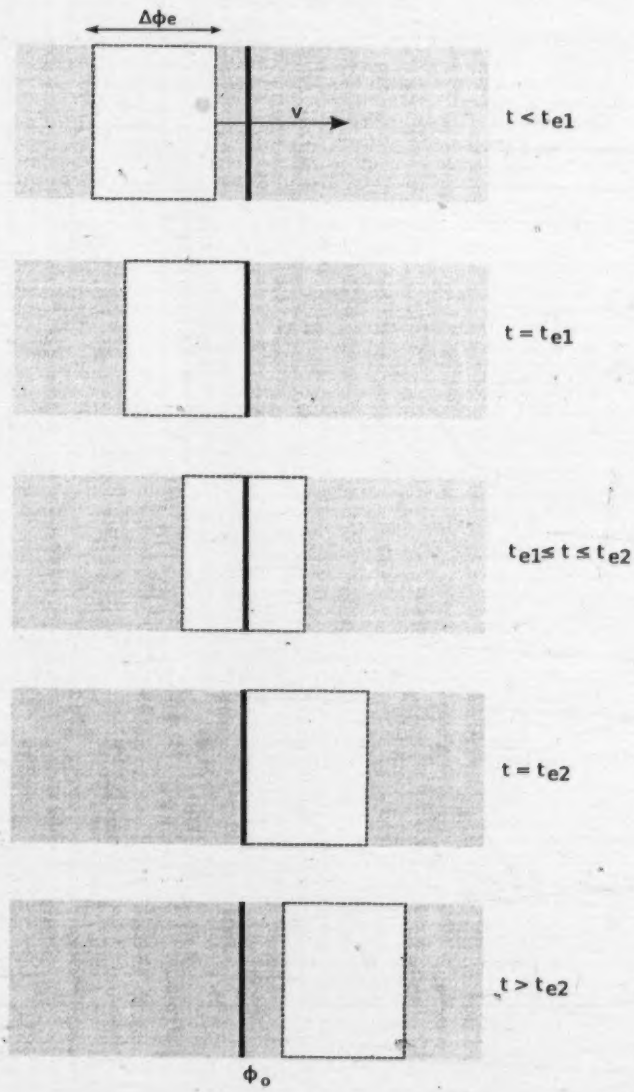

Figure 2.3: An emission region of width $\Delta\phi_e$ as seen in the observer's frame at the surface of the star can be realised by considering that the points located at coordinate ϕ (represented by the bold line), are illuminated between coordinate times $t_{e_1} \equiv \Omega_\star^{-1}(\phi - (\Delta\phi_e/2))$ and $t_{e_2} \equiv \Omega_\star^{-1}(\phi + (\Delta\phi_e/2))$.

the limit of ever smaller emission regions. The inequalities in Equation 2.81 have the solution

$$-\frac{(\Delta\phi_e/2)}{1+\Omega_\star \mathrm{d}T/\mathrm{d}\phi|_{\phi=\phi_o}} \leq \phi - \phi_o \leq \frac{(\Delta\phi_e/2)}{1+\Omega_\star \mathrm{d}T/\mathrm{d}\phi|_{\phi=\phi_o}}. \tag{2.84}$$

These are the visible coordinates at an instant of observer time, given an emission region of fixed angular size $\Delta\phi_e$ in the observer's frame at the surface. The visible region is centred on the coordinate ϕ_o, which is defined via Equation 2.83. This result says that if the times of flight are growing (respectively, shrinking) as the emission region moves that this has the effect of narrowing (widening) the visible size of the emission region as determined by an instantaneous observation by the distant observer.

To evaluate the integral for flux in Equation 2.76, we make the assumption that the integrand is approximately constant (i.e., that $\Delta\phi'_e$ is small), and so

$$F_{\nu_o}(t_o) = \Delta\phi_o \left.\frac{\mathrm{d}\Omega}{\mathrm{d}\phi}\right|_{\phi=\phi_o} \frac{I_{\nu_e}(\phi_e)}{(1+z(\phi_o))^3} \tag{2.85}$$

$$= \frac{\Delta\phi'_e/\Gamma}{1+\Omega_\star \mathrm{d}T/\mathrm{d}\phi|_{\phi=\phi_o}} \left.\frac{\mathrm{d}\Omega}{\mathrm{d}\phi}\right|_{\phi=\phi_o} \frac{I_{\nu_e}(\phi_o)}{(1+z(\phi_o))^3}, \tag{2.86}$$

where the last line makes use of the result in Equation 2.84. In this form, the light curve of an infinitesimal emission region is calculable by chosing a coordinate ϕ_o, and following these steps:

1. Calculate t_o via Equation 2.83.

2. Calculate the term $1+\Omega_\star \mathrm{d}T/\mathrm{d}\phi|_{\phi=\phi_o}$. In practice this was done numerically by centred finite differences to calculate the derivative of T using neighbouring rays. However, we show below that this term has a general simple expression in terms of b and $\Omega_\star$, which obviates the need to calculate the derivative numerically.

3. Calculate $\mathrm{d}\Omega/\mathrm{d}\phi|_{\phi=\phi_o}$ by approximating it as the quotient $\Delta\Omega/\Delta\phi_e$, where $\Delta\Omega$ is the solid angle subtended in the observer's sky by photons emitted at the same time from a rectangular emission region of width $\Delta\phi_e$ and height $\Delta\theta$. The emission region is centred on $\phi = \phi_o$, as depicted in Figure 2.2. The quantity $\Delta\Omega$ can be calculated by following the method prescribed in Section 2.4.1, which is to calculate the apparent size of the rectangle observed by a distant observer. A second method, set out in Section 2.5 is available for

the Schwarzschild spacetime where spherical symmetry allows us to describe areas on the distant observer's sky in simpler terms.

4. Calculate the redshift z of the rays emitted from $\phi = \phi_o$ via Equation 2.50. This also is required to determine ν_o from ν_e, if spectral effects are to be included.

5. If the emission is anisotropic, $I(\phi_o)$ should be calculated according to the prescription of anisotropy using the zenith angle of the rays emitted from ϕ_o, which is set out Section 2.3.4.

All elements of this calculation require knowing the actual rays joining points on the star with the observer. Solving for these rays is dealt with numerically, using the method described in Chapter 3.

It is possible to understand the factor $1 + \Omega_\star \mathrm{d}T/\mathrm{d}\phi|_{\phi=\phi_o}$ appearing in Equation 2.86 in terms of comparing intervals of emitted and received proper times: An observer corotating with the emission region at the surface of the star measures intervals of proper time according to

$$\mathrm{d}\tau_e^2 = V_e^2 \mathrm{d}t^2, \tag{2.87}$$

where V_e^2 is evaluated at the point of emission according to Equation 2.48. For an observer being held at the same spatial coordinates, the proper time interval is

$$\mathrm{d}\tau_o^2 = W_o^2 \mathrm{d}t^2, \tag{2.88}$$

where W_o^2 is evaluated at the observer's coordinates according to Equation 2.49. At large $\bar{r}$, $W^2 \approx 1$ and $\tau_o \approx t_o$. However our calculations are concerned with comparing the emitted and observed intervals of proper time *joined by photons emitted from a moving surface*, so it is also necessary to introduce a third quantity, τ_r: the proper time at which a photon emitted at τ_e is received, as measured on the distant observer's clock. Using $t_o = t_e + T$ from the discussion above, we have $\tau_r = \tau_e/V + T(\tau_e)$. So we have that the term $1 + \Omega_\star \mathrm{d}T/\mathrm{d}\phi|_{\phi=\phi_o}$ appearing in Equation 2.86 can be written as

$$1 + \Omega_\star \mathrm{d}T/\mathrm{d}\phi|_{\phi=\phi_o} = \frac{\mathrm{d}t_o}{\mathrm{d}t_e} \tag{2.89}$$

$$= \frac{\mathrm{d}\tau_r/W}{\mathrm{d}\tau_e/V} \tag{2.90}$$

$$= \frac{\mathrm{d}\tau_r/\mathrm{d}\tau_e}{\mathrm{d}\tau_o/\mathrm{d}\tau_e}, \tag{2.91}$$

where between Equations 2.90 and 2.91 we made use of Equations 2.87 and 2.88. This result says that the term correcting the visible size of the extended emission region is: the rate at which the receiving times τ_r measured by the distant observer change per unit of proper time in the emission frame, divided by a factor which is the rate the observer's clock runs at per unit of proper time in the emission frame, $\mathrm{d}\tau_o/\mathrm{d}\tau_e$.

We will show at the end of Section 2.5 that the overall factor of $\Gamma(1+\Omega_\star \mathrm{d}T/\mathrm{d}\phi_{\phi=\phi_o})$ is similar to the "Doppler factor" of special relativity, defined as

$$1/\delta \equiv \Gamma(1 - v\cos\xi), \tag{2.92}$$

where ξ is the angle formed by photons reaching the observer with the extended object's velocity vector in the observer's frame (Ghisellini, 1999; Leahy, 2003b). According to special relativity, an emitting area $\mathrm{d}S'$ moving with respect to a distant observer is observed to have area $\mathrm{d}S = \delta \mathrm{d}S'$ in a "snapshot" where one captures the photons reaching the observer at the same instant in time (Terrell, 1959). The above argument shows the sense in which our observer will observe the same effect for a moving emission region when gravity is involved.

Analytical form of $1 + \Omega_\star \mathrm{d}T/\mathrm{d}\phi$

Morsink (2005b) observed that the derivative $\mathrm{d}T/\mathrm{d}\phi$, where ϕ is the azimuthal deflection of a light ray, has a surprisingly simple form in general. This leads to a simplification of the term $1 + \Omega_\star \mathrm{d}T/\mathrm{d}\phi$. To see this, we can begin with the momentum constraint, Equation 2.40, and define new quantities $\dot{s}$ and $h(b)$ according to

$$\dot{s}^2 \equiv \dot{\bar{r}}^2 + \bar{r}^2\dot{\theta}^2 = e^{-\gamma-\rho-2\alpha}h(b), \text{ with} \tag{2.93}$$

$$h(b) \equiv (1-\omega b)^2 - \frac{b^2}{e^{-2\rho}\bar{r}^2\sin^2\theta}. \tag{2.94}$$

The derivatives of $h(b)$ satisfy

$$\frac{\mathrm{d}h}{\mathrm{d}b} = -2\left[\omega(1-\omega b) + \frac{b}{e^{-2\rho}\bar{r}^2\sin^2\theta}\right] \tag{2.95}$$

$$\frac{\mathrm{d}^2h}{\mathrm{d}b^2} = -2\left[-\omega^2 + \frac{1}{e^{-2\rho}\bar{r}^2\sin^2\theta}\right] \tag{2.96}$$

$$h - \frac{b}{2}\frac{\mathrm{d}h}{\mathrm{d}b} = (1 - \omega b) \tag{2.97}$$

$$\frac{\mathrm{d}h}{\mathrm{d}b} - b\frac{\mathrm{d}^2 h}{\mathrm{d}b^2} = -2\omega. \tag{2.98}$$

Reparameterising the equations of motion for the t and ϕ coordinates (Equations 2.33 and 2.34) by s, which is the coordinate length of the geodesic projected into the $(\bar{r}, \theta)$ coordinate plane, we obtain

$$\frac{\mathrm{d}t}{\mathrm{d}s} = e^{\alpha-(\gamma+\rho)/2}\frac{1-\omega b}{h^{1/2}}, \tag{2.99}$$

$$\frac{\partial}{\partial b}\frac{\mathrm{d}t}{\mathrm{d}s} = \frac{e^{\alpha-(\gamma+\rho)/2}}{h^{3/2}}\frac{b}{e^{-2\rho}\bar{r}^2\sin^2\theta}; \text{ and} \tag{2.100}$$

$$\frac{\mathrm{d}\phi}{\mathrm{d}s} = -\frac{1}{2}\frac{e^{\alpha-(\gamma+\rho)/2}}{h^{1/2}}\frac{\mathrm{d}h}{\mathrm{d}b}, \tag{2.101}$$

$$\frac{\partial}{\partial b}\frac{\mathrm{d}\phi}{\mathrm{d}s} = \frac{e^{\alpha-(\gamma+\rho)/2}}{h^{3/2}}\frac{1}{e^{-2\rho}\bar{r}^2\sin^2\theta}. \tag{2.102}$$

So,

$$\frac{\partial}{\partial b}\frac{\mathrm{d}t}{\mathrm{d}s} = b\frac{\partial}{\partial b}\frac{\mathrm{d}\phi}{\mathrm{d}s}. \tag{2.103}$$

Regarding T and $\Delta\phi$ as functions of s, we have

$$T = \int_0^{s_f} \mathrm{d}s \frac{\mathrm{d}t}{\mathrm{d}s} \tag{2.104}$$

$$\Delta\phi = \int_0^{s_f} \mathrm{d}s \frac{\mathrm{d}\phi}{\mathrm{d}s}. \tag{2.105}$$

Equations 2.104 and 2.105 are of the form of exact line integrals. Thus, if the impact parameter b is held fixed, the values of these two integrals depends only on the endpoints $(\bar{r}_i, \theta_i)$ and $(\bar{r}_f, \theta_f)$. If the endpoints of the geodesic are kept fixed, then we can obtain new integral expressions for the derivative of the arrival time and azimuthal deflection with respect to b, by interchanging the order of integration and differentiation as follows:

$$\frac{\mathrm{d}T}{\mathrm{d}\phi_e} = \frac{\partial T/\partial b}{-\partial(\Delta\phi)/\partial b} = -\frac{\frac{\partial}{\partial b}\int_0^{s_f}\mathrm{d}s(\mathrm{d}t/\mathrm{d}s)}{\frac{\partial}{\partial b}\int_0^{s_f}\mathrm{d}s(\mathrm{d}\phi/\mathrm{d}s)}$$

$$= -\frac{\int_0^{s_f}\mathrm{d}s\frac{\partial}{\partial b}(\mathrm{d}t/\mathrm{d}s)}{\int_0^{s_f}\mathrm{d}s\frac{\partial}{\partial b}(\mathrm{d}\phi/\mathrm{d}s)} \tag{2.106}$$

$$= -\frac{b\int_0^{s_f}\mathrm{d}s\frac{\partial}{\partial b}(\mathrm{d}\phi/\mathrm{d}s)}{\int_0^{s_f}\mathrm{d}s\frac{\partial}{\partial b}(\mathrm{d}\phi/\mathrm{d}s)} \tag{2.107}$$

$$= -b. \tag{2.108}$$

Therefore, according to this argument, the factor which accounts for the motion of the emitting region satisfies (however, see below for a caveat)

$$1 + \Omega_\star \mathrm{d}T/\mathrm{d}\phi = 1 - \Omega_\star b. \tag{2.109}$$

In this calculation, it is claimed that the order of differentiation with respect to b and the path integral in the $(\bar{r}, \theta)$ plane can be interchanged because we were holding the endpoints of the curve fixed, and the integrals were of the form of exact line integrals. One possible objection to this argument is that we have neglected terms in the derivative related to how the path length changes with small changes in b. This is a technical point that we wish to study further. However, note that in Section 3.5.4 we show the result of a numerical experiment which shows that Equation 2.109 holds to reasonable accuracy (typically within a few parts in 10^3) in our code when the left-hand side is calculated by finite differencing the arrival times. So if additional terms are required to make Equation 2.109 formally correct, our experiments have indicated that any such additional terms would be small, i.e., that Equation 2.109 seems to hold in the neutron star spacetimes we considered. As discussed in Chapter 3, our pulse profile calculations calculated the left-hand side of Equation 2.109 numerically using the integrated arrival times. Making use of this formula was left to future work.

2.5 Calculating the light curve in the Schwarzschild metric

In this section we develop a method for calculating the light curve when the exterior spacetime is taken to be Schwarzschild, and the star is taken to be spherical. The additional symmetry allows us to obtain a formula for the light curve which is easily computed and doesn't rely on the methodology envisaged for calculating the light curves in the more general case. Thus, it's a method to check independently the implementation of the more general method that we have laid the foundations for in this chapter. This check is carried out in Section 3.5.2. The formalism for calculating the light curves for emission from the bright spots on the surface of slowly-rotating neutron stars was developed by Pechenick *et al.* (1983), and employs the Schwarzschild metric to describe gravitational effects. The development of this section draws on Leahy (2003b) and Poutanen and Gierliński (2003), but additional details are filled in and the effect due to the motion of the emitting region is treated differently.

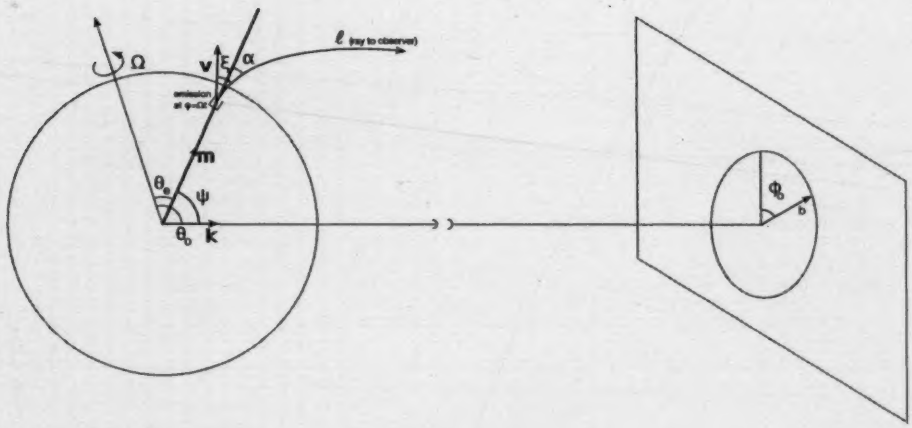

Figure 2.4: Geometry for calculating projection of emitting region onto observer's sky in Schwarzschild metric

We are considering the flux from a star of radius R and mass M, and the geometry of the situation is depicted in Figure 2.4. A useful way to describe the geometry is to define a three-vector $\mathbf{k}$ which points from the origin towards the observer inclined at an angle θ_o to the spin axis of the star, and a second three-vector $\mathbf{m}$ which points at the emitting region inclined at an angle θ_e to the spin axis, and located at azimuthal angle (i.e., rotational phase) $\phi = \Omega_\star t_e$. In a right-handed system of rectilinear coordinates where the x-axis is located at $\phi = 0$ in the equatorial plane *of the star*, and the z-axis points along the spin axis of the star, the rectilinear components of these vectors can be taken to be

$$\mathbf{k} = (\sin\theta_o, 0, \cos\theta_o), \text{ and,} \tag{2.110}$$

$$\mathbf{m} = (\cos\phi\sin\theta_e, \sin\phi\sin\theta_e, \cos\theta_e). \tag{2.111}$$

In the coordinate plane containing the origin, emission region, and observer, observed photons are deflected through an angle ψ, with

$$\cos\psi = \mathbf{k}\cdot\mathbf{m} = \cos\theta_o\cos\theta_e + \sin\theta_o\sin\theta_e\cos\phi. \tag{2.112}$$

The Schwarzschild spacetime is spherically symmetric, and the metric is given by

$$ds^2 = -(1-2M/r)dt^2 + \frac{dr^2}{1-2M/r} + r^2\left(d\tilde{\theta}^2 + \sin^2\tilde{\theta}d\psi^2\right). \tag{2.113}$$

The spherical symmetry allows us to consider all photon orbits as orbits in a coordinate equatorial plane ($\tilde{\theta} = \pi/2$) which in general does not coincide with the star's equatorial plane. The orbits of photons in this plane are described by the equations of motion

$$\frac{dt}{d\lambda} = \frac{1}{1-2M/r} \tag{2.114}$$

$$\frac{d\psi}{d\lambda} = \frac{b}{r^2} \tag{2.115}$$

$$\frac{dr}{d\lambda} = \left[1-(1-2M/r)\frac{b^2}{r^2}\right]^{1/2}, \tag{2.116}$$

where the impact parameter b is a constant of the motion, with $|b| \leq R/(1-2M/R)^{1/2}$ for outgoing rays. The angular deflection $\psi(b)$ between the star's surface at $r = R$ and a distant observer at $r = r_f$ can be calculated by dividing Equation 2.115 by Equation 2.116 and integrating:

$$\psi(b) = \int_R^{r_f} dr \frac{1}{r\left[r^2/b^2 - (1-2M/r)\right]^{1/2}}. \tag{2.117}$$

The lapse of coordinate time between two radial coordinates joined by a photon orbit can be found in a similar way, but because this quantity will diverge in the limit $r_f \to \infty$, it is more convenient to calculate the difference between this time and the time a radial ($b = 0$) ray would take:

$$T(b) = \int_R^{r_f} dr \frac{1}{1-2M/r}\left[\frac{1}{(1-(1-2M/r)b^2/r^2)^{1/2}} - 1\right]. \tag{2.118}$$

Measured in the observer's frame, the angle α formed by the initial direction of the outgoing ray with the (radial) normal to the star's surface can be calculated using the "cos angle" relation (see Equation 2.67) where the observer in this situation has $u^a = t^a/(-g_{tt})^{1/2}$. If ℓ^a is the four-momentum of the emitted photon, one obtains that

$$\cos\alpha = \ell^r, \tag{2.119}$$

which, using Equation 2.116, is

$$\sin\alpha = (1 - 2M/R)^{1/2} b/R. \tag{2.120}$$

We also would like to calculate the angle ξ formed by the light ray and the velocity vector at the surface of the star. One way to do this is by explicitly setting out a rotation mapping (θ, ϕ) "star" coordinates to the $(\tilde{\theta}, \psi)$ "propagation" coordinates, however this is not the most straightforward approach.[4] Instead, it is more convenient to make use of an orthonormal basis for the photon propagation plane to complete the calculation. Take $\mathbf{m}$ and $\mathbf{k}_\perp$ to be the basis vectors, with

$$\mathbf{k}_\perp \equiv \frac{\mathbf{k} - (\mathbf{m}\cdot\mathbf{k})\mathbf{m}}{[1 - (\mathbf{m}\cdot\mathbf{k})^2]^{1/2}} = \frac{\mathbf{k} - \cos\psi\mathbf{m}}{\sin\psi}. \tag{2.121}$$

If $\mathbf{l}_i$ is a unit vector pointing in the initial direction of the photon propagation, then in terms of the given basis vectors, it has components

$$\begin{aligned} \mathbf{l}_i &= (\mathbf{l}_i\cdot\mathbf{m})\mathbf{m} + (\mathbf{l}_i\cdot\mathbf{k}_\perp)\mathbf{k}_\perp \\ &= \cos\alpha\mathbf{m} + \frac{1}{\sin^2\psi}\left[\cos(\psi-\alpha) - \cos\psi\cos\alpha\right](\mathbf{k} - \cos\psi\mathbf{m}) \\ &= \frac{\sin(\psi-\alpha)}{\sin\psi}\mathbf{m} + \frac{\sin\alpha}{\sin\psi}\mathbf{k}. \end{aligned} \tag{2.122}$$

Considering the rectlilinear components of $\mathbf{k}$ and $\mathbf{m}$ in Equations 2.110 and 2.111, and that a unit vector pointing in the direction the star's motion has components in this system given by

$$\mathbf{v} = (-\sin\phi, \cos\phi, 0), \tag{2.123}$$

then we have that ξ is related to α, θ_o, ϕ, and ψ by:

$$\cos\xi = \mathbf{l}_i\cdot\mathbf{v} = -\frac{\sin\alpha\sin\theta_o\sin\phi}{\sin\psi}. \tag{2.124}$$

To calculate the projection of the emission region on the observer's sky, also depicted in Figure 2.4, consider that rays reaching the observer will land on the image plane at radial coordinate b and azimuthal angle ϕ_o, which is given by

$$\cos\phi_o = \frac{\mathbf{n}_{\phi_o=0}\cdot(\mathbf{k}\times\mathbf{m})}{|\mathbf{k}\times\mathbf{m}|}, \tag{2.125}$$

[4]The explicit rotation is considered briefly in Section 4.5.1, where in that section we require the description of the ray in both systems of coordinates.

where $\mathbf{n}_{\phi_o=0}$ is an arbitary unit vector perpendicular to $\mathbf{k}$ which defines the direction on the image plane corresponding to $\phi_o = 0$. If we take $\mathbf{n}_{\phi_o=0} = (0, 1, 0)$, then

$$\cos\phi_o = \frac{\cos\theta_o \sin\theta_e \cos\phi - \sin\theta_o \cos\theta_e}{\left[\sin^2\theta_e \sin^2\phi + (\cos\theta_o \sin\theta_e \cos\phi - \sin\theta_o \cos\theta_e)^2\right]^{1/2}}. \tag{2.126}$$

The element of flux received by the observer is

$$\mathrm{d}F = I_o \mathrm{d}S_o / D^2, \tag{2.127}$$

where I_o is the intensity of the observed radiation, D the distance separating the source and observer, and the element of area $\mathrm{d}S_o$ on the image plane, which is

$$\mathrm{d}S_o = b\,\mathrm{d}b\,\mathrm{d}\phi_o. \tag{2.128}$$

Ultimately we want to be able to express the integral for flux in terms of the coordinates θ_e, ϕ on the star's surface, which will require the Jacobian

$$\begin{aligned} J &= \frac{\partial b}{\partial \theta_e}\frac{\partial \phi_o}{\partial \phi} - \frac{\partial b}{\partial \phi}\frac{\partial \phi_o}{\partial \theta_e} \\ &= \frac{1}{\mathrm{d}\psi/\mathrm{d}b \sin\psi \sin\phi_o}\left(\frac{\partial(\cos\psi)}{\partial\theta_e}\frac{\partial(\cos\phi_o)}{\partial\phi} - \frac{\partial(\cos\psi)}{\partial\phi}\frac{\partial(\cos\phi_o)}{\partial\theta_e}\right). \end{aligned} \tag{2.129}$$

By differentiation of Equation 2.112 for $\cos\psi$ and Equation 2.126 for $\cos\phi_o$, the Jacobian in Equation 2.129 is seen (after a very tedious exercise) to be

$$J = \frac{1}{\mathrm{d}\psi/\mathrm{d}b}\frac{\sin\theta_e}{\sin\psi}, \tag{2.130}$$

so the integral for the observed flux from a *stationary* emitting region on the surface of the star is

$$F_{\nu_o} = \frac{1}{D^2}\int \frac{I_{\nu_e}}{(1+z)^3} b \frac{1}{\mathrm{d}\psi/\mathrm{d}b}\frac{\sin\theta_e}{\sin\psi}\mathrm{d}\theta_e \mathrm{d}\phi. \tag{2.131}$$

To bring in the effect of rotation on the observed light curve, we know that for a bright spot of width $\Delta\phi'_e$ in the emission frame, only a region of width

$$\frac{\Delta\phi'_e/\Gamma}{1 + \Omega_\star \mathrm{d}T/\mathrm{d}\phi}$$

is visible to the observer at the instant $t = t_o = \Omega_\star\phi + T(b)$. The denominator of this term is

$$1 + \Omega_\star\frac{\mathrm{d}T}{\mathrm{d}\phi} = 1 + \Omega_\star\frac{\mathrm{d}\psi}{\mathrm{d}\phi}\frac{1}{\mathrm{d}\psi/\mathrm{d}b}\frac{\mathrm{d}T}{\mathrm{d}b}, \tag{2.132}$$

where

$$\frac{\mathrm{d}\psi}{\mathrm{d}\phi} = \frac{\sin i \sin\theta_e \sin\phi}{\sin\psi} \tag{2.133}$$

$$\frac{\mathrm{d}\psi}{\mathrm{d}b} = \int_R^{r_f} \mathrm{d}r \left[\frac{1}{r^2\left[1-(1-2M/r)b^2/r^2\right]^{1/2}} + \frac{b^2(1-2M/r)}{r^4\left[1-(1-2M/r)b^2/r^2\right]^{3/2}} \right]$$

$$= \int_R^{r_f} \mathrm{d}r \frac{1}{r^2\left[1-(1-2M/r)b^2/r^2\right]^{3/2}} \tag{2.134}$$

$$\frac{\mathrm{d}T}{\mathrm{d}b} = \int_R^{r_f} \mathrm{d}r \frac{b}{r^2\left[1-(1-2M/r)b^2/r^2\right]^{3/2}} = b\frac{\mathrm{d}\psi}{\mathrm{d}b}. \tag{2.135}$$

So for a small emission region of size $\Delta\phi'_e \times \Delta\theta_e$, the quantity to be evaluated is

$$F_{\nu_o}(t_o) = \frac{1}{D^2}\frac{I_{\nu_e}}{(1+z)^3} b \frac{1}{\mathrm{d}\psi/\mathrm{d}b}\frac{\sin\theta_e}{\sin\psi}(\Delta\theta_e)\frac{(\Delta\phi'_e)/\Gamma}{1+\Omega_\star\frac{\mathrm{d}\psi}{\mathrm{d}\phi}\frac{1}{\mathrm{d}\psi/\mathrm{d}b}\frac{\mathrm{d}T}{\mathrm{d}b}} \tag{2.136}$$

$$= \frac{1}{D^2}\frac{I_{\nu_e}}{(1+z)^3} b \frac{1}{\mathrm{d}\psi/\mathrm{d}b}\frac{\sin\theta_e}{\sin\psi}(\Delta\theta_e)\frac{(\Delta\phi'_e)/\Gamma}{1+\Omega_\star b\frac{\mathrm{d}\psi}{\mathrm{d}\phi}}. \tag{2.137}$$

The evaluation is accomplished in the following manner:

1. Pick a rotation phase $\phi = \Omega_\star t_e$. Calculate the bending angle ψ via Equation 2.112.

2. Solve for the impact parameter b which yields ψ via the integral given in Equation 2.117. This can be done either numerically or via a polynomial approximation to the integral such as the one given by Beloborodov (2002).

3. Calculate the arrival time $t_o = t_e + T(b)$ by evaluating the integral for T in Equation 2.118.

4. Calculate the derivatives appearing in Equation 2.137 by using the Equation 2.133 for $\mathrm{d}\psi/\mathrm{d}\phi$, and Equation 2.134 for $\mathrm{d}\psi/\mathrm{d}b$.

5. Calculate $\Gamma = (1-v^2)^{1/2}$, using $v = R\Omega_\star \sin\theta_e/(1-2M/R)^{1/2}$ at the star's surface.

6. Calculate the redshift $(1+z) = (1-2M/R)^{-1/2}/\delta$, where δ is defined in Equation 2.92, and $\cos\xi$ is given in Equation 2.124.

2.5.1 The Doppler factor and times-of-flight in Poutanen and Gierliński (2003)

Poutanen and Gierliński (2003) derive the integral to be evaluated for the light curve in a slightly different manner. They start off with an element of area $\mathrm{d}S'$ in the emission frame, and an element $\mathrm{d}S$ in the observer's frame. Observing that the zenith angle of emitted rays between the emission and observation frames transforms as $\cos\alpha' = \delta\cos\alpha$, and that Terrell (1959) says that observed and emitted areas transform as $\delta\mathrm{d}S' = \mathrm{d}S$, they see that the projected area $\mathrm{d}S'\cos\alpha' = \mathrm{d}S\cos\alpha$ is an invariant, and they proceed.

It's difficult to see whether the result $\delta\mathrm{d}S' = \mathrm{d}S$ holds for our situation, as this is a result inspired by special relativity. By comparison with the above calculations, but relabelling b from Section 2.5 as b', it amounts to a claim that

$$\delta \stackrel{?}{=} \frac{1/\Gamma}{1+\Omega_\star b'\frac{\mathrm{d}\psi}{\mathrm{d}\phi}}, \tag{2.138}$$

which is the same as saying

$$1 - v\cos\xi \stackrel{?}{=} 1 + \Omega_\star b'\frac{\mathrm{d}\psi}{\mathrm{d}\phi}. \tag{2.139}$$

To assess the sense in which Equation 2.139 holds, let us again consider the situation with the general metric. First, the b' on the right-hand side is related to the conserved angular momentum ℓ_ψ in the propagation plane. From Equations 2.132 and 2.135, we know that the right-hand side satisfies

$$1 + \Omega_\star b'\frac{\mathrm{d}\psi}{\mathrm{d}\phi} = 1 + \Omega_\star\frac{\mathrm{d}T}{\mathrm{d}\phi}. \tag{2.140}$$

In terms of the axisymmetric coordinates for the general case, b is defined via the angular momentum ℓ_ϕ, and by comparing Equation 2.140 with Equation 2.109, we conclude that

$$1 + \Omega_\star b'\frac{\mathrm{d}\psi}{\mathrm{d}\phi} = 1 - \Omega_\star b, \tag{2.141}$$

and the claim in Equation 2.139 is now

$$1 - v\cos\xi \stackrel{?}{=} 1 - \Omega_\star b. \tag{2.142}$$

To see the conditions under which Equation 2.142 is true, we now express the left-hand side in terms of quantities in the general axisymmetric metric. Note

that we are doing these calculations for the observer $u^a = t^a/W$ and not the zero angular momentum observer. The angle ξ formed between the fluid velocity and the emitted ray in the observer's frame can be calculated via the formula

$$\cos\xi = -\frac{(W/V)(1-\Omega_\star b) + (g_{tt}+\Omega_\star g_{t\phi})/(WV)}{[-1+((g_{tt}+\Omega_\star g_{t\phi})/(WV))^2]^{1/2}}, \tag{2.143}$$

and the velocity measured at the surface in the observer's frame is

$$v = \sqrt{1 - \frac{W^2V^2}{(g_{tt}+\Omega_\star g_{t\phi})^2}}. \tag{2.144}$$

Then in the general spacetime, the left-hand side can be expressed as

$$\begin{aligned} 1 - v\cos\xi &= 1 + \frac{WV}{|g_{tt}+\Omega_\star g_{t\phi}|}\left[\frac{W}{V}(1-\Omega_\star b) + \frac{g_{tt}+\Omega_\star g_{t\phi}}{WV}\right] \\ &= \frac{W^2}{|g_{tt}+\Omega_\star g_{t\phi}|}(1-\Omega_\star b) \\ &= \frac{1}{1+(\Omega_\star g_{t\phi}/g_{tt})}(1-\Omega_\star b). \end{aligned} \tag{2.145}$$

When the exterior spacetime is taken to be Schwarzschild, the metric component $g_{t\phi} = 0$ (i.e., there is no frame dragging), and so Equation 2.142 holds exactly. In the general case, however, $g_{t\phi} \neq 0$ and the Doppler factor is not equivalent (and ought not to be used in place of) the factor $1 - \Omega_\star b = 1 + \Omega_\star \mathrm{d}T/\mathrm{d}\phi$, which is brought in to account for the motion of the emitting region.

The calculation by Poutanen and Gierliński (2003) is correct in the sense that they are calculating an integral which is exactly correct in the case they consider (i.e., when the exterior spacetime is Schwarzschild and the star is taken to be spherical), but they omit the step of calculating the arrival time $t_o = t_e + T(b)$ by evaluating the integral for T in Equation 2.118 at each step. Instead they adopt the approximation that $t_o = t_e + \text{const}$ for the construction of their light curves, which results in a distortion of the curves they obtained for rapid rotation. Put another way, they account for the fact that the arrival times are changing (because the emission region is moving) for the purpose of calculating the flux, but don't account for this in assigning the integrated flux to some observed time. This distorts the pulse shape, and has implications for data analysis. This is discussed further in Section 4.3.

Chapter 3

Numerical procedure

3.1 Introduction

The main objective of this work is, first, to set out a general method by which the observed flux from a bright spot on the surface of a rapidly-rotating neutron star can be calculated without invoking a special choice of the exterior metric, and including the effects of the varying times-of-flight of photons and the motion of the emitting region. The analytical part of this was set out in Chapter 2, but the method that is envisioned requires numerical methods to evaluate the integrals that result—at least because, in general, the metric components are only known numerically. A second objective is to determine the degree to which an accurate calculation with a precise metric, stellar oblateness, time-of-flight, and motion effects included, differs from calculations that make approximations to one or more of these elements which our method is designed to include. In order to accomplish this, it was necessary to implement a code that was flexible enough that it would be possible to carry through the precise calculation, but also several variations on it. In this chapter, we touch on the various techniques we have used in this implementation of this computer code, and provide a look at some of the code verification which was performed.

The computer code for this project was implemented in the C++ programming language (Stroustrup (1997); also see Eckel (2000) for an excellent guide to the language). In its current form, approximately 13.1×10^3 lines of source code were developed for this work including declarations, comments, and a small amount of superceded code, but not including blank lines. We also make use of an external library (Gammel, 2005) for interpolation methods, and have customised a version of the RNS code (Stergioulas and Friedman, 1995) to produce files containing the

metric components, their derivatives, stellar oblateness, and other stellar parameters for a stellar model specified by a choice of equation of state (EOS), mass, and spin frequency. Details about RNS and the modifications are given in Section 2.2.

Developing the code in C++ was a natural choice, because it allows the software to be written in a fashion where logical concepts (e.g., a metric, of basic type `Metric`) are decoupled from the implementation details (e.g., the code to deal with a numerically-specified metric from RNS output in the class `RNSMetric`, or perhaps an analytically specified metric, as in the class `KerrMetric`). In this example, `RNSMetric` is called a subclass of the class `Metric`. The exact specification of metric type can be made at runtime using command-line arguments, but aside from the initial creation of the metric data structure, the remainder of the code need only ever be written to deal with the generic base type `Metric`, rather than dealing with all possible subclasses of `Metric` that might be encountered. In other words, one does not need to write complicated branching routines, or multiple versions of functions adapted for every conceivable subclass of the base class `Metric`, and instead one just deals with a common interface that all such subclasses implement. The correct mapping, or "binding", between a function call somewhere in the code to a method that all instances of classes deriving from `Metric` must implement (e.g., all such instances must provide an implementation of the function `Metric::rho(r,theta)`), to the required implementation of that function (e.g., a call to the code for `RNSMetric::rho(r, theta)`), is determined automatically at runtime with no additional effort by the programmer. This is one of the basic features of object-oriented programming languages. This feature of C++, and others which are not present in procedural languages like C and FORTRAN, are used to solve several problems in the design of the code.

3.1.1 Details of metric and stellar surface descriptions

In particular, given an EOS, mass M, and frequency $\Omega_\star$, we investigate the following five situations, which each represent a subclass of `Metric`:

Exact Using the exact metric, and surface location $\bar{r}_s(\theta)$ as output by the customised RNS code.

Oblate Kerr (OK) Using the Kerr metric as given in Section 2.2.1 with $a = J/M$, where J is obtained from the RNS calculation, and the stellar surface located at the same $\bar{r}_s(\theta)$ as in the Exact case.

"Spherical" Kerr (SK) As above, but the stellar surface is located at constant $\bar{r} = \bar{r}_s(\pi/2)$ at all θ.

Oblate Schwarzschild (OS) As for OK, but setting $a = 0$.

Spherical Schwarzschild (SS) Where the Exact case is used to calculate the areal (Schwarzschild) radius on the equator, $R = \exp[(\gamma - \rho)/2]\bar{r}_s(\pi/2)$, and the surface is located at coordinate $\bar{r}$ such that the areal radius has value R (using the Schwarzschild metric) at all angles.

It should be noted that with this definition, the OS and SS cases do not agree on the value of $\bar{r}$ or R on the equator due to the slight difference in their definition. While it is possible to redefine the OS or SS approximation so that they are consistent in this fashion, the definitions above represent perhaps the most straightforward means by which a person with access to a structure code such as RNS and a ray tracing code for the Schwarzschild or Kerr spacetimes might attempt to approximate the situation.

3.2 Integration of rays

Integration of a single null ray proceeds by setting the initial coordinates $\bar{r}_i$ and θ_i, selecting an allowed value of b according to the constraint at Equation 2.41, and initial values of $\dot{\theta}_i$ and $\dot{\bar{r}}_i$ which are constrained by the geometry of the stellar surface. With the initial conditions in hand, the ordinary differential equations 2.33, 2.34, 2.37, and 2.38 for the path followed by the ray can be integrated numerically. Since Equations 2.37 and 2.38 are second order equations, we add two equations to the family to reduce the set of ODEs to a set of six first order equations for $\{t(\lambda), \phi(\lambda), \theta(\lambda), \dot{\theta}(\lambda), \bar{r}(\lambda), \dot{\bar{r}}(\lambda)\}$.

To accomplish this integration, we use a customised version of a standard adaptive 4th-5th order Runge-Kutta routine (Press *et al.*, 1988). The particular customisations were to allow for more flexible error controls than the routine given in Press *et al.* (1988), as well as an adaptation to accomodate the peculiarities of the coordinate system we are using. For example, in the (ϕ, θ) angular coordinates that we use, it is possible for a numerical integrator to get into difficulty by stepping to $\theta < 0$; additional care must be taken so that such steps are corrected for appropriately by changing the sign of θ and taking ϕ to $\phi + \pi$ without causing problems with the adaptive step control. Additionally, care must be taken that all integrations end at the same value of $\bar{r} = \bar{r}_f$.

For some applications, all that we require is an accurate determination of θ_f and $\Delta\phi$ given a set of initial conditions. In this situation, we are able to run the integration in a faster mode since it is possible to extrapolate the final values of θ_f and $\Delta\phi$ accurately after most of the integration has run, without doing the time-consuming integration of the final values of $\dot{\theta}$ and $\dot{\bar{r}}$ at $\bar{r} = \bar{r}_f$. This extrapolation is accomplished using the `polint` routine in Press *et al.* (1988). The full integration to $\bar{r} = \bar{r}_f$ runs approximately 8 times slower than this fast version, but the cost of using the fast integrator is that the final values of $\dot{\theta}$ and $\dot{\bar{r}}$ are not useable; the integrals obtained in this manner are useful for making the interpolation routine described in Section 3.3 reasonably fast since it contains an iteration which requires the repeated integration of geodesics.

3.2.1 Calculating the time-of-flight

Another modification of the numerical ODE integrator allows us to get accurate times-of-flight of the rays. As in the case of the Schwarzschild formulation of the problem in Section 2.5, it is more convenient to calculate the time-of-flight of a photon relative to some other ray, since the relative time-of-flight is much smaller than the values of t_f output by the straightforward integration. To accomplish this calculation, we use the Runge-Kutta integrator to integrate a set of 13 ODEs: 6 of which are for the ray being integrated, 6 of which are for the integral of the ray chosen as having zero (relative) time-of-flight, and a final equation to accumulate the relative time-of-flight

$$\frac{\mathrm{dT}}{\mathrm{d}\lambda} = \dot{t}_{\mathrm{ray}}(\lambda) - \dot{t}_{\mathrm{zero}}(\lambda). \tag{3.1}$$

Of course care must be taken to account for the different parameter lengths of the "zero" ray and the ray being integrated. Since we envision finite-differencing the time-of-flight arrived at in this way to get a derivative, the error in this quantity must be small relative to the change in the time-of-flight over the size of the rotational phase bins.

This integration can run roughly 20 times slower than the standard integration described above, and 160 times slower than the fast version described above. For efficiency, this method is only used to obtain the time-of-flight of particular rays; the fastest method is used to examine the variation of $\Delta\phi$ and θ_f over the space of allowed initial conditions.

3.3 Interpolation of rays

The straightfoward integration of geodesics takes initial conditions θ_i, $\bar{r}(\theta_i)$, b, $\dot{\theta}_i$, and $\mathrm{sgn}(\dot{\bar{r}}_i)$, and yields the azimuthal deflection $\Delta\phi$ and final value θ_f at the endpoint of the integration. However, determining the rays extending from a given position on the star to the observer requires solving a slightly different problem: we need a method by which to determine b, $\dot{\theta}_i$, and $\mathrm{sgn}(\dot{\bar{r}}_i)$ if we know θ_i, $\bar{r}(\theta_i)$, $\Delta\phi$ and θ_f. To accomplish this, we fix θ_i and $\bar{r}_i$, and integrate a number of rays over the entire range of the remaining initial conditions b, $\dot{\theta}_i$, $\mathrm{sgn}(\dot{\bar{r}}_i)$. Finally, we use interpolation to construct the functions $b(\Delta\phi, \theta_f)$, $\dot{\theta}_i(\Delta\phi, \theta_f)$, and $\dot{\bar{r}}_i(\Delta\phi, \theta_f)$ in order to determine estimates of the initial conditions which will yield the particular rays we seek. Once an estimate of the required initial conditions is obtained in this manner, the forward integration of the interpolated initial conditions can be carried out as described above, and the precision of the interpolation checked. If necessary, subsequent interpolations can be carried out so that ultimately we arrive at a set of values b, $\dot{\theta}_i$, and $\mathrm{sgn}(\dot{\bar{r}}_i)$ which, after integration, yield $\Delta\phi$ and θ_f to a required accuracy. Once a final set of initial conditions is arrived at, the ray is re-integrated using the time-of-flight method described above.

The choice of methods by which the interpolating functions can be constructed is limited by the fact that the "data" to be used for the interpolations do not fall on a regularly-spaced grid in $\Delta\phi$ and θ_f. This rules out the use of standard methods such as bicubic spline interpolation (Press *et al.*, 1988). An obvious choice for the interpolation method is a bilinear approach: this would proceed roughly by taking the three closest points close to the desired $\Delta\phi, \theta_f$, and regarding the quantities to be interpolated, denoted $f(\Delta\phi, \theta_f)$, as being described by the unique plane which passes through the three data. In practise, this method required too large a collection of interpolating data for the iteration described above to converge reliably: if the ray corresponding to the interpolated initial conditions is not closer to the desired point than the three vertices used to construct the interpolating function, then this method cannot be used as an iteration for successively improved rays. It was found that Shepard's method (Shepard, 1968) for interpolation performed acceptably well in that it did not require too much data for the envisaged interpolation to converge quickly; we make use of a publicly-available implementation of a modified Shepard's method which is distributed with the Matpack C++ Numerics and Graphics Library (Gammel, 2005; Renka, 1988). The details of this interpolation algorithm are set out below in Section 3.3.1.

3.3.1 Shepard's Interpolation of Scattered Data[1]

Shepard's method uses a system of weighted averages to produce a once continuously differentiable interpolating function which passes though the interpolating data; the method also attempts to account for "screening" of far away data by closer data in the same direction, and to produce an interpolating function with reasonable partial derivatives. Following Shepard (1968), we will describe how the method can accomplish these objectives, although the specific implementation by Renka (1988) has been improved in certain respects. Starting with N data values z_i for points $D_i = (x_i, y_i)$, we wish to interpolate the value of a function $f(x, y)$ described by the data at the point $P = (x, y)$. If $d(P, D_i) \equiv d_i$ is the Euclidean distance between P and D_i, then the basic idea of weighted average interpolation is to compute the approximation

$$f_1(x,y) = \begin{cases} \frac{\sum_i d_i^{-u} z_i}{\sum_i d_i^{-u}} & \text{if } d_i \neq 0 \text{ for every } i \\ = z_i & \text{if } d_i = 0 \text{ for some } i. \end{cases} \tag{3.2}$$

The requirement that the interpolating function f is differentiable requires $u \geq 1$. This particular prescription has the property that the x and y partial derivatives of the interpolation function approach 0 at the data, and it is desireable to find a method by which takes into account the "slope" of the data so that reasonable partial derivatives are obtained. Empirically, Shepard (1968) found that $u > 2$ leads to situations where the interpolating function is quite flat near the data and has steep transition zones between data, whereas $u = 2$ tended to work better for general purposes.

To make the calculation more efficient, it is reasonable to compute the above approximation by summing over only those points in some r-neighbourhood of P, $C_P = \{D_i | d_i \leq r\}$, with r chosen so that a sufficient number of data are included, but small enough for the computation to be efficient. Futhermore, one can reasonably generalise the weights $1/d_i$ to be weaker for the most distant points.

[1]The development of this section follows almost identically the exposition originally given by Shepard (1968); the development is repeated here since it's not a difficult algorithm, and significant use is made of it. Furthermore, it is not discussed in standard numerical methods texts like Press *et al.* (1988).

Shepard (1968) proposes the weights $s_i = s(d_i)$ given by

$$s(d) = \begin{cases} \frac{1}{d} & \text{if } 0 < d \leq r/3 \\ \frac{27}{4r}\left(\frac{d}{r} - 1\right)^2 & \text{if } \frac{r}{3} < d \leq r \\ 0 & \text{if } r < d. \end{cases} \tag{3.3}$$

These weights have the required continuity at $d = r/3$, and have the property that points outside of C_P are not included in the weighted average. The interpolating function is taken to be

$$f_2(x, y) = \begin{cases} \frac{\sum_i s_i^2 z_i}{\sum_i s_i^2} & \text{if } d_i \neq 0 \text{ for every } i \\ = z_i & \text{if } d_i = 0 \text{ for some } i. \end{cases} \tag{3.4}$$

To incorporate the effect of "screening" of more distant data by closer data in the same direction, the weights are further modified by incorporating a directional term,

$$t_i = \frac{\sum_j s_j(1 - \cos(D_i P D_j))}{\sum_j s_j}, \tag{3.5}$$

where

$$\cos(D_i P D_j) = \frac{(x - x_i)(x - x_j) + (y - y_i)(y - y_j)}{d_i d_j}. \tag{3.6}$$

The factor t_i tends to be close to 0 when D_i lies generally in the same direction as the other data away from P, and close to 2 when D_i lies opposite the other data from P. Shepard (1968) defines new weighting functions $w_i = (s_i)^2(1 + t_i)$ which has the effect of increasing the influence of unscreened data and decreasing the influence of screened data. The interpolating function is given by

$$f_3(x, y) = \begin{cases} \frac{\sum_i w_i z_i}{\sum_i w_i} & \text{if } d_i \neq 0 \text{ for every } i \\ = z_i & \text{if } d_i = 0 \text{ for some } i. \end{cases} \tag{3.7}$$

The remaining issue that Shepard (1968) deals with is an adjustment to account for the "slope" of the data, as the preceding interpolating functions all have the property that at every D_i, $\partial f/\partial x = \partial f/\partial y = 0$. This is accomplished by setting out a weighted average corresponding to an approximation of the partial derivatives of the data; summing over the data in $C_P^i \equiv C_P \setminus D_i$,

$$A_i = \frac{\sum_{D_j \in C_P^i} w_j \frac{(z_j - z_i)(x_j - x_i)}{d(D_i, D_j)^2}}{\sum_{D_j \in C_P^i} w_j} \tag{3.8}$$

$$B_i = \frac{\sum_{D_j \in C_P^i} w_j \frac{(z_j - z_i)(y_j - y_i)}{d(D_i, D_j)^2}}{\sum_{D_j \in C_P^i} w_j}. \tag{3.9}$$

Clearly A_i and B_i are respectively estimates of the x and y partial derivatives of the data at D_i. To see this, consider the general situation of a function $F(x, y)$ and a second function $G(\lambda)$ which is once continuously differentiable, with

$$\lambda^2 \equiv (x - x_i)^2 + (y - y_i)^2, \tag{3.10}$$

G satisfying $G(0) = F(x_i, y_i) = z_i$ and $G(d(D_i, D_j)) = F(x_j, y_j) = z_j$. Then if $dF = dG$, we have

$$\frac{\partial F}{\partial x}\mathrm{d}x + \frac{\partial F}{\partial y}\mathrm{d}y = \frac{1}{\lambda}\frac{\mathrm{d}G}{\mathrm{d}\lambda}\left[(x - x_i)\mathrm{d}x + (y - y_i)\mathrm{d}y\right] \tag{3.11}$$

Approximation of $\partial F/\partial x$ at D_i is obtained by approximating $\mathrm{d}G/\mathrm{d}\lambda \approx \Delta G/\lambda$, where $\Delta G = G(d(D_i, D_j)) - G(0)$ and $\lambda = d(D_i, D_j)$, so that

$$\frac{\partial F}{\partial x} \approx \frac{(\Delta G)(x_j - x_i)}{d(D_i, D_j)^2}. \tag{3.12}$$

The quantity A is just the weighted average of these approximations over pairs of data. Similarly, the y partial derivative is approximated by B.

These slope terms should be introduced in such a manner that they affect the interpolated values close to the data, but have little effect far from data. Shepard (1968) accomplishes this by defining a distance parameter

$$\nu = \beta(\max(z_i) - \min(z_i))/(\max(A_i^2 + B_i^2))^{1/2}, \tag{3.13}$$

where β is a small number ($\beta = 0.1$ in Shepard (1968)). Then, given P, increments Δz_i are computed for each D_i according to

$$\Delta z_i = (A_i(x - x_i) + B_i(y - y_i))\frac{\nu}{\nu + d_i} \tag{3.14}$$

Obviously at every D_i, the x and y partial derivatives of the increment Δz_i are A_i and B_i respectively. The size of the increments are bounded by

$$|\Delta z_i| \leq \beta(\max(z_i) - \min(z_i)), \tag{3.15}$$

and approach 0 as $d_i \to \infty$. The final interpolating function is

$$f_4(x,y) = \begin{cases} \frac{\sum_i w_i(z_i+\Delta z_i)}{\sum_i w_i} & \text{if } d_i \neq 0 \text{ for every } i \\ = z_i & \text{if } d_i = 0 \text{ for some } i; \end{cases} \tag{3.16}$$

This interpolating function has the additional property that the partial derivatives evaluated at the data points have reasonable values. This is the final interpolating function the Shepard (1968) proposed; improvement in this method is achieved by Renka (1988) by making different choices of weights, w_i, and the "nodal functions," in this case $(z_i + \Delta z_i)$.

3.4 Calculating the light curve

Several separate programs are run in order to produce the light curves. Excepting the SS calculations which can optionally use manually specified parameters, the metric and stellar structure computation must be carried out for the desired combination of EOS, mass, and spin frequency. This takes place by running an instance of a program based on RNS (Stergioulas and Friedman, 1995), described in Section 2.2. The output of this program is a binary file containing the metric potentials and derivatives, the location of the star's surface as a function of latitude, the central energy density of the model, and the angular momentum of the star. This output is designed to be loaded by the other programs we use. The file for a single model is approximately 9 megabytes in size, corresponding to a computational grid of 201 × 401 divisions (angular × spatial grid points), and a single execution takes on the order of minutes, since the modified program is designed to iterate over several models to find a desired mass and frequency. The standard RNS algorithm computes models given the central energy density and ratio of polar to equatorial axes, $\bar{r}_p/\bar{r}_e$.

The next stage of the calculation is to generate the tables used for ray interpolation. These are files containing data describing null geodesics for a fixed initial latitude θ_i and radius $\bar{r}_s(\theta_i)$, ranging over all allowed initial conditions. This program uses the fastest version of the Runge-Kutta integrator, described above, since at this stage all we require is the mapping between initial conditions b, $\dot{\theta}_i$, and $\mathrm{sgn}(\dot{\bar{r}}_i)$, to the angular deflections of the photon trajectories $\Delta\phi$ and θ_f. The tables will depend on the approximation scheme being considered (Exact, OK, OS, SK, SS), since the allowed initial conditions and final integrals depend on the choice of metric and description of the stellar surface. Each latitude of the stellar model

requires a separate table, and for a given pulse profile, at least two tables are required for the northern and southern boundaries of the emitting region. In practice we have typically generated all of the tables for a given stellar model and approximation mode at a time, for typical angular separations of 2°. In the configuration used for the bulk of our results, a single table at a given latitude would contain approximately 10^4 separate integrals of the geodesic equations, and the results are stored in a file approximately 500 kilobytes in size. In the current configuration a single table would take approximately 1–3 CPU hours to compute on commodity Pentium IV class hardware. To compute 45 tables covering the whole of the upper hemisphere of a neutron star model takes on the order of 2 CPU days. Each invocation of this program is for a fixed θ_i, and so the task of calculating all tables for a given stellar model can be easily split up between different computers, for example in a cluster environment.

The next stage of the calculation requires the neutron star model and two of the tables computed in the previous step, corresponding to the upper and lower boundary of the emission region. The location of the observer θ_f for the desired pulse profile is also specified. With this information, we use Shepard's interpolation to compute the initial conditions b, $\dot{\theta}_i$, and $\mathrm{sgn}(\dot{\tilde{r}}_i)$ corresponding to photons originating at initial angular coordinates $(\phi_i = n(2\pi/N), \theta_i)$, and landing at coordinates $(0, \theta_f)$. $N = 180$ is the typical number of azimuthal subdivisions that we used, and n is an index running from 0 to $N - 1$. For each value n, an iteration takes place where Shepard's interpolation is used to obtain a guess for the desired initial conditions. The fast version of the Runge-Kutta integrator is used to check the guess. If the obtained angular deflections are not within a required tolerance, the result of the integration is added to the table and another guess is made. When this procedure converges on the required initial conditions, the slow version of the Runge-Kutta integrator is started to compute the time-of-flight and final directions of the light ray, and the result is saved. Obviously, this iteration will fail if the desired ray falls outside of the bounds of the scattered data, and in this case the location is marked as invisible to the observer. The collection of final integrated rays are written to a file. For 180 azimuthal divisions the files for a single initial latitude θ_i are several tens of kilobytes. In the current configuration, a single latitude may take anywhere from minutes to 1–2 CPU hours to calculate, depending on the viewing geometry and the metric being employed. This task is also well-suited to cluster computing, since the starting and stopping value of the index n can be selected at runtime and the results of the calculations merged to-

gether when all values of n have been computed. Two executions of this calculation are required for a single pulse shape, corresponding to the top and bottom of the emission region.

The final stage of the calculation simply reads in the "north" and "south" ray solutions from the previous step, and uses the steps enumerated in Section 2.4.2 to compute the pulse profile. In this thesis we have restricted ourselves to the bolometric flux from a small, isotropically emitting region on the surface of the star. For each location ϕ_e of the rectangular emitting region, the solid angle $\mathrm{d}\Omega$ subtended by the patch on the observer's sky is calculated, using Equations 2.73, 2.74, and 2.75. The average value of $(1+z)$ is calculated using Equation 2.50, and the arrival time of the flux $t_o = \phi_e/\Omega_\star + T(\phi_e)$ is calculated, where $T(\phi_e)$ is the average time-of-flight of photons to reach the observer from the emitting patch. Also, the factor $(1+\Omega_\star \mathrm{d}T/\mathrm{d}\phi|_{\phi=\phi_e})$ is calculated by finite differencing the time-of-flight on neighbouring bins. The bolometric flux is then taken to be

$$F(t_o) \propto \frac{\mathrm{d}\Omega}{(1+z)^4(1+\Omega_\star(\mathrm{d}T/\mathrm{d}\phi))}. \tag{3.17}$$

A final step rescales the maximum flux to value 1.0, and interpolates the calculated fluxes onto evenly-spaced arrival times. This interpolation step is necessary to aid with subsequent analysis, since the emission patches are spaced uniformly by azimuthal angle, and not by uniform increments of arrival time. In this step it is also possible to optionally disregard the time-of-flight $T(\phi_e)$ when computing t_o, since we wish to investigate the effect this approximation will have on the shape of the light curve. This program takes a few seconds to run and outputs short text files containing the results of the calculation.

We have also written a code implementing the method for a spherical star and Schwarzschild metric, following the independent method derived in Section 2.5. This is used partially as verification, to see that when the general method employs the SS approximation to compute a pulse profile, that it recovers what would be calculated by a code that is specialised for this purpose.

3.5 Verifying the implementation

We have implemented a new method of calculating the observed light curve for surface emission from rotating neutron stars, which makes use of the exact spacetime metric, and accounts for the time-of-flight of photons and the motion of the emitting region. It is not possible to check the full version of this calculation because

both the method used and the quantity calculated are new. However, it is possible to check that important quantities in the code are self-consistent, and that when the code is run with approximations to the exterior metric and stellar structure, that the output matches (or can be sensibly compared to) what can be obtained using more straightforward methods.

3.5.1 Checking $\bar{r}_s(\theta)$

We modified a third-party computer code, RNS (Stergioulas and Friedman, 1995), to calculate the location of the stellar surface, and to output this in a file in addition to the spacetime metric potentials and their derivatives, and several other physical values which describe the stellar model corresponding to a supplied EOS, mass, and frequency.

To check that the obtained location of the stellar surface, $\bar{r}_s(\theta)$, is correct, we can calculate the angle formed between the normal to the star's surface as defined by the four-acceleration of the fluid elements at the surface, described in Section 2.3.4, and the geometric normal defined by the coordinate position of the surface, described in Section 2.3.4. The former quantity depends on the metric potentials and their derivatives, while the latter depends on a derivative of $\bar{r}_s(\theta)$. In an equilibrium configuration, these definitions should coincide and the angle formed between these vectors should be 0.

We found that for the exact metrics this angle was on the order of 10^{-4} degrees or smaller, and for the oblate approximations OK and OS, that this angle was on the order of 10^{-1} degrees. For the spherical approximations SK and SS, where this check ought to fail, this angle was as large as order 10 degrees for the models that were the most oblate.

These checks suggest that values of $\bar{r}_s(\theta)$ calculated in our customised version of RNS are consistent with the values of the metric components.

3.5.2 Comparison with Schwarzschild light curves

Spherical models

In Section 2.5, a method to calculate the light curve using the approximation of a spherical star and Schwarzschild exterior spacetime was presented. Using a completely separate computer code, we can evaluate the flux according to Equation 2.136 for a set of parameters, and compare the result to the output of the general code we developed. If the results are the same, then we have confirma-

tion that, at least for this set of assumptions, the programs calculate equivalent quantities and the general method we are proposing is correct.

In particular, the verification code relies only on the numerical intergration of $\psi(b)$ and $T(b)$ (Equations 2.117 and 2.118, respectively) and a root-finding algorithm to determine $b(\psi)$; we used Ridder's method (Press *et al.*, 1988) on a precomputed array of $\psi(b)$ values to accomplish this. The general code is what we will eventually use with the RNS numerical spacetimes and an accurate calculation of the stellar oblateness, except for verification purposes we are running it for the SS approximation described above. This method depends on the general solution of the geodesics chosen in the less convenient coordinate system where $\theta = \pi/2$ corresponds to the star's equatorial plane (i.e., the plane normal to the spin axis), and on the determination of the solid angle projection according to the method described in Section 2.4.1, which involves inner products of pairs of rays arriving at the observer which can be traced back to a patch of fixed angular size on the star.

In Figure 3.1, we show the observed bolometric flux calculated from a small emitting region for a variety of geometries and M/R values, and the equivalence of these two methods in these cases is apparent.

Oblate model compared to spherical model

A further check is to compare the OS approximation to an appropriately chosen SS calculation. We do this as follows: given θ_e for the emission region, we can calculate the radius $R(\theta_e)$ in the OS approximation, and run the SS calculation for the same set of parameters. In what follows it is useful to consider a model where the effect of oblateness is not small; we will use the SS and OS approximations to the model calculated with EOS L for $\Omega_\star = 600\,\mathrm{Hz}$, and $M/M_\odot = 1.4$. This particular model is spinning at a rate close to its breakup speed of 742 Hz, which results in distortion of the star's surface. An indication of the degree of oblateness is given by the axes ratio for this model which is $\bar{r}_s(0)/\bar{r}_s(\pi/2) \approx 0.83$. We wish to examine the effect arising from the different orientations of surface elements in the SS and OS calculations, and so we must pick θ_e away from the spin axis and the equator, so that $\mathrm{d}\bar{r}_s(\theta)/\mathrm{d}\theta \neq 0$. For this section, all comparisons are made using $\theta_e = 41°$, $\theta_o = 20°$. For this situation, we use $R = 14.7538$ km for the corresponding SS model. Also, with these particular values the code will integrate to $\bar{r}_f = 696.32$ km for the OS model, and $\bar{r}_f = 617.41$ km for the SS model.

First we check that the redshifts and $\mathrm{d}t_r/\mathrm{d}t_e$ are the same for both the OS and SS calculations, which are depicted in Figures 3.2 and 3.3 respectively. Both figures

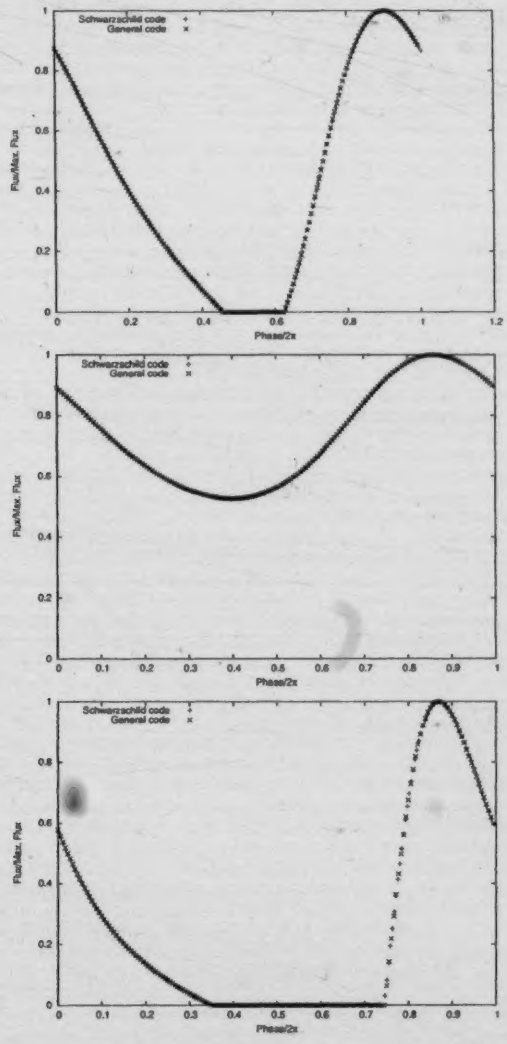

Figure 3.1: Comparing direct Schwarzschild calculation of bolometric flux to SS approximation in the general code: These figures show the calculated bolometric flux as a function of the observed time. All three calculations have rotation rate $\Omega_\star = 600\,\mathrm{Hz}$, and mass $M/M_\odot = 1.4$. The top panel is for a star with $GM/(c^2R) = 0.211$, and Schwarzschild radius $R = 9.78\,\mathrm{km}$, corresponding to values at the equator for a model computed with EOS A; the emission is from $\theta_e = 41°$, and observation from $\theta_o = 100°$. The middle panel and bottom panels are for a star with $GM/(c^2R) = 0.126$, $R = 16.38\,\mathrm{km}$, corresponding to values at the equator for a model computed with EOS L. The middle panel was calculated for $\theta_e = 41°$, $\theta_o = 20°$. The bottom panel has $\theta_e = 85°$, $\theta_o = 100°$.

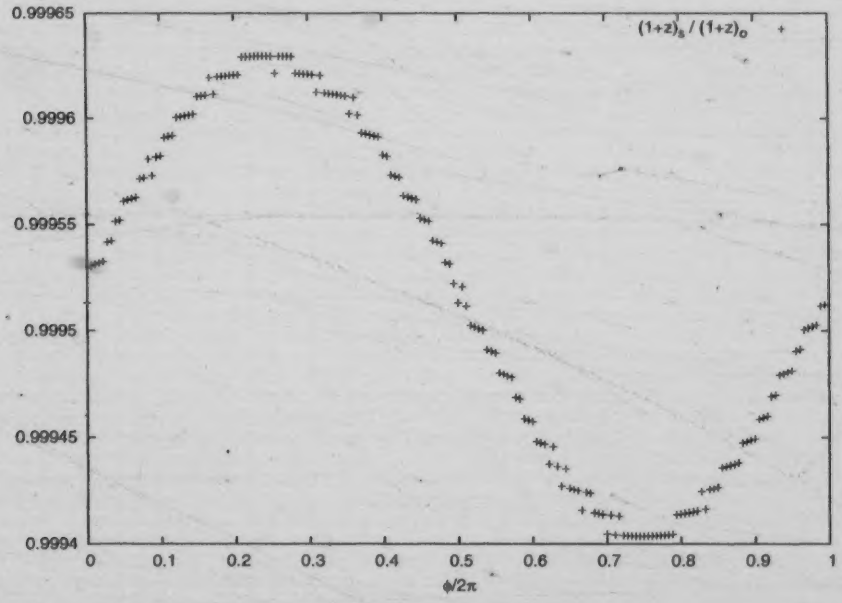

Figure 3.2: Comparison of $(1+z)$ in spherical and oblate codes, when M/R and R is matched: This is a plot of the ratio of $(1+z)$ values calculated in the OS and SS calculations as a function of rotational phase, when all quantities are otherwise the same (to finite precision).

are plots of the ratios of the relevant values between the OS and SS calculations as a function of rotation phase (*not* observed phase). Ideally these graphs should show a constant value of 1 at all times; in practice there is a limit to the precision. We see that the redshift ratio in Figure 3.2 has very weak rotational modulation around a value of 0.99953; which tends to indicate that the calculation of z is the same in either the SS or OS case as intended. The slight shift away from 1 and weak modulation is not unreasonable because for the purpose of this calculation the SS parameters were manually set at runtime, and the parameters M, R, $\Omega_\star$ were not input to better than the indicated accuracy. Similarly, the graph of $\mathrm{d}t_r/\mathrm{d}t_e$ In Figure 3.3 shows a very mild rotationally-modulated error about 1. So we have demonstrated that in these respects the SS and OS calculations agree, which they must for a correctly implemented code.

These calculations must differ, however, on the projected solid angle $\mathrm{d}\Omega$. However, it is also possible to see that they differ in a predictable way: one naïvely expects that the difference in the projected solid angle between the SS and OS

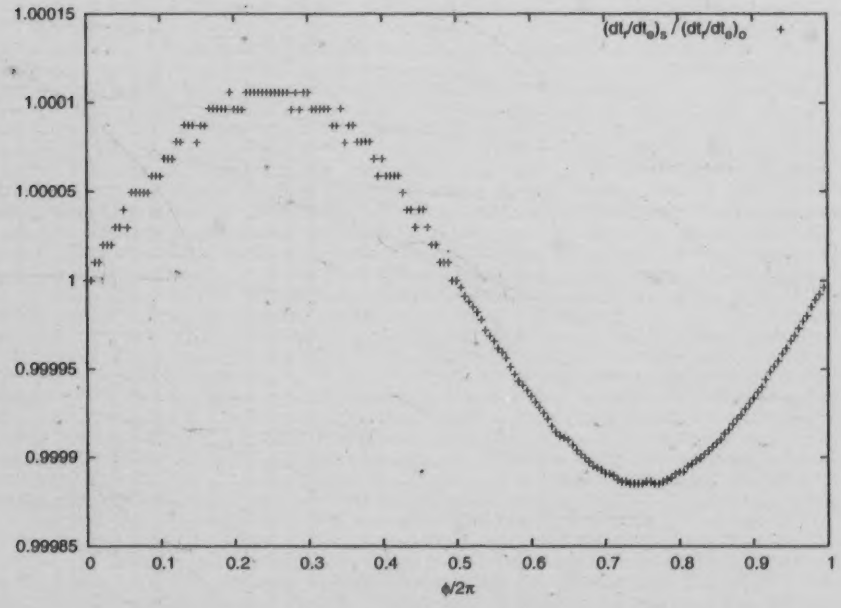

Figure 3.3: Comparison of $\mathrm{d}t_r/\mathrm{d}t_e$ in spherical and oblate codes, when M/R and R is matched: As with Figure 3.2, this is another check that quantities that ought to match between the spherical (SS) and oblate (OS) calculations match to reasonable precision.

calculations should be governed by

$$\frac{\mathrm{d}\Omega_{\mathrm{OS}}}{\cos\alpha_{\mathrm{OS}}} \approx k\frac{\mathrm{d}\Omega_{\mathrm{SS}}}{\cos\alpha_{\mathrm{SS}}}, \tag{3.18}$$

where α is the zenith angle as measured by an observer at the surface of the star, and k is a constant chosen to account for the different radial location of the observer in the OS and SS cases which results because of a coordinate choice that is made in the computer code. In terms of the above relations, we expect that

$$k \approx D_{\mathrm{SS}}^2/D_{\mathrm{OS}}^2, \tag{3.19}$$

where D represents the radius of the observer's sky, and so $D \approx \bar{r}_f$ for the geodesic integrations. In Figure 3.4, we show the ratio $k\mathrm{d}\Omega_{\mathrm{SS}}/\mathrm{d}\Omega_{\mathrm{OS}}$ agrees with the ratio $\cos\alpha_{\mathrm{SS}}/\cos\alpha_{\mathrm{OS}}$ when $k = 0.7988$. In this case k was chosen by inspection, but $(\bar{r}_f^2)_{\mathrm{SS}}/(\bar{r}_f^2)_{\mathrm{OS}} = 0.7862$ in this case, indicating that k is accounted for to within 2% by the different final values of $\bar{r}_f$ used in these two calculations. That this relation isn't exact isn't surprising, because we have made a number of idealisations; for example, about the "radius" D of the observer's sky, and that we are comparing emitting regions of fixed angular size and not fixed area. Another way of presenting the same material is that the above amounts to a claim that $\bar{r}_f^2\mathrm{d}\Omega/\cos\alpha$ is a constant function of rotational phase, and that this constant ought to be the same for both the SS and OS calculations. In Figure 3.5 we check this, and see that this does approximately hold to about the same level.

The fact that the difference in the solid angle projection between the SS and OS modes of calculation can generally be understood so well in basic terms serves as a check that the method created for calculating the solid angle projection via inner products in the general code is a correct one. It is also suggestive of a means by which existing computer codes based on the Schwarzschild formalism of Section 2.5, similar to the independent code we used earlier in this section, might be adapted for rapid rotation to some effect by properly accounting for oblateness which becomes a factor in these models. To make this adaptation would require a specification $R_s(\theta)$ for the location of the surface of the star, which in principle could be used to obtain a correction factor like $\cos\alpha_{\mathrm{obl.}}/\cos\alpha_{\mathrm{sph.}}$ for the calculated flux. Making this adaptation would also require care with the visibility condition $\cos\alpha > 0$ as in certain circumstances light is blocked in the oblate case that would otherwise be visible, and vice versa. In Section 4.5 a model of $R_s(\theta)$ is given in terms of polynomials and simple parameters, and the correction factor implied by

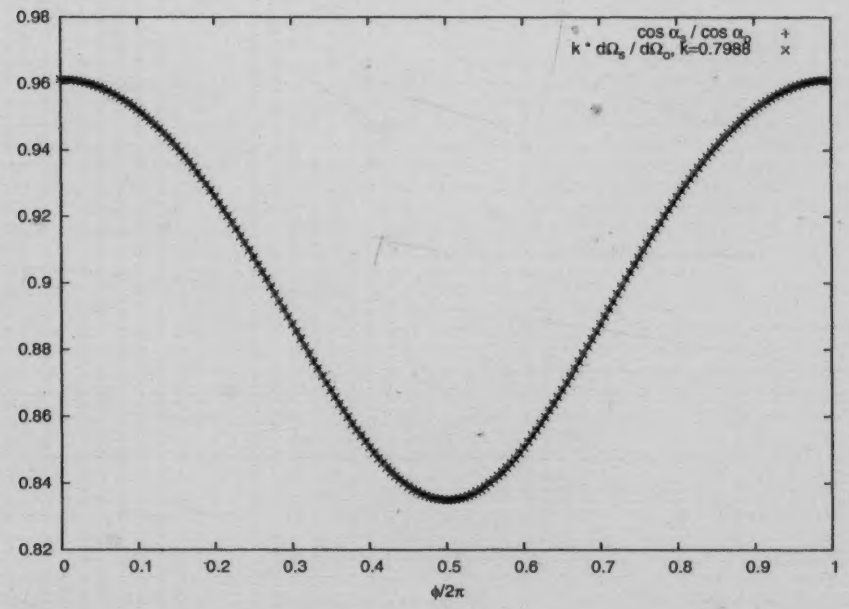

Figure 3.4: Comparing $k\mathrm{d}\Omega_{\mathrm{SS}}/\mathrm{d}\Omega_{\mathrm{OS}}$ with $\cos\alpha_{\mathrm{SS}}/\cos\alpha_{\mathrm{OS}}$: This is a check that the solid angle projections calculated in the SS and OS methods scale in a manner determined by the shape of the surface.

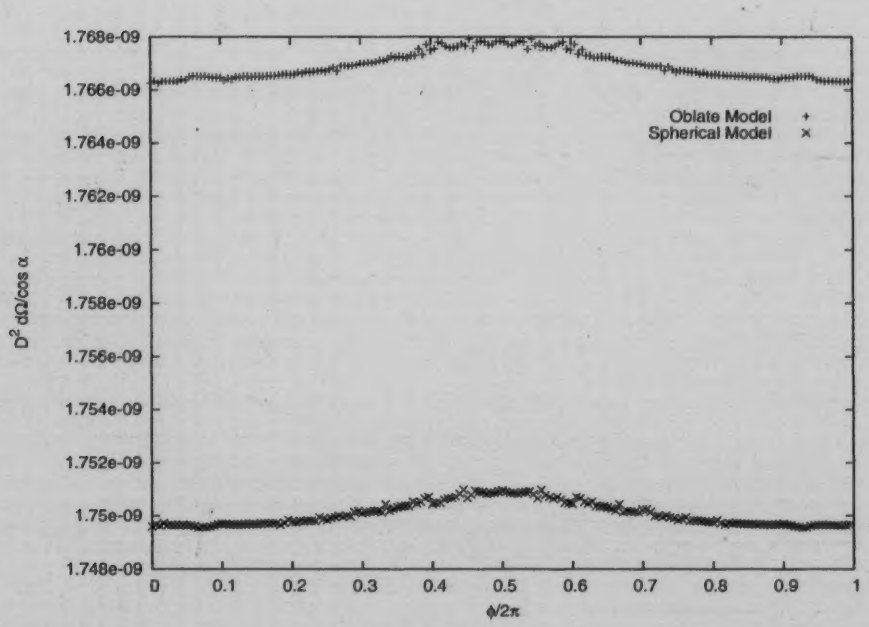

Figure 3.5: Checking constantness of $\bar{r}_f^2 \mathrm{d}\Omega / \cos\alpha$: This check is related to Figure 3.4; it is another way of seeing that the solid angle projection is determined by the orientation of the emitting region.

these observations is given explicitly.

3.5.3 Checking Carter's constant

Comparisons to cases calculated using the Schwarzschild metric are only useful up to a point. An additional check on our general code can be made by running calculations in either the OK or SK configuration, where the exterior metric is approximated as Kerr with $a = J/M$; J is obtained via the RNS structure calculation. In the Kerr spacetime, there is an additional symmetry beyond stationarity and axisymmetry which results in the quantity

$$K = (\bar{r}^2 e^{2\alpha}(\ell^\theta/E))^2 + b^2/\sin^2(\theta) + a^2\sin^2(\theta) \tag{3.20}$$

being conserved along the photon's world line. K is Carter's constant (Carter, 1968). By looking at the initial and final values of Carter's constant, we found that the change was typically on the order of a few parts in 10^5 when the exterior spacetime was Kerr, which suggests that the computer code for the geodesic integration functions correctly. When the general code is run with the exact exterior metric, the relative change in Carter's constant increases to up to a few parts in 10^2; we don't expect Carter's constant to be conserved when using the exact exterior metric since the conservation of K is a result that is special to Kerr spacetimes.

3.5.4 Checking time-of-flight & future improvements

In its current configuration, the factor $1 + \Omega_\star \mathrm{d}T/\mathrm{d}\phi$ appearing in the flux integral is calculated by direct finite-differencing the times-of-flight T over equally-spaced divisions in ϕ_e. Considering Equation 2.109, it would be better to modify the code so that it calculates this factor only in terms of b and $\Omega_\star$; this is an opportunity for future improvement of the code. As it is, the slow integration which obtains the time-of-flight after an appropriate combination of initial conditions is found must be run at a high-enough precision that the derivative of T can be accurately calculated numerically; the precision of this integral can be relaxed somewhat (and made faster) if we use the analytical expression for this factor instead. This is a trivial change to make; the more time-consuming part is re-tuning the accuracy controls for the slow integral so that the required precision in $\dot{\theta}_f$ is retained.

The current configuration at least allows us to check that the times-of-flight are being calculated correctly, by comparing $1 + \Omega_\star \mathrm{d}T/\mathrm{d}\phi$ with $1 - \Omega_\star b$. In Figure 3.6, the quotient of these quantities is plotted, indicating agreement at the level of

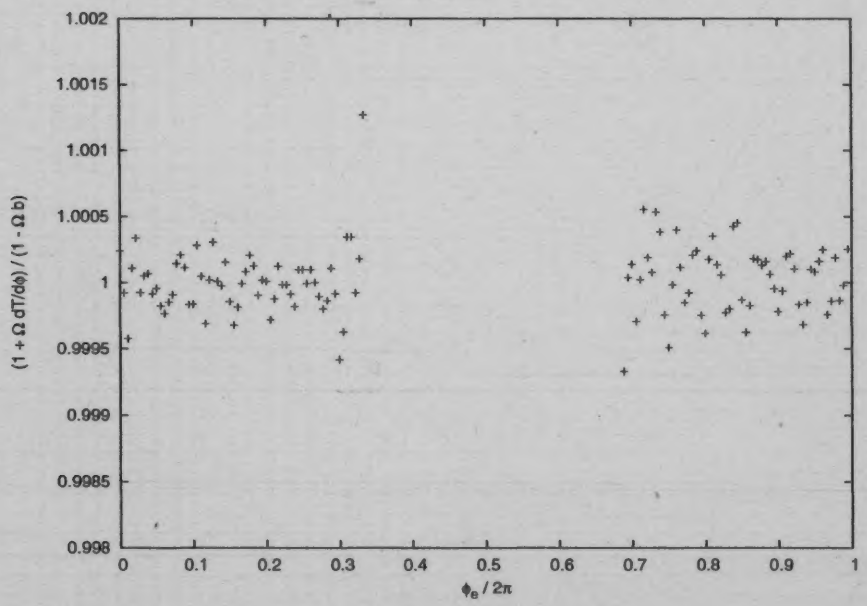

Figure 3.6: Verification of time-of-flight via its numerical derivative: Equation 2.109 says that $1 + \Omega_\star \mathrm{d}T/\mathrm{d}\phi = 1 - \Omega_\star b$. Using the finite-differenced derivative of T to evaluate the left-hand side, and the interpolated value of b for the right-hand side, we check that the correct correspondence exists between T and b by plotting $(1 + \Omega_\star \mathrm{d}T/\mathrm{d}\phi)/(1 - \Omega_\star b)$. In this case, we used an EOS L stellar model with $\Omega_\star = 600\,\mathrm{Hz}$, $M = 1.4M_\odot$, $R = 16.38\,\mathrm{km}$, $GM/c^2R = 0.126$ (EOS L), $\theta_e = 41°$, $\theta_o = 100°$. The agreement of these quantities is within 0.15%.

0.15%. We can be confident that the times-of-flight are calculated correctly, and that the error resulting from using the finite-differenced derivative is acceptably small.

Chapter 4

Results

4.1 Introduction

Observations of pulsed light emitted from the surface of a neutron star have the potential to constrain the star's mass and radius, and so the equation of state of the matter comprising the neutron star (Lattimer and Prakash, 2001). One can see that this information is encoded in the light curve roughly via the velocity of the emission region (which scales with R), and the star's compactness (i.e., M/R). The velocity controls the Doppler boosting of photon energies and the special relativistic Terrell (Terrell, 1959) effect, which largely determines the asymmetry of the lightcurve. The compactness controls the degree to which light can "bend" around the star, which determines the length of any eclipse which may be present in the data. In cases where the associated velocities are not relativistic, it may be that only M/R can be obtained from the light curve since the rotational variation of redshift becomes unimportant (alternatively, some additional mechanism affecting the model light curve which relies on R would need to be introduced). Since both of these effects require light to be emitted from the surface of the star to be significant, light curves obtained from observations of radio pulsars are unlikely to be useful in the sense of constraining these neutron star properties, since for these objects light is probably emitted close to the light cylinder. On the other hand, most X-ray pulsars emit light liberated by accreting matter which is decelerated close to the surface of the neutron star, or else light emitted by thermonuclear burning of accreted matter on the surface. There are efforts being made to use X-ray timing observations from accreting X-ray binaries to provide a determination of the global properties of neutron stars. In practice, information is extracted from the light curve by adjusting the parameters of a calculable model so as to find the

parameters that are most consistent with the observations. Realistic model light curves generally incorporate parameters describing one or more spectral components which may have different associated anisotropies, as well as the shape and size of the emitting region.

The first attempts to model observed X-ray pulsar light curves did not include gravitational effects and used polar cap models of the emitting region (Wang and Welter, 1981; Leahy, 1990, 1991). The latter of these models were motivated by radiative transfer calculations of the emissivity by caps and columns of Mészáros and Nagel (1985). Pechenick *et al.* (1983) set out a formalism to account for gravity in such models for slow rotation, by tracing out the paths of photons in the Schwarzschild spacetime. This formalism was used to calculate the pulse profile produced by radiation from hot spots and accretion columns by Riffert and Mészáros (1988), which in a follow-up paper was extended to incorporate a spectral model (Mészáros and Riffert, 1988). Leahy and Li (1995) accounted for gravity in fits of cap models to observed pulse profiles. Other accretion column models with light-bending were computed by Kraus (2001), Leahy (2003a) and Kraus *et al.* (2003). In an analysis of the occultation sequence of the X-ray pulsar Her X-1 by Scott *et al.* (2000), it was determined that the pulse profile corresponded to a pencil beam from the near pole and a gravitationally-focused fan beam from the far pole. This led to a quantitative model for the pulse shape of Her X-1 by Leahy (2004a), which in turn resulted in a constraint on M/R for the neutron star (Leahy, 2004b).

Clearly, the application of models based on Pechenick *et al.* (1983) to the analysis of conventional X-ray pulsars is adequate because the periods of these pulsars are so long (the fastest is 69 ms, most are > 1 s) that the gravitational field is well-approximated as Schwarzschild, and accounting for the motion of the emission region, to the extent that it's necessary, is trivially accomplished by inserting the appropriate factors to account for the rotation-induced blue-/redshift and the Terrell, or "snapshot," effect. The first millisecond period X-ray pulsar in a low-mass X-ray binary, SAX J1808.4-3658, was recently discovered by Wijnands and van der Klis (1998) and spins at a frequency of 400 Hz (Chakrabarty and Morgan, 1998). This is fast enough that the rotational speeds at the equator must be relativistic. An application of this category of model with corrections for relativistic motion to the pulse profile SAX J1808.4-3658 was undertaken by Poutanen and Gierliński (2003), to obtain a constraint on M/R. However, it should be noted that their model did not include time-of-flight effects, which at these speeds might reach a few percent of the rotation period. This is a failing that many of the models in

this category (but not all) share. Extensions to this Schwarzschild-based method of modelling the pulsed emission has been undertaken by Kapoor and Datta (1986) using the slowly-rotating neutron star metric, and by Kapoor (1991) using a weak form of the Kerr black hole metric (discarding terms of order a^2/R^2 and higher). Chen and Shaham (1989) developed a model using the full Kerr metric. Braje *et al.* (2000) made use of a Monte Carlo method to produce light curves using the full Kerr metric, and they made the important point that accounting for the varying photon travel times is necessary for the millisecond pulsars. This work was followed up in Braje and Romani (2001), where the authors pointed out that the differences introduced in their light curve calculation by using the Kerr metric instead of the Schwarzschild metric for the photon propagation introduced changes that were probably too small to measure, and that these changes were less important than the effects that rotation-induced oblateness would introduce for rapidly-rotating models. A separate model using the Kerr metric for photon propagation was developed by Bhattacharyya *et al.* (2005), and notably they used their model to obtain a constraint on neutron star parameters by fitting to the burst oscillation light curves of the accreting 3.2 ms pulsar XTE J1814-338.

One application of these models is to understand the observed phase lag of the low-energy light curve (e.g., in the soft X-ray band) compared to the high-energy light curve (in hard X-rays) for the same source, which may have its genesis in the relativistic motion of the emission region. A model of this was developed by Ford (1999) by accounting for special relativistic Doppler effects but neglecting gravity. This model was improved by incorporating gravity using the Schwarzschild metric and applied to the observed energy-dependent delays in SAX J1808.4-3658 by Ford (2000). Similar models were developed to model the oscillation amplitudes and energy phase lags during X-ray burst on rapidly-rotating neutron stars by Miller and Lamb (1998) and Weinberg *et al.* (2001). These models were further improved by Muno *et al.* (2002b) by incorporating the time-of-flight effects.

It is still early in the history of analysis of millisecond X-ray pulsar light curves, partly due to the paucity of suitably reduced data for analysis. In the literature that does exist, many of the techniques and tools used are borrowed, or at least inspired by, the profusion of models developed for slowly-rotating X-ray pulsars. One is forced to wonder to what extent these methods can be straightforwardly adapted to carry through analyses of observations of millisecond pulsars by including the relevant special-relativistic contributions. To what extent does the approximation of the spacetime as Schwarzschild matter? Does the inclusion of travel-time effects

matter? Do the effects of rotation on stellar structure matter? The answer to these questions in the case of slow X-ray pulsars is uniformly "no," but little prior analysis has been undertaken to answer these questions in the case of millisecond pulsars, and furthermore it seems reasonable to assume that at least under certain circumstances these effects can have significant implications. The main complication in assessing the applicability of these approximations has been the absence of a calculation which can account for these effects to whatever extent they matter. We have described and implemented a model which accounts for all of these effects in earlier chapters, which is the main tool by which we attempt to answer these questions. We restrict our considerations this way to observed bolometric flux which is isotropically emitted by an infinitesimal emission region on the surface of the neutron star, because problems identified in this simple case will persist in some form when complications such as emission spectra and emitting region shape are included.

This chapter is organised as follows: First, in Section 4.2 we discuss the models we have selected which are used in the work that follows. In Section 4.3, we consider a simplified situation in which one wishes to use light curves which are calculated without accounting for the different integrated times-of-flight of photons to draw conclusions about hypothetical data where the effect of the times-of-flight are present. Section 4.4 considers the effect of approximations to the spacetime metric and the effect of stellar oblateness, in the sense of comparing the forward calculations with various approximations for the same set of parameters, and also in the sense of utilising an approximate method for obtaining fits to hypothetical data. It becomes apparent that adequately including the effect of oblateness is important for rapid rotation, so in Section 4.5 a model is developed which specifies the surface value of the Schwarzschild R coordinate as a function of polar angle, given a single dimensionless quantity involving M, R at the equator, and Ω_*. An initial attempt is made to incorporate this model into a simpler computer code with some success. Although this programme was not carried through completely, enough has been completed to indicate that it should be fruitful to modify other extant codes to incorporate a reasonable estimate of the effect of stellar oblateness using the model we have devised.

4.2 Choice of neutron star models

In the sections that follow, we will refer to the stellar models we used by equation of state (EOS) and the frequency $\Omega_\star$ of rotation. All of our models have $M = 1.4\,M_\odot$, which is a conventional choice for the fiducial mass of a neutron star. This choice is experimentally justified by the recent mass measurement of the neutron star in the recycled binary radio pulsar PSR J1909-3744 which has a mass $(1.44 \pm 0.02)\,M_\odot$ (Jacoby *et al.*, 2005). Other experimental justifications for this figure come from double neutron star systems containing slower radio pulsars, which with two exceptions have experimentally determined masses falling inside the range $(1.35 \pm 0.04)\,M_\odot$ (Thorsett and Chakrabarty, 1999). There is some evidence that neutron stars can be heavier than this canonical value: an extreme example is a recent measurement by Nice *et al.* (2005) who used precision measurements of the millisecond radio pulsar binary PSR J0751+1807 to determine a mass of $(2.1 \pm 0.2)\,M_\odot$ for the neutron star via its general relativistic orbital decay, which is the largest known neutron star mass. Future observations of this pulsar will improve this mass measurement. If its relatively high mass holds, it may lead to a significant constraint on the state of neutron star matter, since this mass exceeds or is at the upper end of the maximum mass that can be supported by several candidate equations of state (Lattimer and Prakash, 2001, 2004).

For this work we have chosen to use the candidate equations of state EOS A and L from the Arnett and Bowers (1977) catalogue which span a wide range of stiffness. EOS A is one of the softest equations of state, and EOS L is one of the stiffest allowed by present observations. For each EOS we have computed equilibrium models using RNS (Stergioulas and Friedman, 1995) for a number of different frequencies, spanning the range of frequencies observed in accreting millisecond pulsars. The parameters describing these models are given in Table 4.1. The EOS L, 600 Hz model is one that we return to a few times since it is the fastest and largest of the set; we expect that effects due to varying times-of-flight will be maximised (it is quite large, so has a relatively long light-crossing time), as well as effects due to deformation of the surface (or "oblateness," since it is spinning at a frequency quite near its breakup speed).

EOS	$\Omega_B/2\pi$[a](Hz)	$\Omega_\star/2\pi$ (Hz)	R[b](km)	$cJ/(GM^2)$	$GM/(c^2R)$	v/c[c]	$\omega_{eq}/2\pi$[d](Hz)
A	1387	100	9.57	0.036	0.216	0.03	16.8
		200	9.59	0.073	0.216	0.05	33.6
		300	9.62	0.109	0.215	0.08	50.2
		400	9.66	0.147	0.214	0.11	66.7
		500	9.71	0.185	0.213	0.13	82.8
		600	9.78	0.223	0.211	0.16	98.4
L	742	100	14.86	0.076	0.139	0.04	9.5
		200	14.95	0.154	0.138	0.07	18.9
		300	15.11	0.234	0.137	0.11	27.9
		400	15.36	0.318	0.135	0.15	36.4
		500	15.74	0.408	0.131	0.19	43.8
		600	16.38	0.508	0.126	0.24	49.0

[a] The break-up spin frequency for a star with the given mass and equation of state.
[b] The equatorial Schwarzschild radius.
[c] The speed of the neutron star at the equator measured by a static observer at the surface. Velocities are calculated with the full metric.
[d] The frame-dragging term at the equator; this is the angular velocity of a zero angular momentum particle at the equator.

Table 4.1: Neutron Star Models with Mass = $1.4\,M_\odot$

4.3 The effect of neglecting time-of-flight[1]

4.3.1 Introduction

In the case of Pechenick *et al.* (1983), slow rotation was being contemplated, and there was no need to account for variations of the travel time, or time-of-flight, of photons as the neutron star rotated because these variations were small compared to the rotation period. Some extant analyses of millisecond-period pulsars, for example the work on SAX J1808.4-3658 by Poutanen and Gierliński (2003), retain this assumption but are modified to incorporate the necessary special relativistic effects arising from the relativistic motion of the emitting region. Braje *et al.* (2000) pointed out that the varying photon time-of-flight was important to account for, but they did not carry through an analysis of how important it was from the point of view of systematic error that might be introduced by neglecting it. Section 2.5 contains a careful discussion of how light curves can be calculated in the Schwarzschild case. In that Section, it was shown that the calculation by Poutanen and Gierliński (2003) is correct in the sense that they are calculating an

[1] A version of this section was originally published as Cadeau *et al.* (2005), and substantial portions of this paper are incorporated here. Some details have been updated here to account for an erratum in the original publication, which is discussed in the text.

integral which is exactly correct in the case they consider (i.e., when the exterior spacetime is Schwarzschild and the star is taken to be spherical), but they omit the step of calculating the arrival time $t_o = t_e + T(b)$ by evaluating the time-of-flight integral at each step of the calculation. Instead they adopt the approximation that $t_o = t_e + \text{const}$ for the construction of their light curves, which results in a degree of distortion of the curves they obtained for rapid rotation. Put another way, they account for the fact that the arrival times are changing (because the emission region is moving) for the purpose of calculating the flux—this is the origin of the special relativistic factors they make use of—but they don't account for this in assigning the integrated flux to some observed time. The purpose of this section is to determine the worst extent to which this approximation will affect the outcome of the analysis of millisecond pulsar data. We make no claim as to the validity or not of the result in Poutanen and Gierliński (2003), but instead are using their treatment of the problem as but one example of several treatments which neglect times-of-flight in this manner.

To carry through this analysis, we begin by setting out some details of how the general treatment in earlier chapters simplifies when one is restricted to considering photons only in the equatorial plane. In Section 3.1.1, we set out a number of different approximation schemes that one can contemplate as variations on the basic method contemplated by Pechenick *et al.* (1983). In this section what we are doing is assessing the impact of using the SS approximation without times-of-flight included, as a means by which to obtain fits to data corresponding to the Exact method with times-of-flight included. In order to do this within the context of the simplifying assumption we're making in this section, a non-standard definition of flux is adopted where the emitting region is a small line segment located on the equator of the neutron star, and correspondingly the observer's sky is taken to be one-dimensional. Both the "Exact" and "SS without times-of-flight" methods are adapted to agree on this non-standard definition of flux so that the effect we are measuring will be a result only of the inclusion/exclusion of times-of-flight, and the approximation of the metric. In this section we are mainly concerned with the 300 Hz and 600 Hz models for both EOS A and L from Table 4.1. These models span a reasonable range of stiffness, and span observed frequencies of millisecond pulsars and X-ray burst oscillations.

4.3.2 Equations of motion

To accomplish our goal in this section, we consider a simplified case where we restrict our calculations to photons emitted from the equator which travel in the equatorial plane to the observer. This has the effect of simplifying the necessary calculations, as well as maximising the effect of the time-of-flight of photons. In this case, the motion of a photon is specified once the initial location and impact parameter are specified. The simplified equations of motion are:

$$\left(\frac{\mathrm{d}t}{\mathrm{d}\lambda}\right) = e^{-(\gamma+\rho)}(1-\omega b), \tag{4.1}$$

$$\left(\frac{\mathrm{d}\phi}{\mathrm{d}\lambda}\right) = \omega e^{-(\gamma+\rho)}(1-\omega b) + \frac{b}{\bar{r}^2}e^{\rho-\gamma}, \text{ and} \tag{4.2}$$

$$\left(\frac{\mathrm{d}\bar{r}}{\mathrm{d}\lambda}\right) = e^{-\alpha-\frac{1}{2}(\gamma+\rho)}\left((1-\omega b)^2 - \frac{b^2}{\bar{r}^2}e^{2\rho}\right)^{1/2}, \tag{4.3}$$

where b is the photon's impact parameter and λ is an affine parameter defined so that photon orbits are independent of energy. We are considering photons originating on the equatorial plane ($\theta = \pi/2$) emitted parallel to the equatorial plane ($u^\theta = 0$ initially). It is a straightforward calculation to show that such photons must remain in the equatorial plane, i.e., $\mathrm{d}\theta/\mathrm{d}\lambda = 0$.

Since the radial component of the four-velocity must be real, the impact parameters must lie in the range $b_{\min} \leq b \leq b_{\max}$, where the minimum and maximum impact parameters are:

$$b_{\min} = -\bar{r}e^{-\rho}\frac{1}{1-\omega\bar{r}e^{-\rho}}, \text{ and} \tag{4.4}$$

$$b_{\max} = \bar{r}e^{-\rho}\frac{1}{1+\omega\bar{r}e^{-\rho}}, \tag{4.5}$$

where the metric potentials are to be evaluated at the point at which the null ray originates, i.e., at the surface of the star. The frame-dragging term is positive, so the effect of rotation is that $|b_{\min}| > |b_{\max}|$. As a result, rotation allows an observer to see more of the side of the star which is moving away from the observer, as shown in Figure 4.1. In this figure, b_S corresponds to the maximum value of the impact parameter allowed for a static star.

In Figure 4.1 we illustrate the deflection of photons from the point of emission on the star to the observer. We define the azimuthal location of the distant observer to be at $\phi = 0$. A photon with impact parameter b hits the observer if it was emitted at azimuthal angle ϕ_e. The initial emission location is found by dividing

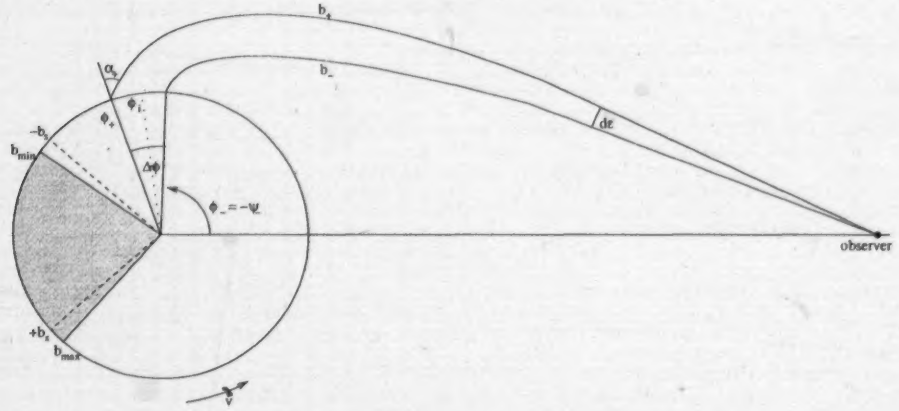

Figure 4.1: Angles in the simplified 1-D case. This figure was originally published as Figure 1 of Cadeau *et al.* (2005).

Equation 4.2 by Equation 4.3, and integrating from the star's surface to the distant observer:

$$-\phi_i(b) = \int_{\bar{r}_e}^{\infty} e^{\alpha-\frac{1}{2}(\gamma+\rho)} \frac{\omega(1-\omega b) + be^{2\rho}/\bar{r}^2}{((1-\omega b)^2 - b^2 e^{2\rho}/\bar{r}^2)^{1/2}} \, \mathrm{d}\bar{r}. \tag{4.6}$$

The deflection angle ψ is defined by $\psi = -\phi_i$. In the calculation of flux from a star, both the quantities $\psi(b)$ and $\mathrm{d}\psi/\mathrm{d}b$ are of importance. These quantities are plotted for the 600 Hz EOS L model in Figure 4.2. In addition, we show the deflections calculated using the SS approximation. The differences between the calculations with and without rotation are very small. The worst errors occur at the limbs of the star, so these differences are only likely to be of importance if the light is preferentially emitted in directions close to the horizontal.

4.3.3 Times-of-flight

To accurately model pulse shapes, we account for the different amounts of coordinate time that photons emitted from different regions of the star will take to reach the observer. Once the times-of-flight—alternatively, the times-of-arrival (TOA)—are known, the photons can be placed into the correct detector timing bins. The choice of zero time is arbitrary, so we have chosen a value of zero TOA for a photon with zero impact parameter. For photons emitted with the maximal values of impact parameter, the TOA is similar to the light travel time across the star. For the EOS L, 600 Hz model with $R = 16.38$ km, the light travel time is close to 80 μs. Compared to a spin period of 1.6 ms, this corresponds to a 5% effect, which

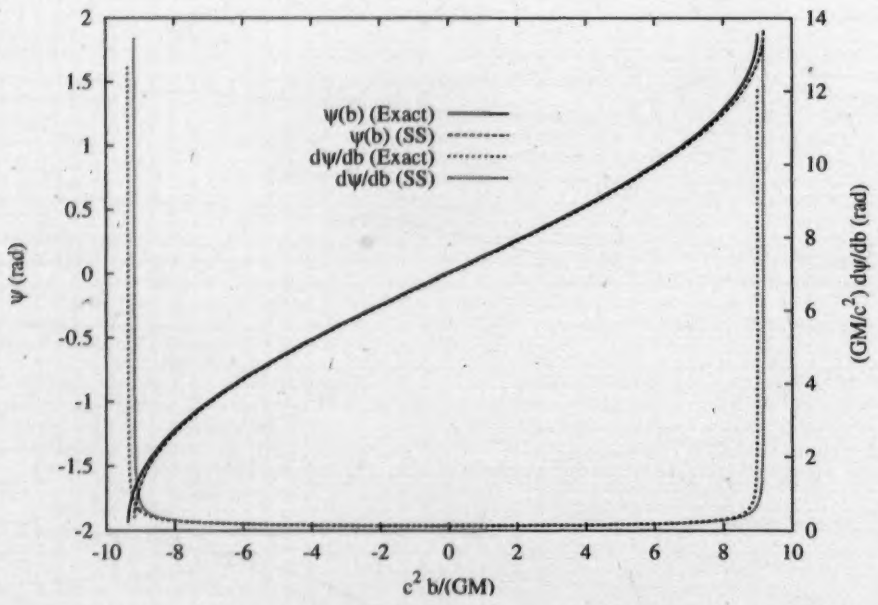

Figure 4.2: Bending angle $\psi(b)$ and $\mathrm{d}\psi/\mathrm{d}b$ for photons in the equatorial plane, calculated using both the exact metric and using the corresponding SS metric for the EOS L, 600 Hz model. This figure was originally published as Figure 2 of Cadeau *et al.* (2005).

will be seen to have a significant effect on the calculated pulse shapes.

The TOA is calculated by dividing Equation 4.1 by Equation 4.3, integrating from the star's surface to the distant observer and then subtracting off the corresponding quantity for a $b = 0$ photon. This yields the following formula for the arrival times $T(b)$:

$$T(b) = \int_{\bar{r}_e}^{\infty} e^{\alpha - \frac{1}{2}(\gamma+\rho)} \left(\frac{(1-\omega b)\bar{r}}{((1-\omega b)^2\bar{r}^2 - b^2 e^{2\rho})^{1/2}} - 1 \right) \mathrm{d}\bar{r}. \tag{4.7}$$

In Figure 4.3 we plot the TOA for the 600 Hz EOS L model using both the Exact method and SS approximation. Note that in the Exact calculation, the retrograde photon takes longer to reach the observer than the prograde photon. This is due to the frame-dragging effect. The magnitude of this effect is about 1/10 of the effect due to the light-crossing time in the corresponding SS models so we expect that for most timing applications that it will not be detectable.

4.3.4 Redshift

In our units, the photon's energy as measured by an observer far from the star has been normalized to unity. Any observer with four-velocity u^a measures a photon energy of $E_u = -\ell^a u_a$, where the photon's four-velocity components $\ell^a = \mathrm{d}x^a/\mathrm{d}\lambda$ are given in Equations 4.1–4.3. The star's four-velocity at the equator is

$$u^a = \frac{1}{V}\left(t^a + \Omega_\star \phi^a\right), \tag{4.8}$$

where $\Omega_\star$ is the star's angular velocity as measured by an observer at infinity, and the normalization condition $u^a u_a = -1$ yields

$$V^2 = e^{\gamma+\rho}\left(1 - (\Omega_\star - \omega)^2 \bar{r}^2 e^{-2\rho}\right), \tag{4.9}$$

where all quantities are evaluated on the star's equator.

The redshift factor $(1 + z)$ between light emitted at the star's equator and detected by an observer at infinity is

$$1 + z = e^{-\frac{1}{2}(\gamma+\rho)} \frac{(1 - \Omega_\star b)}{\sqrt{1 - (\Omega_\star - \omega)^2 \bar{r}^2 e^{-2\rho}}}. \tag{4.10}$$

Note that the quantity $v^2_{\mathrm{ZAMO}} \equiv (\Omega_\star - \omega)^2 \bar{r}^2 e^{-2\rho}$ appearing in the denominator is the square of the velocity of the star's fluid as measured by an observer with zero

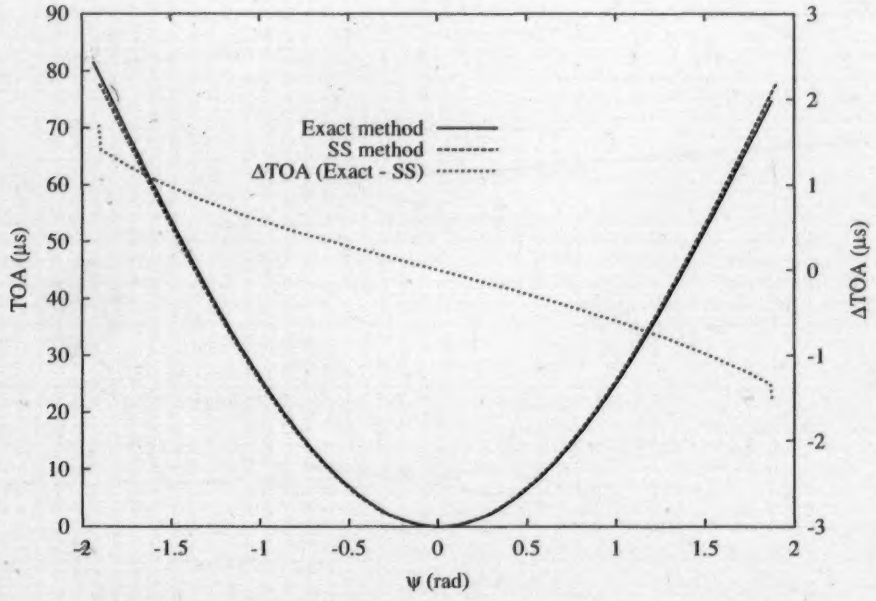

Figure 4.3: Times-of-flight as a function of bending angle: This plot shows times-of-flight (TOA) as a function of bending angle ψ calculated in both the Exact case and the SS case for the 600 Hz EOS L model. To illustrate the magnitude of the difference between the two calculations, we have also plotted the difference between them on the right-hand axis, "ΔTOA." This plot was originally published as Figure 3 of Cadeau *et al.* (2005).

angular momentum; i.e., an observer with $u_\phi = u^{\bar{r}} = u^\theta = 0$.

4.3.5 Angles between Photons

In a more general calculation of flux from a two-dimensional emitting area on the star, we would need to calculate the solid angle subtended by the area, as viewed by the observer at infinity. In this section (4.3), we are only including the flux of photons emitted from a segment of the equator into the equatorial plane. Adopting this special one-dimensional emission region means that observed radiation will subtend zero solid angle in the observer's sky. The most straightforward way of adjusting the usual definition of flux for this simplified emission region is to define flux in terms of an integral over angle in the observer's one-dimensional "sky" which coincides with the equatorial plane.

In Figure 4.1 we show a curve of angular extent $\Delta\phi$ on the star, and the angle measured by the observer at infinity between the two photons emitted from the endpoints (points ϕ_- and ϕ_+) is $\mathrm{d}\varepsilon$. If the impact parameters for these two photons are related by $b_+ = b_- + \mathrm{d}b$, the angle observed between the two photons reduces at infinity to

$$\mathrm{d}\varepsilon = \frac{\mathrm{d}b}{r}, \tag{4.11}$$

if both photons are restricted to move only in the equatorial plane. This is a well-known result in the Schwarzschild spacetime, but to obtain it in general, proceed by letting the two photons have four-velocities ℓ^a and m^a, with impact parameters b_+ and b_-, respectively. The angle the distant observer measures is calculated via the "cos angle" relation, which is also relied on for the results in Sections 2.3.4 and 2.4.1: The observer has $u^a \propto t^a$, and we define the projection operator as $h^{(\infty)}_{ab} \equiv g_{ab} + u_a u_b$ and the magnitudes of the projected null vectors as $\ell^u \equiv |\ell_\perp| = |h^{(\infty)}_{ab}\ell^b|$. The angle is calculated by the inner product of the projected vectors:

$$\begin{aligned}
\cos\varepsilon &= \frac{h^{(\infty)}_{ab}\ell^a_\perp m^b_\perp}{\ell^u m^u} \\
&= \omega(b_+ + b_-) + b_+ b_- \left(\frac{e^{2\rho}}{\bar{r}^2} - \omega^2\right) \\
&\quad + \sqrt{\left[(1-\omega b_+)^2 - \frac{b_+^2 e^{2\rho}}{\bar{r}^2}\right]\left[(1-\omega b_-)^2 - \frac{b_-^2 e^{2\rho}}{\bar{r}^2}\right]}.
\end{aligned} \tag{4.12}$$

This formula is only valid when the photons are restricted to move in the equatorial plane, i.e., $u^\theta = 0$. To get the infinitesimal version of this equation, put $b_+ = b_- + \mathrm{d}b$,

and Taylor expand the left-hand side for small angles $\mathrm{d}\varepsilon$. Expanding the right-hand side in $\mathrm{d}b$ and equating the second-order terms gives:

$$\mathrm{d}\varepsilon^2 = -\mathrm{d}b^2 \left[(1-\omega b_-)^2 - \frac{b_-^2 e^{2\rho}}{\bar{r}^2}\right] \left[\frac{\omega^2\bar{r}^2 - e^{2\rho}}{\bar{r}^2(1-\omega b_-)^2 - b_-^2 e^{2\rho}} - \left(\frac{\omega^2 b_- \bar{r}^2 - b_- e^{2\rho} - \omega\bar{r}^2}{\bar{r}^2(1-\omega b_-)^2 - b_-^2 e^{2\rho}}\right)^2\right]. \tag{4.13}$$

In the large $\bar{r}$ limit, ω falls off as $1/\bar{r}^3$, so to leading order in $1/\bar{r}$ the first term in square brackets is ~ 1 and the second term in square brackets is $\sim -e^{2\rho}/\bar{r}^2$. So we have for large $\bar{r}$,

$$\mathrm{d}\varepsilon = \frac{e^{\rho}\mathrm{d}b}{\bar{r}}, \tag{4.14}$$

and in terms of the usual Schwarzschild r coordinate given by Equation 2.6, this is

$$\mathrm{d}\varepsilon = \frac{\mathrm{d}b}{r}, \tag{4.15}$$

which is Equation 4.11. Note Equation 4.11 applies to the case of an emitting region that is not moving. An additional factor must be brought in to account for the "snapshot effect" as discussed in Section 2.4.2: at an instant of observer's time, an observer actually sees an angle $\mathrm{d}\varepsilon/(1-\Omega_\star b)$.

4.3.6 Outline of Numerical Method

To accomplish our goal, there are two main tasks that need to be carried out: first, we need a method to compute the pulse profile for the special case under consideration using the exact metric and including time-of-flight effects; these calculations will be what we regard as "data" for fitting in Section 4.3.8. Second, to accomplish this fitting we need a method to quickly calculate a number of light curves using the Schwarzschild metric without times-of-flight included. In principle the same method could be used for both tasks with the appropriate adaptations, but it was more convenient to carry out the former task using an early version of code described in Chapter 3 to compute the exact light curves, and a special code to calculate the Schwarzschild light curves which is similar to what might ordinarily be done in other implementations of the method described by Poutanen and Gierliński (2003) (we are also aware of an equivalent, but independent, implementation by Leahy (2003b)), but which has been modified for our case of a one-dimensional emission region located and observed in the equatorial plane. For completeness, we describe both calculations here.

1-D version of Exact calculation

The Exact version of the calculation proceeds as follows: We discretise the period of the azimuthal coordinate ϕ into N bins and keep track of the fluxes $F(i)$ and arrival times $t_o(i)$, where i is the bin index running from 0 to $N-1$. The size of each angular subdivision is $\Delta\phi = 2\pi/N$, and we take the centre of the emission region at each step to be $\phi(i) = (i)(\Delta\phi)$. Figure 4.1 shows the relevant quantities.

We obtain the fluxes $F(i)$ by performing the following steps at each period step i:

1. Calculate the impact parameters of the null rays arriving at the observer from $\phi_- = \phi(i) - (\Delta\phi)/2$, $\phi(i)$, and $\phi_+ = \phi(i) + (\Delta\phi)/2$. Denote these impact parameters by b_-, b, and b_+. This is done by numerically solving Equation 4.6.

2. Calculate the redshift $z(b)$ using Equation 4.10.

3. Calculate the angular contribution to the flux integral, $\mathrm{d}\varepsilon$, using Equation 4.11.

4. Calculate the arrival time $t_o(i)$ of the flux by evaluating Equation 4.7 for impact parameter b, and putting $t_o(i) = \phi(i)/\Omega_\star + T(b)$.

5. Assign to $F(i)$ the value of the flux integral

$$F_{(1-\mathrm{D})} = \int_{(1+z)\nu_{o_{\mathrm{low}}}}^{(1+z)\nu_{o_{\mathrm{high}}}} \mathrm{d}\nu_e \int \mathrm{d}\varepsilon \, \frac{I_{\nu_e}(\alpha_e)}{(1-\Omega_\star b)(1+z(b))^4}, \tag{4.16}$$

   where $\nu_{o_{\mathrm{low}}}$ and $\nu_{o_{\mathrm{high}}}$ correspond to the lower and upper limits of the detector's energy band. In the particular case we are considering, we can leave out the integral over energies (we integrate over all energies $h\nu_o$ for bolometric flux), and disregard the dependence of I on α_e since we are considering isotropic radiation. Also note, again, that this integral is a non-standard definition of flux which we are adopting because we are dealing with a special one-dimensional emission region, as discussed in Section 4.3.5. The observer only receives photons from within the equatorial plane (the sky is effectively one-dimensional), so the integral is over a one-dimensional angle, not the usual solid angle for a two-dimensional sky.

Once the calculation for each step is completed, the stored values $F(i)$ and $t_o(i)$ are used to construct the function $F(t_o)$ at equally spaced intervals of t_o via a standard interpolation method. This step is necessary to facilitate fitting in the next section,

as the statistic that the fits rely on require comparing values at equal values of t_o. Also note that the **rns** code calculates the Exact metric potentials to a finite value of $\bar{r}$, and so our calculation is performed at distance $r \approx 10^{10}$ cm and not at infinity, however we have used expressions which account for locating the observer at finite $\bar{r}$ in our code. Also, for $M = 1.4\,M_\odot$, at this distance $2GM/(c^2 r) \approx 2 \times 10^{-5}$ so that the spacetime is close to flat.

For the purpose of illustration in Section 4.3.7, it will also be interesting to perform this calculation without time-of-flight effects included. To do this, the only change that needs to be made is to take $T(b) = 0$ at every i in the above calculation.

1-D version of Schwarzschild calculation without times-of-flight

We had a special code at hand to calculate the Schwarzschild light curves without times of flight included, although in principle an adaptation of the above method could also have been used. Instead, we adapted Equation 2.137 for our one-dimensional emission region. In practise this means that instead of the area element on the image plane given by Equation 2.128, i.e., $\mathrm{d}S_o = b\,\mathrm{d}b\,\mathrm{d}\phi_o$, we use the appropriate length element $\mathrm{d}\ell = \mathrm{d}b$. Using a similar argument as that leading to Equation 2.137, we obtain the following special expression specialised to the Schwarzschild metric for bolometric flux from a one-dimensional emitting region:

$$F_{1-\mathrm{D,\,Schw.,\,bol.}}(t_o) = \frac{1}{D}\frac{I_e}{(1+z)^4}\frac{1}{\mathrm{d}\psi/\mathrm{d}b}\frac{(\Delta\phi'_e)/\Gamma}{1-\Omega_\star b} \tag{4.17}$$

$$= \left(\frac{I_e(1-2M/R)^2(\Delta\phi'_e)}{\Gamma^5 D}\right)\frac{1}{(1-\Omega_\star b)^5\mathrm{d}\psi/\mathrm{d}b}, \tag{4.18}$$

where the term in parentheses is a constant that can be taken out of the calculation since we are only considering the shape of the pulse profile and not the value of the received flux. In this calculation, the evaluation of the light curve proceeds in a similar manner as above, except that we need only solve Equation 4.6 for b given $\phi(i)$ (eliminating the need to solve this equation for ϕ_- and ϕ_+ as well), and then evaluate the integral given by Equation 2.134 for $\mathrm{d}\psi/\mathrm{d}b$. Also, since we are not including the times-of-flight we need only take $t_o = \phi(i)/\Omega_\star$; the integral for $T(b)$ given in Equation 4.7 does not need to be calculated, and the final steps above to interpolate the $F(i)$ and $t_o(i)$ to values that are regularly-spaced in t_o does not need to be carried out since this calculation already has this property.

4.3.7 Light curve calculations

We are now able to discuss the properties of light curves calculated using the method that we have set out in this section. In Figure 4.4, we show the curves calculated using the Exact method with times-of-flight included for EOS A and L, for the 300 Hz and 600 Hz cases. First, note that the more compact EOS A models have a shorter eclipse than the EOS L models, as one would expect: the effect of "light bending" is greater for the more compact model. Also, the length of the eclipse expressed as a fraction of the period does not change a great deal as the speed of the models is increased; this is because the compactness decreases only by about 2% in the EOS A case as the star is spun up. In the EOS L case, the 600 Hz model is approaching breakup speed and the change is greater: about 10% between the 300 Hz and 600 Hz model. The other notable feature of these calculations is that as frequency (or speed) is increased, the pulse profiles become more asymmetric. So there is an indication that speed at the equator tends to equate to greater asymmetry in the pulse profile.

The main purpose of this section is to understand the effect of leaving out the time-of-flight in these calculations. In Figure 4.5, we have given a series of three plots corresponding to a $\Omega_\star$ =50 Hz, 300 Hz, and 600 Hz model calculated using EOS L for a $1.4\,M_\odot$ star. Each plot shows two light curves: one is computed in a manner that flux arriving from further away is binned relatively later than light arriving from closer points (i.e., we put $t_o = \phi(i)/\Omega_\star + T(b)$ as described in Section 4.3.6), the other light curve is calculated by binning flux only by rotational phase of the star, but retaining the required Doppler factor to account for magnification or reduction of the emitting region due to its motion (i.e., we only discard the $T(b)$ term in calculating t_o). As the light-crossing time of the star becomes a larger fraction of the rotation period, the distortion introduced by discarding the time-of-flight increases, and is noticable at the 300 Hz and 600 Hz levels covering the range of frequencies occupied by millisecond pulsars.

Another important observation from Figure 4.5 is that the plots which have the time-of-flight included tend to be more asymmetric than those that do not. This observation together with what we noted above about Figure 4.4 suggests the following: if one were to set about interpreting an observed pulse profile to extract M and R for a real millisecond-period source by referring only to sample calculations that did not include the photon travel times, one would tend to pick models with larger speeds at the equator in order to capture the greater asymmetry that is present in the data. Since the frequency of source would be fixed by the

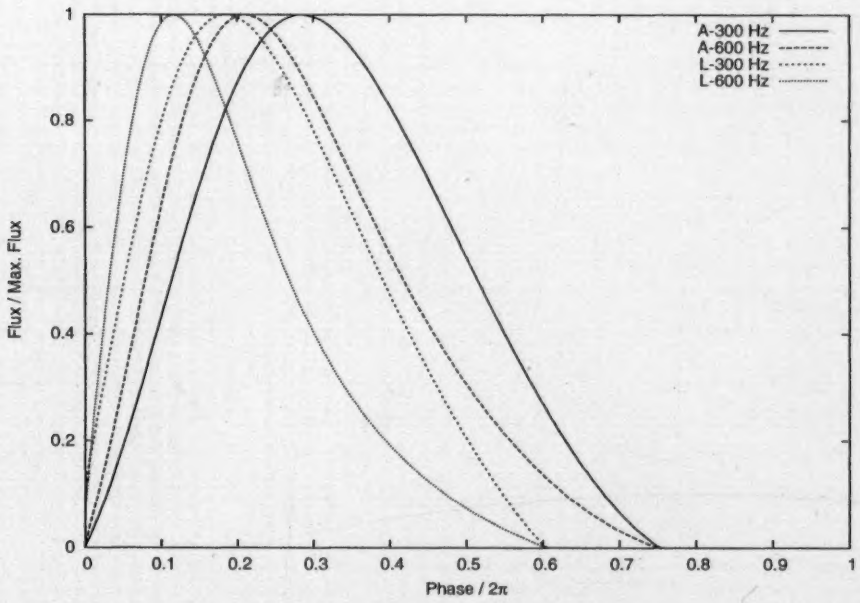

Figure 4.4: Light curves for 1-D emitting region: This figure shows the light curve produced by a 1-D emitting region located and observed in the equatorial plane for the 300 Hz and 600 Hz models for both EOS A and L, as listed in Table 4.1. The light curves are calculated using the exact metric, with all time-of-flight effects accounted for.

data, the only available mechanism to increase the speed is by increasing R. The length of the eclipse would also be fixed by the data, which fixes the value of M/R; thus a corresponding increase in M would be required. In sum, it seems reasonable to assume that this method of extracting M and R would tend to systematically over-estimate both M and R, but keep the value of M/R close to the true value. The remainder of this section tests this hypothesis.

4.3.8 Fit results

To determine the degree to which neglecting times-of-flight might (maximally) impact an analysis of real millisecond pulsar data, we attempted to fit the Exact method light curves shown in Figure 4.4 to curves calculated using the SS method without times-of-flight included. To accomplish this, we first calculated a number of approximate light curves over a range of values of M and R. If true(i) represents discrete values of the exact light curve calculation at observed phase $i(\Delta\phi)$, for $\Delta\phi = 2\pi/N$, and $0 \leq i \leq N-1$; and approx(i) is similarly the discretised values of the light curve obtained using the approximate calculation we are considering, then the best fit values of M and R—to the extent that they are unique—are taken to be the ones which achieve the minimum

$$\text{S.Sq.}/N = \frac{1}{N} \min_{M,R} \min_{0 \leq k \leq N-1} \left[\sum_{i=0}^{N-1} (\text{true}(i) - \text{approx}((i+k) \bmod N))^2 \right]. \qquad (4.19)$$

The minimisation over k is necessary since a constant phase shift of the approximate light curve relative to the true one should not influence the results of the fitting. The resulting fitted parameters are shown in Table 4.2. It is helpful to see the sense in which the result of this calculation produces a "fit" to the data: Figure 4.6 shows plots of the true light curve together with the best fit approximate light curve for the EOS A models. Similarly, Figure 4.7 shows this for the EOS L models. Our hypothesis is partially borne out by the results of this experiment: in 3 of the 4 cases, both M and R were over-estimated by 30–40%, while the error on M/R was constrained to less than 8%. The results for the EOS L, 600 Hz model do not follow from the simple argument we set out earlier: this case resulted in the poorest fit (measured via S.Sq./N), and overestimated R by 20%, but *underestimated* M by 12%. Of the four cases considered, this is the case where the introduction of the times-of-flight has the largest effect, since this is the largest model used (so with the longest-light crossing time), and the shortest period considered (so the times-of-flight represent the largest fraction of one period). What appears to happen is that

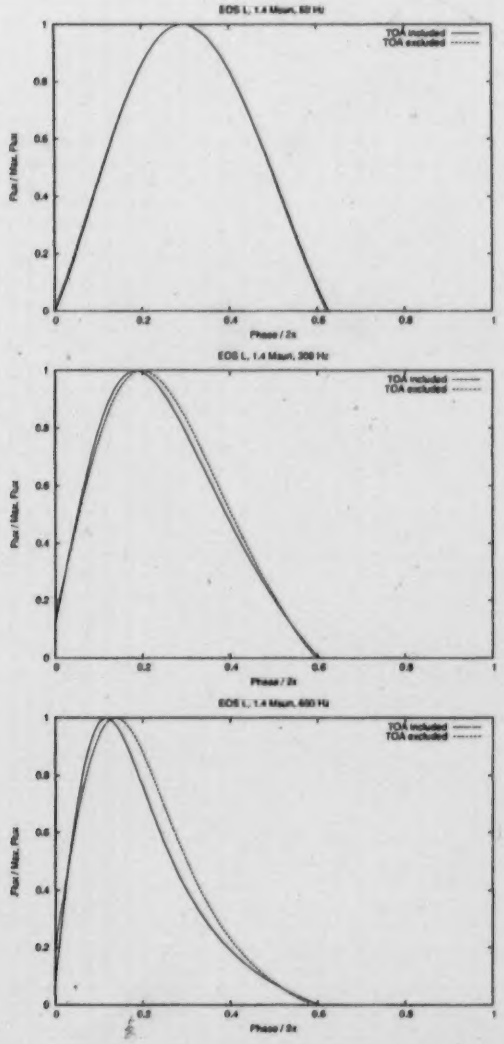

Figure 4.5: Distortion introduced by not including all time-of-flight effects: Each plot in this series shows two light curves: one is computed with photon travel time accounted for, the other is not. A 1.4 $M_\odot$, EOS L model was used to produce these plots; from top to bottom the frequencies used are 50 Hz, 300 Hz, and 600 Hz.

EOS	$\Omega_*/2\pi$ (Hz)	R (km)	Err.	M ($M_\odot$)	Err.	$GM/(c^2R)$	Err.	S.Sq./N ($\times 10^{-4}$)[a]
A	300	13.3	+38.3%	2.0	+42.9%	0.22	+3.3%	0.4
	600	12.5	+27.8%	1.8	+28.6%	0.21	+0.6%	2.6
L	300	19.4	+28.4%	1.94	+38.6%	0.15	+7.9%	0.8
	600	19.8	+20.9%	1.2	−14.3%	0.09	−29.1%	4.9

[a] The sum of squared differences between fitted approximate calculation and exact calculation, divided by the number of phase bins in the exact pulse shape. ($N = 180$ for all fits).

Table 4.2: Results of fits to exact 1-D light curves via an approximate calculation which does not include time-of-flight. See remark in text about possible degeneracy or non-uniqueness of fit results.

it is not possible to obtain a close fit to the data using the approximate method, and the fitting procedure preferentially attempts to fit the rise of the pulse as closely as possible which required a decrease in compactness and a corresponding shortening of the eclipse. The errors in the fit are moved to the portion of the pulse as the emitting region moves out of view. It is worth noting here that this fitting procedure has the undesireable property that good fits in the sense of small values of S.Sq./N do not imply good performance in estimating M and R individually: the worst fit has the smallest relative errors in these parameters. A similar statement applies to the resulting fitted value of M/R: the errors on the obtained value of M/R do not appear to be linked in a straightforward way to the quality of fit.

It is also necessary to discuss an apparent operational difficulty in obtaining these fits which foreshadows a well-known difficulty which is discussed in greater detail in Section 4.4.2 for the general case of the two-dimensional emitting region. In Figure 4.8 we have plotted contours of the S.Sq./N value for the EOS L, 300 Hz case, as a function of the M and R values of the candidate fitted models. In this plot, there are clearly two separate minima corresponding to different sets of parameters which result in approximately the same quality of fit: one is at $M = 1.94\,M_\odot$, $R = 19.4$ km; the other at $M = 1.74\,M_\odot$, $R = 18.4$ km. Both of these results have the same quality to within 1 part in 10^3 of S.Sq./N, and although the best of these is tabulated in Table 4.2 it would be incorrect to say that there is a single well-defined best-fitting model. While this is the only case that exhibited a distinct double minimum in this statistic, all of the cases we examined show a long, flat valley in these contours. One might expect this feature since, as has been pointed out, the best-fit models will tend to be those constrained to a narrow range of M/R. This example shows that there is a degree of degeneracy in obtaining fits

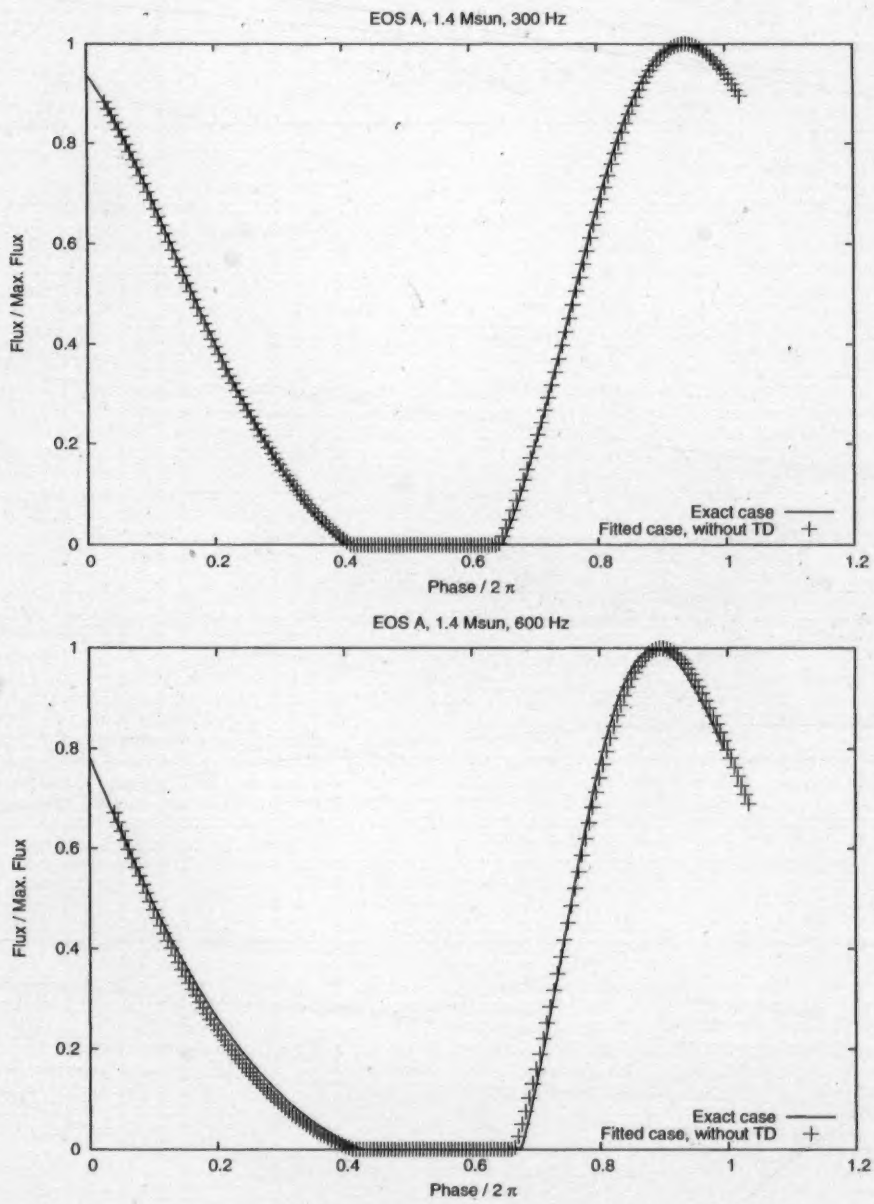
EOS A, 1.4 Msun, 300 Hz
Flux / Max. Flux
Phase / 2 π
Exact case
Fitted case, without TD
EOS A, 1.4 Msun, 600 Hz
Flux / Max. Flux
Phase / 2 π
Exact case
Fitted case, without TD

Figure 4.6: Fitted 1-D light curves for EOS A models: The best fit approximate light curves from Table 4.2 are plotted against the exact 1-D calculation.

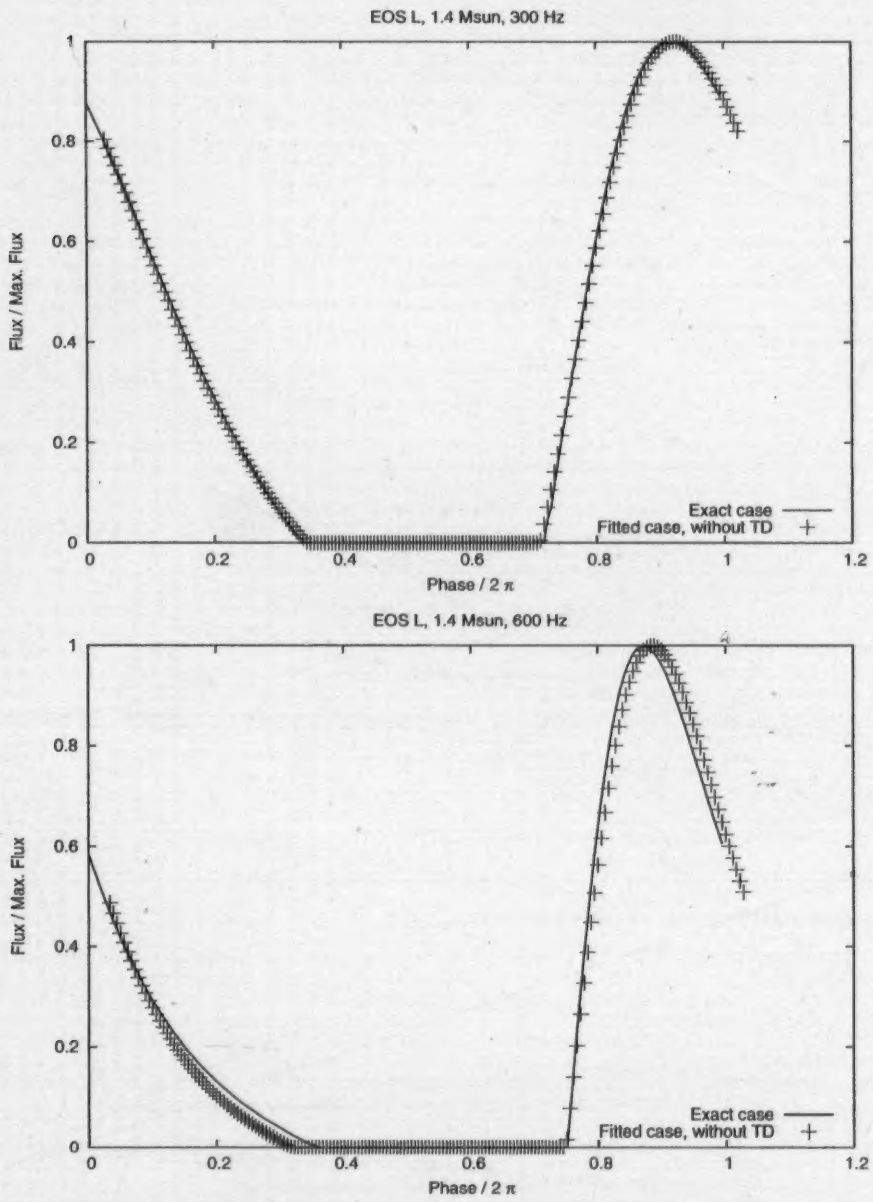
EOS L, 1.4 Msun, 300 Hz
Flux / Max. Flux
Phase / 2 π
Exact case
Fitted case, without TD
EOS L, 1.4 Msun, 600 Hz
Flux / Max. Flux
Phase / 2 π
Exact case
Fitted case, without TD

Figure 4.7: Fitted 1-D light curves for EOS L models: The best fit approximate light curves from Table 4.2 are plotted against the exact 1-D calculation.

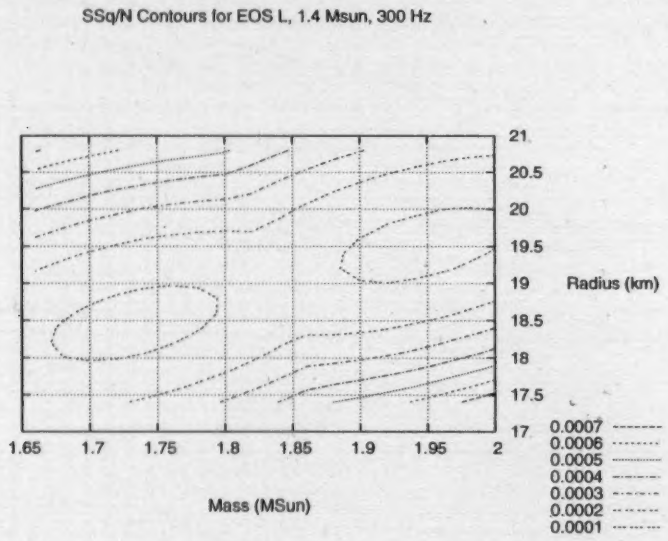

Figure 4.8: Contours of sum of squared differences for fit: Contours of the "S.Sq. / N" value for the EOS L, 300 Hz case are shown. In this plot there are clearly two separate minima corresponding to different sets of parameters with approximately the same quality-of-fit.

even in this simplified case.

Erratum in Cadeau *et al.* (2005)

This section is based on an idea pursued in Cadeau *et al.* (2005), except that in the results presented here a subtle change has been made in calculation of the Exact light curves and the fit results have been recalculated. The result is that the net size of the effect has changed, although the essence of the result has not. In Cadeau *et al.* (2005), the Exact light curves were calculated using a series of instantaneous flashes from the surface of the star, which were then composed together to give the "true" light curve. By doing this, however, the snapshot effect was removed from the true values, whilst it was included in the approximate light curves which were used for fitting. This is because the snapshot effect arises because of continuous-time emission from a moving object, measured at an instant of observer time. Instantaneous emission from a moving extended region, on the other hand, deposits energy over a range of observer times. The basic approach in Cadeau *et al.* (2005)

was to bin the flux arriving at the observer from instantaneous flashes, when it would have been more correct to bin flux arriving at the observer for emission over a range of times Δt_e; this would numerically capture the snapshot effect and no additional change would need to be made to the basic idea in Cadeau *et al.* (2005). In this section, we have discarded the flux-binning method described in Cadeau *et al.* (2005) in favor of correcting the subtended angle $d\varepsilon$ by the required factor, which is derived in Section 2.4.2.

Cadeau *et al.* (2005) states that the maximal error arising from using a fitting program which does not incorporate time-of-flight effects is "approximately $\pm 10\%$"; the results shown in Table 4.2 indicate that the resulting systematic error is much higher than that.

4.3.9 Conclusion

In this section we have set out a simplification of the full problem of calculating the light curve which relies on restricting both the emitter and observer to the equatorial plane, and furthermore adopting a non-standard definition of flux in order to suit this restriction. Many, but not all, analyses of millisecond pulsar data and related phenomena have not accounted for the differences in photon travel time as an emitting region moves with a rapidly-rotating neutron star. Furthermore, it is common to use the Schwarzschild metric as the framework in which to calculate deflection angles for photons reaching the observer. Within the simplified context of this section, we have calculated light curves using the exact metric and accounting for time-of-flight effects, and attempted to fit them by a least-squares method using light curves calculated using the Schwarzschild metric without time-of-flight effects included. We found that to capture the additional asymmetry in the pulse profile introduced by the time-of-flight effects, significant errors in the obtained best-fit parameters were introduced at the level of up to about 40% in M and R in isolation, and up to about 12% in M/R in the worst case. Furthermore, a degree of degeneracy in picking the "best fit" models was noted.

Since there is no difficulty in evaluating the times-of-flight, the efforts to fit millisecond-period pulsed light from accreting X-ray binaries with model light curves to infer neutron star parameters ought to include these effects, in view of the potentially considerable systematic error that would otherwise be introduced as a result.

4.4 The applicability of other approximate techniques[2]

In Section 4.3 we have provided a demonstration that it is important to account for the varying times-of-flight in the calculation of the light curve for rapid rotation, and in this section these effects are always included. This section is concerned with the approximations described in Section 3.1.1 to the general light curve calculation set out in Chapters 2 and 3. In particular, we described a number of possible approximations to the calculation of the light curve, which amount to a selection of metric (precise solution, Kerr, or Schwarzschild), and the manner by which the oblateness of the stellar surface is accounted for ("oblate," where the surface $\bar{r}_s(\theta)$ is specified via the structure calculation; or "spherical", i.e. constant $\bar{r}$ (for SK), or constant Schwarzschild $r = \exp[(\gamma - \rho)/2]\bar{r}_s(\pi/2)$ (for SS)). The "Exact" method represents the first calculation of light curves using a precise solution of the spacetime metric and stellar structure, and the remaining methods are various approximations that may be conceived of and are analogous to other calculations found in the literature. For example, Muno *et al.* (2002b) use a method similar to our "SS" method in their studies of the amplitude evolution and harmonic content of X-ray burst oscillations (they included times-of-flight in their models). Bhattacharyya *et al.* (2005) use the Kerr metric and a spherical stellar surface star to obtain light curves which they used to model the burst oscillations of the X-ray pulsar XTE J1814-338; this is similar to what we refer to as the "SK approximation". In their calculation, Bhattacharyya *et al.* (2005) make use of a structure calculation to obtain the angular momentum, mass, and radii of their stellar models given an EOS, which allows them to fix the Kerr parameter a in their calculations, similar to what we did to calculate Table 4.1. However, they "do not include the effects of spin-induced stellar oblateness," which they argue are small since the oblateness is second order in $\Omega_\star$. One of the goals of this section is to test this assertion. Finally, Braje *et al.* (2000) use a Monte Carlo method to obtain a calculation similar to our SK calculation, and in Braje and Romani (2001) they undertook a comparison of a light curve model for either oblate or spherical stellar surfaces. We have also made it possible to marry our light curve calculations to a precise solution of the stellar structure, by incorporating the oblateness of rapidly-rotating neutron star models, as expressed by $\bar{r}_s(\theta)$: the coordinate location of the star's surface as a function of colatitude. Knowing this makes it possible to pick correct initial conditions for the integration of null geodesics, as discussed

[2]Some of the results appearing in this section are contained in Cadeau *et al.* (2006), and portions of the paper are incorporated here.

in Section 2.3.2.

This section is arranged as follows: First, we attempt to quantify the differences between the five different methods we are contemplating in Section 4.4.1. Then, in Section 4.4.2 we present a study where we calculated light curves using the Exact method, then then obtained fits to them by varying the input parameters of the SS calculation so as to minimise the χ^2 between the Exact and SS methods.

4.4.1 Methods comparison

To begin with, one expects that all reasonable methods of calculating the light curve should converge as the spin is reduced. To illustrate this, in Figure 4.9 we have computed the light curve for an EOS L, $1.4\,M_\odot$ model for emission from $\theta_e = 41°$, and observation at $\theta_o = 100°$ spinning at $\Omega_\star = 200$ Hz, 400 Hz, and 600 Hz, using the Exact calculation as well as the approximations OK, OS, SK, and SS. As $\Omega_\star$ increases, it is apparent that the calculations which account for oblateness in some fashion (i.e., Exact, OK, OS) depart from the ones that do not (i.e., SK, SS), but that for the slowest speed shown there is little difference. It is clear that of the models we are considering from Table 4.1, that the 600 Hz EOS L case will be the most oblate. The simplest way of seeing this is classically: this model has the largest radius and angular velocity, and so the effect due to centrifugal force on the surface is greatest. This model is quite close to the breakup speed, or mass-shedding limit, when the rotating fluid elements at the surface are no longer gravitationally bound to the star (or, in the relativity language, they have no four-acceleration). In this case, $\bar{r}_s(0)/\bar{r}_s(\pi/2) = 0.827$, compared to the 600 Hz EOS A case where the same ratio is 0.96. Since we are concerned with the worst-case of effects due to oblateness for realistic models, we will limit what follows to considering the 600 Hz EOS L case; this is relaxed again in Section 4.4.2.

To illustrate the distortions that appear in the calculated light curves when oblateness is incorporated, we have chosen two cases where there are significant differences in the light curve calculated by the methods with an oblateness description compared with the "spherical" methods. In Figure 4.10, we have plotted the light curve obtained using all of the methods we are considering for: emission from $\theta_e = 15°$, and observation at $\theta_o = 100°$ in the top panel, and $\theta_e = 45°$, $\theta_o = 135°$ in the bottom panel. In the top panel, the clear difference is that the oblate calculations do not eclipse, while the spherical ones do. In the bottom panel the situation is reversed: the oblate calculations eclipse for longer than do the spherical calculations. Clearly these differences might have significant implications for

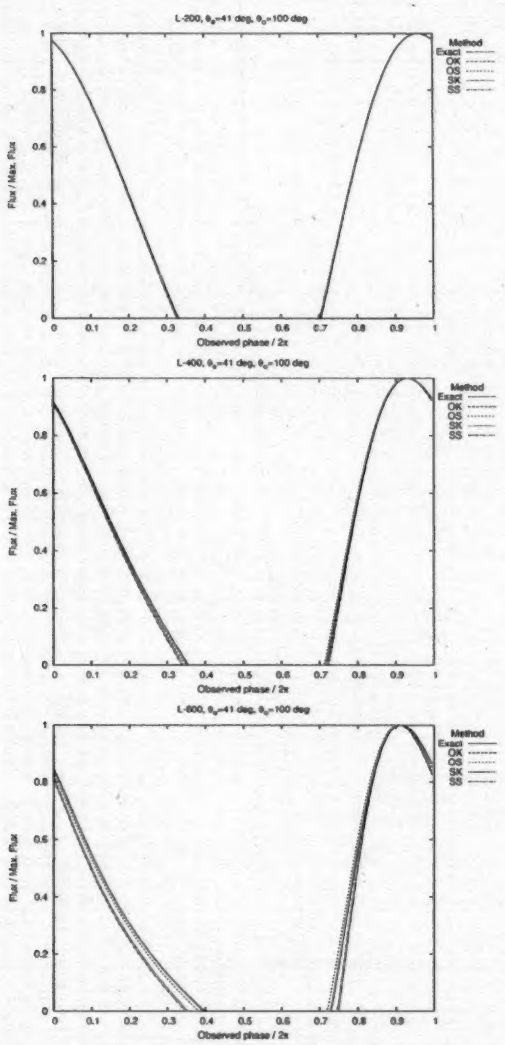

Figure 4.9: Oblateness becomes important as Ω_* increases: In this series of light curves, we vary the speed of the model and leave the other parameters fixed. The top panel is the slowest (200 Hz), and the bottom is the fastest (600 Hz). Note that as speed increases, the calculated pulse profile increasingly depends on the particular method used.

data analysis: fitting routines are based on minimisation of χ^2 will tend to match eclipse durations or pulsed fractions of data with those features predicted by a theoretical light curve model. As Figure 4.10 illustrates, these features as calculated in the "spherical" approximations are not reliable approximations of the situation for the Exact method, or other approximate methods with an oblateness description built-in.

To understand the genesis of this distortion, we consider the $\theta_e = 15°$, $\theta_o = 100°$ case more carefully. In Figure 4.11, we show two panels corresponding to the Exact method (top) and the SS method (bottom), where we have plotted as a function of rotation phase two quantities: first, a parameter which corresponds to $\dot{\theta}_i$ for the rays reaching the observer using cross symbols against the left-hand axis, and second, a parameter corresponding to $\dot{\tilde{r}}_i$ using a line against the right-hand axis. Note that the plotted parameters are actually rescalings of these values used by the code such that the sign and relative sizes of these values are maintained—only the relative sizes and signs matter for the discussion at hand. When $\dot{\theta}_i$ is negative, the ray initially heads "north" in angular coordinates. Comparing the values of the $\dot{\tilde{r}}_i$ parameter in the Exact (top) panel where there is no eclipse, and SS (bottom) panel where the emission region is eclipsed (the eclipse occurs at those points where the cross symbols are absent compared to the top panel), we see that the value of $\dot{\tilde{r}}_i$ becomes negative in the Exact case, which allows additional rays to reach the observer during those phases for which the emission region is eclipsed in the SS calculation. The eclipse is introduced in the SS calculation because $\dot{\tilde{r}}_i \geq 0$ when the star is taken to be spherical, but north-directed rays from the upper hemisphere can have negative values of $\dot{\tilde{r}}_i$ when the star's oblateness is accounted for. An illustration of this is given in Figure 4.12. The bottom panel of Figure 4.10, where the SS calculation is visible for longer than in the Exact calculation, can be explained in a similar way: in this case, the rays reaching the observer are south-directed from the upper hemisphere, and in the exact case the $\dot{\tilde{r}}_i$ values must remain above a positive critical value determined by the oblateness, while in the SS calculation they can reach zero. In the sense of Figure 2.1, the top panel of Figure 4.10 involves a case where some rays reaching the observer in the exact calculation are in Region I, which is prohibited in the SS calculation. The bottom panel involves a case where rays reaching the observer in the SS calculation are in Region IV, which is prohibited in the Exact calculation.

Naturally, one is led to wonder how the approximate methods we have considered fare as θ_e, θ_o are varied. To investigate this, we calculated the Exact, SS, and

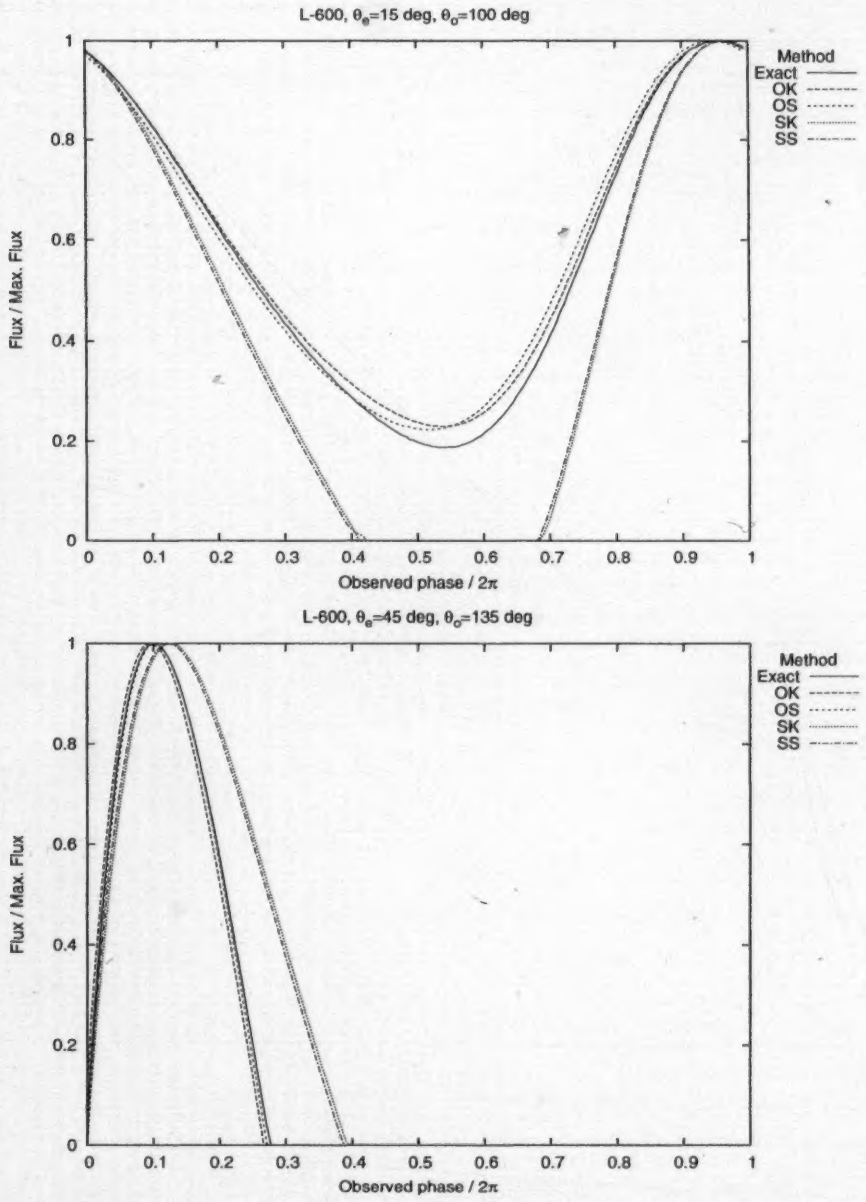

Figure 4.10: Qualitative changes in lightcurves when oblateness is accounted for: These plots show light curves calculated for EOS L, $1.4\,M_\odot$, $\Omega_\star = 600$ Hz. The top panel shows the case where emission is from $\theta_e = 15°$, and observation takes place at $\theta_o = 100°$; the bottom panel is for $\theta_e = 45°$, $\theta_o = 135°$.

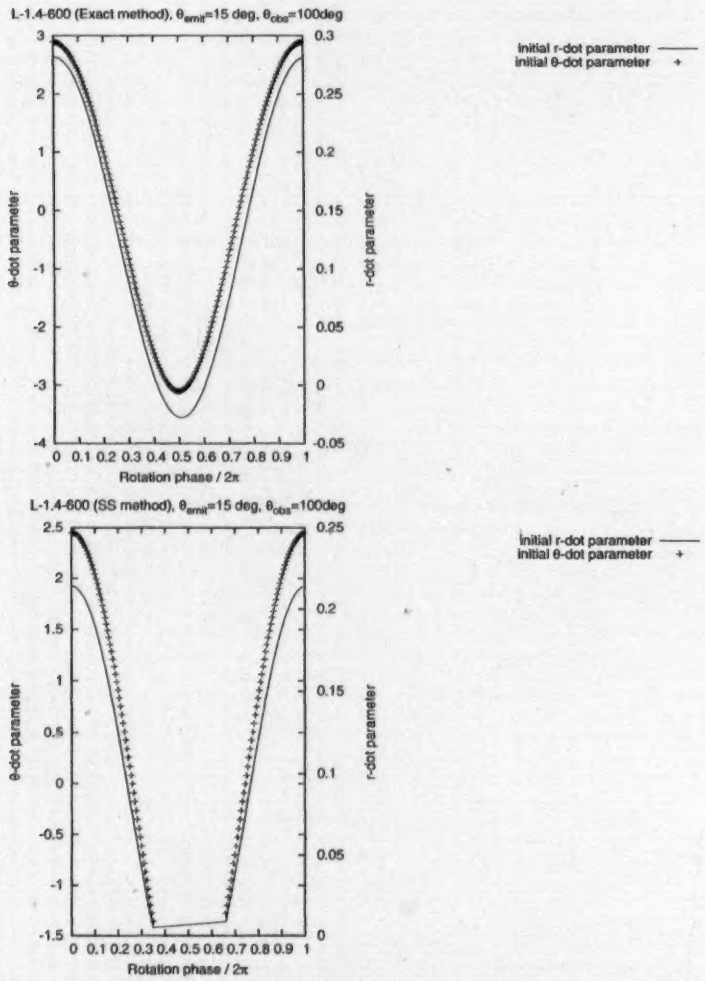

Figure 4.11: Different rays can reach the observer in oblate calculation ($\theta_e = 15°$, $\theta_o = 100°$): This figure corresponds to the top panel of Figure 4.10. On these two panels, we have plotted a parameter which corresponds to $\dot{\theta}_i$ for the rays reaching the observer using cross symbols against the left-hand axis, and a parameter corresponding to $\dot{r}_i$ using a line against the right-hand axis, as a function of rotation phase (the plotted parameters are rescalings of these values used in the code such that the sign and relative sizes of these values are maintained).

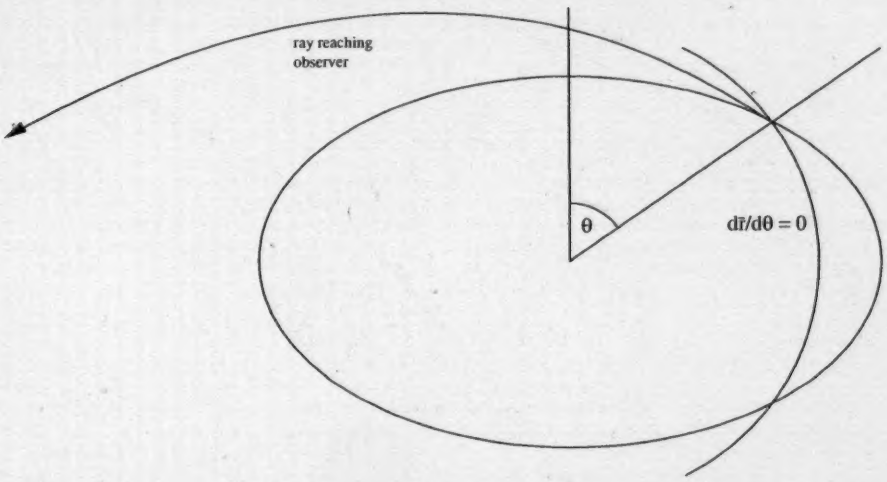

Figure 4.12: Exact method allows for rays with $\dot{\bar{r}}_i < 0$, but in the SS calculation these rays would be prohibited, leading to an eclipse as in the top panel of Figure 4.10.

OK light curves for a range of angles, and then computed the S.Sq./N statistic, defined in Equation 4.19. The results are shown in Figure 4.13 where we have plotted contours of S.Sq./N as a function of the two angular parameters for the SS calculation (top panel) and OK calculation (bottom panel). Both plots show a steep peak in S.Sq./N for calculation with light coming from near the spin axis and observed by highly-inclined observers, which is the worst-performing case. The peak size of the statistic is about two orders of magnitude smaller for the OK calculation than the SS calculation, indicating that in the worst case, the disagreement between the OK and Exact calculation is about 1/10 the disagreement between the SS and Exact methods, on average. Also, these contour plots indicate that the agreement between methods is best for light emitted and observed near the equatorial plane. This makes sense as at the equator there is no effect due to oblateness, because all methods agree on a description of the stellar radius (whether isotropic or areal) at the emission region, and there are no additional or prohibited rays that are introduced since at the equator $\mathrm{d}\bar{r}/\mathrm{d}\theta = 0$. As a further illustration, in Figure 4.14, we have shown calculations corresponding to the worst case (top panel, $\theta_e = 15°$, $\theta_o = 90°$), and the best case (bottom panel, $\theta_e = 90°$, $\theta_o = 90°$) scenarios that we have identified by this procedure.

In the best case, there is still a small effect due to the precision to which light-

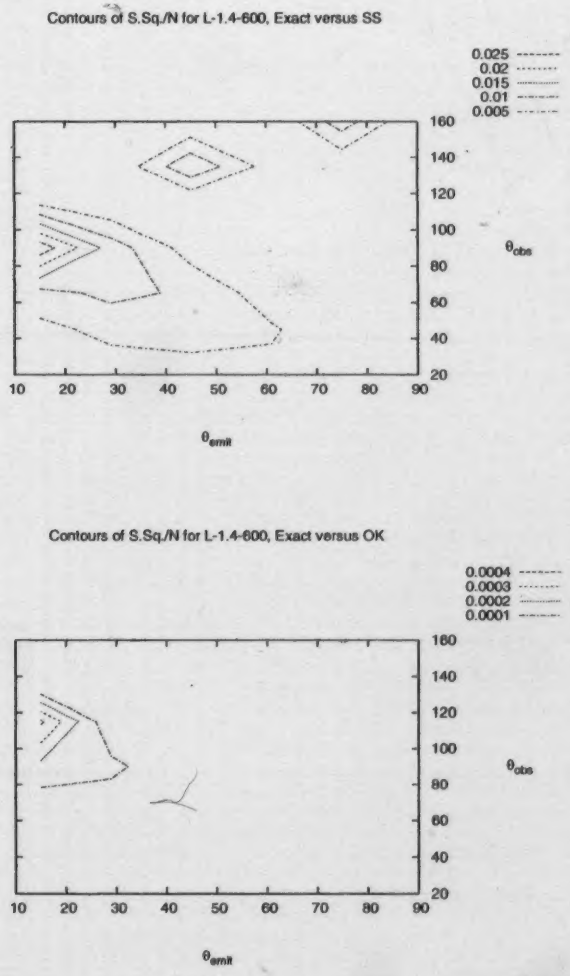

Figure 4.13: Determining the worst-case scenario for approximate calculation: In each panel, we have plotted contours of S.Sq./N, defined in Equation 4.19, as a function of θ_e and θ_o to compare the Exact calculation to the SS calculation (top panel), and to the OK calculation (bottom panel), using calculations for EOS L, $1.4\,M_\odot$, $\Omega_\star = 600$ Hz.

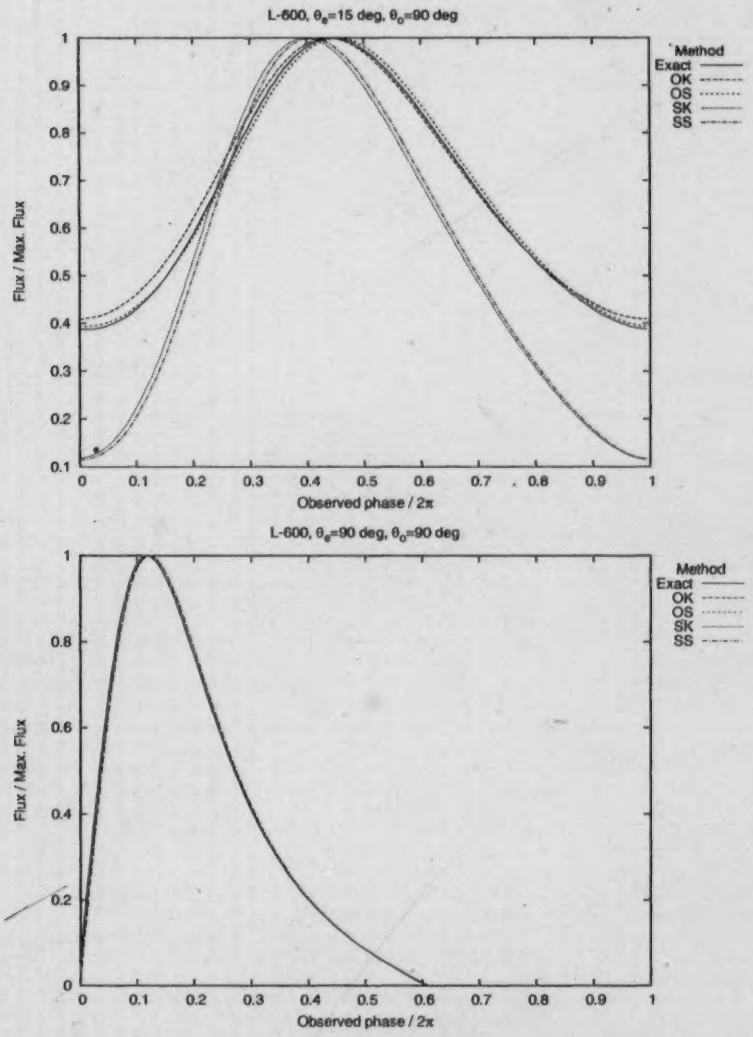

Figure 4.14: Example of worst- and best-case scenarios for approximate calculations: Following on from Figure 4.13, we have produced an examples of the "worst" (top) and "best" (bottom) cases for EOS L, 1.4 $M_\odot$, $\Omega_\star = 600$ Hz. In the top panel, computed for $\theta_e = 15°$, $\theta_o = 90°$, there is significant discrepancy between the calculations which account for oblateness (Exact, OK, OS), and the ones that do not (SK, SS). On the other hand, the bottom panel shows the $\theta_e = 90°$, $\theta_o = 90°$ case, where all calculation methods essentially coincide.

bending can be calculated using an approximate metric, but this is a much smaller effect than oblateness can introduce for general values of the angular parameters. This agrees with what Braje and Romani (2001) found. Their work allowed for the possibility of a rotationally-flattened star in their studies of thermal emission from a single polar cap for both spherical and "elliptical" stars. They noted that the difference in the light curve calculation introduced by passing from the Schwarzschild to Kerr metric was smaller than other considerations that become important for rapid rotation, among them time delays (as we showed in Section 4.3), Doppler boosts, aberration, and oblateness. So it is somewhat surprising that there are no extant analyses of millisecond pulsar data which account for oblateness (Braje and Romani (2001) discusses a theoretical model without an application to data), but effort *has* been expended to improve the accuracy of photon propagation by incorporating the Kerr metric (for example, by Bhattacharyya *et al.* (2005)). Clearly the priority under circumstances similar to what we're considering—surface emission from a millisecond pulsar—should be to incorporate a good description of oblateness in these models.

Perhaps the reason for the absence of effort in analysis this way is understandable: the rotation-induced oblateness as measured by how $\bar{r}_S(\theta)$ differs from some fiducial value (e.g., $\bar{r}_S(\pi/2)$) is of order $\Omega_\star^2$, so one is tempted to assert that it is a small effect (Bhattacharyya *et al.*, 2005). This is absolutely correct from the point of view of those effects that rely on the size of $\bar{r}$ (or speed), for example, the rotation-induced part of redshift (i.e., Doppler boosting). However, there are two problems with this argument; first, $\bar{r}_S(0)/\bar{r}_S(\pi/2)$ is not coordinate invariant and is not directly observable. Second, it is really the derivative $\mathrm{d}\bar{r}_S(\theta)/\mathrm{d}\theta$ that bears the major responsibility for effects due to oblateness discussed here, as this controls the orientation of surface elements along the observer's line of sight. Introducing these effects which are not captured in the analogous "spherical" cases is primarily what causes the effects we have noted here, and are more significant than might be suggested by looking at the ellipticity of the surface. Beyond the temptation to dismiss these effects as "small," there is also the practical matter of producing a model that incorporates a sufficiently flexible model of oblateness while being fast enough for fitting. Braje and Romani (2001) calculated pulse shapes similar to our OS and OK calculations via a Monte Carlo method they devised, which is not at all similar to what is usually done for pulse shape models which are used for fitting, and is probably not suitable for such an application because of the computationally intensive nature of the Monte Carlo method. Methods based on the formalism of

Pechenick *et al.* (1983) can be adapted for oblateness, but not without significant complication. A first look is taken at this in Section 4.5.

4.4.2 Fits to obtain parameters

We have established that, all other things being equal, reasonable variations on the light curve calculation method can result in significant differences in the computed pulse profile. Furthermore, the magnitudes of these differences are sensitive to the emission region's and observer's inclination angles. In this section we would like to ask a different question: how well can one expect a χ^2 minimization program based on fitting to the SS calculation to perform for millisecond-period pulsars? In other words, if we compute the observed bolometric pulse profile for an infinitesimal emitting region using the Exact method for some stellar model and choice of inclination angles, will we reliably recover the relevant parameters by minimising the χ^2 to SS calculations with all but the frequency left undetermined? This is an important question because if the SS fitting technique performs acceptably well, then no, or perhaps only minor work will need to be done to adapt the extant fitting codes for rapid-rotation. On the other hand, if it does not perform well, then it will indicate a general need to replace tools based on SS (or SK) calculations to incorporate oblateness. The restriction to infinitesimal and isotropic emission regions allows us to isolate the effect just due to oblateness, and tests the robustness of the fitting procedure when slightly different descriptions of the photon orbits are used.

To carry through this study, we first computed light curves using the Exact method for a number of $1.4\,M_\odot$ stellar models from Table 4.1, for a number of choices of emission and observer inclinations angles. Then fits were obtained to these light curves using a program which minimises χ^2 against the SS calculation (Leahy, 2005). The true values for the cases considered are displayed in Table 4.3, where we show the Schwarzschild radius as a function of emission inclination angle, $R(\theta_e)$, for all of the considered cases, as well as $GM/(c^2R(\theta_e))$, since the results of the fit are for the value of R and $GM/(c^2R)$ at the emitting region and not on the equator.

The results of the fits are shown in Tables 4.4 and 4.5. The fits were obtained by first fixing the value of $GM/(c^2R)$ at the emission region; this means that all evaluations of the angular deflection integral are for a single value of $GM/(c^2R)$, which makes it easy to numerically solve for impact parameters b given a required angular deflection. Then the program attempts to find the global minimum in χ^2,

θ_e	EOS	Ω_* (Hz)	$R(\theta_e)$ (km)	$GM/(c^2R(\theta_e))$
15°	A	100	9.57	0.216
		300	9.55	0.217
		400	9.53	0.217
		500	9.51	0.217
		600	9.49	0.218
	L	300	14.63	0.141
		400	14.47	0.143
		500	14.25	0.145
		600	13.98	0.148
41°	A	100	9.57	0.216
		300	9.58	0.216
		400	9.58	0.216
		500	9.59	0.216
		600	9.60	0.215
	L	300	14.82	0.140
		400	14.80	0.140
		500	14.78	0.140
		600	14.74	0.140
45°	A	100	9.57	0.216
		200	9.58	0.216
		300	9.58	0.216
		400	9.59	0.216
		500	9.61	0.215
		600	9.63	0.215
	L	100	14.83	0.139
		200	14.84	0.139
		300	14.85	0.139
		400	14.87	0.139
		500	14.89	0.139
		600	14.90	0.139
85°	A	100	9.57	0.216
		200	9.59	0.216
		300	9.62	0.215
		400	9.66	0.214
		500	9.71	0.213
		600	9.78	0.211
	L	100	14.86	0.139
		200	14.95	0.138
		300	15.10	0.137
		400	15.35	0.135
		500	15.73	0.131
		600	16.35	0.127

Table 4.3: The true values of $R(\theta_e)$, $GM/(c^2R(\theta_e))$ are displayed for the fitted light curves; the results of the fits are displayed in Tables 4.4 and 4.5.

defined by

$$\chi^2 = \sum_{i=0}^{N-1} \left(\frac{\text{true}(i) - \text{fit}(i)}{\sigma} \right)^2, \tag{4.20}$$

by varying R, θ_e and θ_o. M is obtained from the assumed value of $GM/(c^2R)$ and the fitted value of the radius. We have taken a constant value $\sigma = 0.01$ to be the "error" on the true values, which will allow us to establish confidence intervals on the obtained fits. The minimisation of χ^2 is achieved by an application of the conjugate gradient method described by Press *et al.* (1988) (Leahy, 2005). This is much faster than doing an evaluation everywhere in the parameter space, but has the side-effect that it is sometimes sensitive to the initial values of the parameters at the beginning of the minimisation process. By carrying out this process for a number of values of $GM/(c^2R)$, we select the result with the lowest minimum χ^2. We have also calculated the 90% uncertainty in the value of $GM/(c^2R)$, which for one parameter of interest is found by interpolating for the values of $GM/(c^2R)$ with $\chi^2 = \chi^2_{\text{best}} + 2.71$ (Leahy, 2005). In several cases, the minimum in χ^2 is so shallow that no meaningful error bars can be computed and these cases are marked with an asterisk in the relevant column. These fits are degenerate in the sense that almost any reasonable value of $GM/(c^2R)$ can correspond to a good fit. The difficulty in obtaining unique fits was foreshadowed in Section 4.3.8, and it is relatively well-known that fitting in this way sometimes has non-unique solutions. Bhattacharyya *et al.* (2005) pointed out that it is the presence of significant power in the higher harmonics of the data that allows for this kind of analysis to take place, because such power is necessary for significant asymmetry in the pulse profile. One of the cases suffering from degeneracy is $\theta_e = 15°$, $\theta_o = 100°$; considering the top panel of Figure 4.14 (actually computed for $\theta_o = 90°$), it is clear that for this set of angles that the light curve does not have significant power in higher harmonics, and as a result it is easy to fit a large number of different models to it. In related work, Muno *et al.* (2002b) remark on a degeneracy in fits containing our two inclination angles and a parameter controlling the emission region size in their fits to the amplitudes of thermonuclear X-ray bursts. Also, the possibility of degeneracies in fitting light curves of isolated X-ray dim neutron stars to their models was raised by Zane and Turolla (2005).

Considering the non-degenerate fit results, first we note that χ^2 tends to increase with frequency, indicating that at higher speeds the best fit SS models fit the Exact calculation more poorly than for slower models. Examining the best fit values of $GM/(c^2R(\theta_e))$, we see that with two exceptions, the true values were generally

within the established error bar, and the errors on the fitted values were constrained to about 11%, often much less. The exceptional cases were also the most extreme tests of this method, corresponding to the EOS L, 600 Hz model for $\theta_e = 45°$, $\theta_o = 135°$ and for $\theta_e = 41°$, $\theta_o = 100°$, where the true values fell outside the error bar and large errors in the fitted values were noted.

Considering the fits to values of M and R individually, we see that for the slower 100 Hz and 200 Hz cases, that the errors on these quantities are generally confined to less than 10%. An exception is the approximately 20% errors noted for the EOS A, 200 Hz case for $\theta_e = 45°$, $\theta_o = 135°$, which may indicate a possible degeneracy problem for this case, since we know that the Exact and SS light curves nearly coincide in this limit. For the faster models, the errors on these fitted values can reach the 20% level in several different cases. Finally, considering the fits to the angular parameters, we found that there were significant difficulties establishing the true angles for nearly all of the $\theta_e = 41°$, $\theta_o = 100°$ cases (signalling a possible degeneracy issue), as well as for the single non-degenerate $\theta_e = 85°$, $\theta_o = 20°$ case, with errors at the level of a few tens of degrees. The $\theta_e = 45°$, $\theta_o = 135°$ results were quite good with errors almost uniformly at the level of a few degrees. Finally, the $\theta_e = 85°$, $\theta_o = 100°$ results were reliable for the slower models, with the errors tending to increase with speed above 200 Hz.

It is also interesting to see an illustration that the fitted models do, indeed, describe the data. Figure 4.15 shows two plots illustrating the differences between light curves obtained via the SS calculation using both fitted and true values for the parameters, compared to the Exact calculation. The top panel is for the EOS L, $\Omega_\star = 300\,\mathrm{Hz}$, $\theta_e = 85°$, $\theta_o = 100°$ case in Table 4.5. We see that although the best fit case over-estimated both mass and radius by about 20% over the true values, there is no appreciable difference between the three light curves. In this case the true value of $GM/(c^2R)$ falls within the error bar given on the fit. The bottom panel is for the EOS L, $\Omega_\star = 600\,\mathrm{Hz}$, $\theta_e = 41°$, $\theta_o = 100°$ case: this fit underestimated mass by 7% and underestimated radius by 12%, and the fitted value of $GM/(c^2R)$ was too high by 14%. In this case, the fitting program shortened the eclipse to better fit the data by tending to a larger value of $GM/(c^2R)$; note that the SS calculation produced using the true values has an eclipse that is too short.

4.4.3 Conclusion

In this section, we first undertook a comparison of the Exact light curve calculation method we set out in Chapters 2 and 3, with the approximations we described in

θ_e	θ_o	EOS	Ω_* (Hz)	$M/M_\odot$		$R(\theta_e)$ (km)		θ_e (deg)		θ_o (deg)		$GM/c^2R(\theta_e)$			χ^2
				fit	rel. err.	fit	rel. err.	fit	abs. err.	fit	abs. err.	fit	unc.	rel. err.	
15°	20°	A	100	1.40	-0.002	10.3	0.08	14.2	-0.8	19.9	-0.1	0.2	*	-0.07	0.002
		A	300	1.40	-7×10^{-5}	9.85	0.03	14.3	-0.7	19.9	-0.1	0.21	*	-0.03	0.01
		L		1.40	-0.002	16.5	0.1	13.0	-2.0	20.1	0.1	0.125	*	-0.1	0.01
		A	400	1.40	-4×10^{-4}	10.3	0.08	13.9	-1.1	19.4	-0.6	0.2	*	-0.08	0.03
		L		1.39	-0.004	17.9	0.2	12.3	-2.7	19.1	-0.9	0.115	*	-0.2	0.03
		A	500	1.40	0.002	10.9	0.2	13.4	-1.6	18.9	-1.1	0.19	*	-0.1	0.04
		L		1.39	-0.008	19.5	0.4	11.6	-3.4	18.1	-1.9	0.105	*	-0.3	0.03
		A	600	1.40	0.003	11.5	0.2	12.9	-2.1	18.4	-1.6	0.18	*	-0.2	0.04
		L		1.41	0.009	19.0	0.4	11.5	-3.5	17.8	-2.2	0.11	*	-0.3	0.1
15°	100°	A	100	1.08	-0.2	6.35	-0.3	30.1	15.1	80.9	-19.1	0.25	*	0.2	4
		A	500	0.593	-0.6	8.76	-0.08	54.7	39.7	21.8	-78.2	0.1	< 0.225	-0.5	1
		L		0.854	-0.4	8.41	-0.4	30.2	15.2	78.1	-21.9	0.15	< 0.2	0.03	0.8
		A	600	0.678	-0.5	9.10	-0.04	56.9	41.9	20.3	-79.7	0.11	*	-0.5	0.8
		L		0.918	-0.3	7.98	-0.4	34.1	19.1	69.5	-30.5	0.17	*	0.1	2
41°	20°	A	100	1.41	0.004	9.23	-0.04	29.8	-11.2	28.9	8.9	0.225	*	0.04	0.005
		A	500	1.40	0.002	10.4	0.08	20.6	-20.4	35.3	15.3	0.2	*	-0.07	0.05
		L		1.99	0.4	16.8	0.1	33.2	-7.8	21.5	1.5	0.175	*	0.3	0.03
		A	600	1.40	0.001	10.9	0.1	20.2	-20.8	34.0	14.0	0.19	*	-0.1	0.07
		L		2.53	0.8	17.8	0.2	28.8	-12.2	23.2	3.2	0.21	*	0.5	0.06
41°	100°	A	100	1.48	0.06	10.2	0.06	80.5	39.5	139.2	39.2	0.215	0.011	-0.005	0.1
		A	300	1.49	0.06	10.0	0.04	79.8	38.8	138.0	38.0	0.220	0.005	0.02	1
		L		1.09	-0.2	11.1	-0.3	67.0	26.0	95.6	-4.4	0.145	0.024	0.04	0.3
		A	400	1.45	0.04	9.55	-0.004	80.8	39.8	134.9	34.9	0.225	0.006	0.04	2
		L		1.17	-0.2	11.9	-0.2	58.0	17.0	96.3	-3.7	0.145	0.023	0.04	0.4
		A	500	1.51	0.08	9.89	0.03	80.2	39.2	136.9	36.9	0.225	0.005	0.04	3
		L		1.29	-0.08	12.7	-0.1	52.7	11.7	98.1	-1.9	0.15	0.02	0.07	0.8
		A	600	1.58	0.1	10.2	0.06	41.9	0.9	102.2	2.2	0.230	0.007	0.07	4
		L		1.30	-0.07	12.0	-0.2	57.9	16.9	97.5	-2.5	0.160	0.015	0.1	2

Table 4.4: Fits to light curves using SS method to extract parameters, part 1: For the tabulated cases, the best fit Schwarzschild calculation (corresponding to our SS method with general M and R) to our light curves calculated using the Exact method were obtained by Leahy (2005) to assess the impact of using this approximation in this context. Where the uncertainty value of GM/c^2R is given as *, this indicates that the best fit was degenerate in this parameter. Table 4.3 displays the true values of $R(\theta_e)$ and $GM/(c^2R(\theta_e))$. All models have true mass $1.4\,M_\odot$. This table is continued in Table 4.5

θ_e	θ_o	EOS	Ω_* (Hz)	$M/M_\odot$		$R(\theta_e)$ (km)		θ_e (deg)		θ_o (deg)		$GM/c^2R(\theta_e)$			χ^2
				fit	rel. err.	fit	rel. err.	fit	abs. err.	fit	abs. err.	fit	unc.	rel. err.	
45°	135°	A	100	1.51	0.08	10.4	0.08	47.4	2.4	137.8	2.8	0.216	0.005	-0.003	0.1
		L		1.46	0.04	15.4	0.04	44.8	-0.2	135.4	0.4	0.140	< 0.155	0.004	0.06
		A	200	1.60	0.1	10.9	0.1	45.5	0.5	138.5	3.5	0.218	0.004	0.007	1
		L		1.48	0.06	15.7	0.06	44.3	-0.7	136.0	1.0	0.140	< 0.145	0.005	0.1
		A	300	1.57	0.1	10.7	0.1	45.1	0.1	137.6	2.6	0.217	0.006	0.003	0.5
		L		1.45	0.04	15.9	0.07	44.0	-1.0	136.0	1.0	0.135	< 0.155	-0.03	0.1
		A	400	1.73	0.2	11.6	0.2	41.6	-3.4	139.0	4.0	0.220	0.005	0.02	8
		L		1.44	0.03	16.3	0.1	43.0	-2.0	136.4	1.4	0.130	< 0.145	-0.07	0.1
		A	500	1.61	0.1	11.0	0.1	44.5	-0.5	138.6	3.6	0.216	0.005	0.001	1
		L		1.22	-0.1	18.0	0.2	32.0	-13.0	123.4	-11.6	0.100	< 0.135	-0.3	0.8
		A	600	1.63	0.2	11.2	0.2	42.5	-2.5	137.7	2.7	0.215	0.005	-0.002	1
		L		1.34	-0.04	18.0	0.2	40.0	-5.0	137.5	2.5	0.110	< 0.145	-0.2	0.6
85°	20°	A	100	0.665	-0.5	9.82	0.03	27.1	-57.9	47.9	27.9	0.1	*	-0.5	0.5
		A	500	0.701	-0.5	10.4	0.07	24.0	-61.0	52.9	32.9	0.1	< 0.23	-0.5	0.6
		L		0.999	-0.3	12.8	-0.2	27.7	-57.3	69.7	49.7	0.115	< 0.2	-0.1	2
		A	600	0.752	-0.5	10.1	0.03	53.1	-31.9	25.0	5.0	0.11	$> 0.1, < 0.22$	-0.5	0.8
		L		1.27	-0.1	13.4	-0.2	26.6	-58.4	75.1	55.1	0.14	0.04	0.1	1
85°	100°	A	100	1.48	0.06	10.4	0.09	87.4	2.4	110.8	10.8	0.210	0.008	-0.03	1
		L		1.45	0.04	15.3	0.03	84.0	-1.0	103.7	3.7	0.140	0.027	0.006	0.05
		A	200	1.46	0.05	10.1	0.05	84.4	-0.6	103.9	3.9	0.215	0.006	-0.003	2
		L		1.43	0.02	15.6	0.05	86.7	1.7	107.6	7.6	0.135	0.029	-0.02	0.4
		A	300	1.48	0.06	10.2	0.06	83.1	-1.9	103.5	3.5	0.215	0.025	6×10^{-7}	4
		L		1.70	0.2	17.9	0.2	80.0	-5.0	123.3	23.3	0.140	0.015	0.02	0.4
		A	400	1.49	0.07	10.3	0.06	77.2	-7.8	99.7	-0.3	0.215	0.003	0.004	7
		L		1.40	0.003	16.0	0.04	85.0	0.0	105.5	5.5	0.130	0.009	-0.04	4
		A	500	1.68	0.2	11.3	0.2	67.7	-17.3	111.0	11.0	0.220	0.004	0.03	5
		L		1.51	0.08	17.9	0.1	61.7	-23.3	97.7	-2.3	0.125	0.009	-0.05	6
		A	600	1.62	0.2	11.1	0.1	72.5	-12.5	113.6	13.6	0.215	0.003	0.02	1×10^1
		L		1.40	0.002	17.3	0.06	77.8	-7.2	102.6	2.6	0.120	0.007	-0.05	2×10^1

Table 4.5: Fits to light curves using SS method to extract parameters, part 2: This is the continuation of Table 4.4.

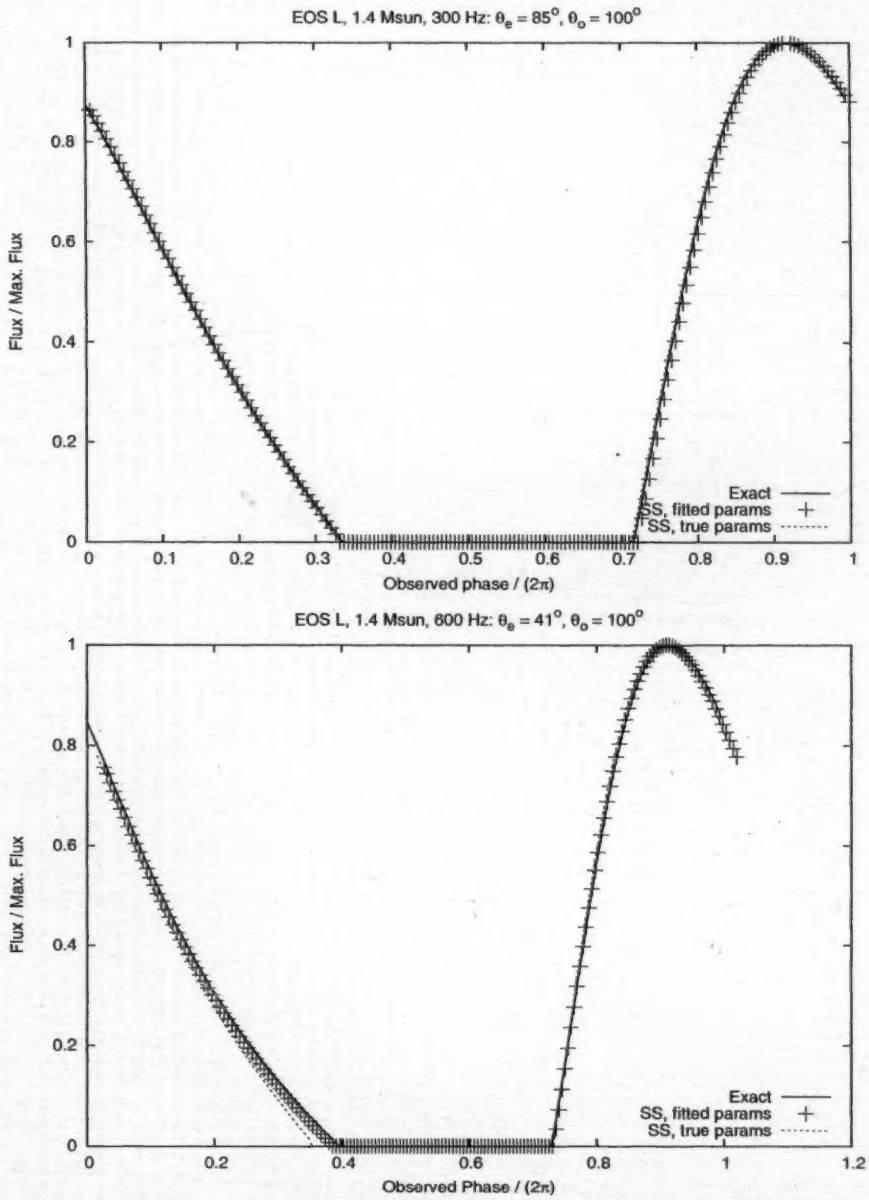
EOS L, 1.4 Msun, 300 Hz: θe = 85°, θo = 100°
Flux / Max. Flux
Observed phase / (2π)
Exact
SS, fitted params
SS, true params
EOS L, 1.4 Msun, 600 Hz: θe = 41°, θo = 100°
Flux / Max. Flux
Observed Phase / (2π)
Exact
SS, fitted params
SS, true params

Figure 4.15: Comparing light curves with fitted parameters to true values: These two plots illustrate the differences between light curves obtained via the SS calculation using both fitted and true values for the parameters, compared to the Exact calculation.

Section 3.1.1: namely, the oblate Kerr and Schwarzschild (OK, OS) methods, and the "spherical" Kerr and Schwarzschild (SK, SS) methods. We found that while there was little difference introduced by using the Kerr metric for photon propagation over the Schwarzschild metric, significant differences could be introduced by describing the stellar surface as oblate instead of spherical. These finding are consistent with what was suggested by Braje and Romani (2001). Furthermore, the differences between the Exact calculation and both of these approximations were maximised in the case when light was emitted from close to the rotation axis, and observed close to the equatorial plane. The maximum disagreement between the OK and Exact methods were on the average 10% of the size of the disagreement between the SS and Exact methods.

Using our Exact calculation as a source of synthetic data for the observed bolometric pulse profile of an infinitesimal isotropic emission region, we then attempted to extract the corresponding parameters by minimising χ^2 against light curves calculated using the SS method. We found that several of the cases studied suffered from degeneracy in the fits, in the sense that there was no unique way to map the pulse profile to parameters. This is expected in cases where there is not significant power present in the higher harmonics of the pulse. For the non-degenerate cases, our results tended to indicate that it is generally possible to get a good estimate of $GM/(c^2R(\theta_e))$ by fits to the SS calculation, for all but the most extremely deformed stars (i.e., the stiff EOS L model at 600 Hz). Modulo some cases that are likely to have suffered from a degeneracy, however, this method is much less reliable in establishing the M and R parameters individually for frequencies higher than about 200 Hz, when the errors on these fitted parameters taken alone can be as high as about $\pm 20\%$, which is not small enough to place interesting constraints on neutron star parameters. The poor performance of this fitting procedure for higher frequencies is likely to be a result of the increasing significance of oblateness. It seems reasonable that fitting to millisecond-period pulsar data is best done using theoretical models that account for oblateness in some fashion.

In the next section we go some distance to show how it is possible to avoid structure calculations in estimating the effect of oblateness for a certain family of equations of state, and we do preliminary work to show that in principle it is possible to modify simple pulse profile calculation codes to capture the qualitative effects of oblateness.

4.5 Modelling oblateness: Model of Schwarzschild radius

Setting the initial conditions for integration of null rays requires knowing the location of the surface, $\bar{r}_s(\theta)$, and this is obtained from the structure calculation from which we also obtain the values of the metric potentials and their derivatives. Considering the apparent usefulness of the OK and OS approximations to the calculation of the flux, we have developed a simple model for the oblateness of rapidly-rotating neutron stars which may be suitable for applications where it is not desireable to compute the structure of a model star, or one wishes to consider models which do not necessarily derive from a known equation of state.

We have heretofore considered oblateness in terms of the coordinate $\bar{r}$ at the surface given the colatitude θ, $\bar{r}_s(\theta)$. To make the model as convenient as possible to use, we remove the potential necessity of having to translate between the quasi-isotropic $\bar{r}$ coordinate and the regular areal (Schwarzschild) r coordinate by considering the value of the r coordinate at the surface as a function of $\mu \equiv \cos\theta$, $r_s(\mu) = \exp[(\gamma - \rho)/2]\bar{r}_s(\theta)$. Then we consider the expansion

$$r_s(\mu) = \sum_{n=0}^{\infty} \tilde{a}_{2n} P_{2n}(\mu). \tag{4.21}$$

In this expansion, $\tilde{a}_{2n}$ has units of length; we consider an expansion in terms of the dimensionless quantity

$$a_{2n} \equiv \frac{\tilde{a}_{2n}}{R}, \tag{4.22}$$

where $R \equiv r_s(0)$. Given a model integrated by the RNS computer code for some EOS, M and $\Omega_\star$, the corresponding $\tilde{a}_{2n}$ values can be calculated via the relation

$$\tilde{a}_{2n} = \frac{4n+1}{2} \int_{-1}^{1} r(\mu) P_{2n}(\mu) \mathrm{d}\mu, \tag{4.23}$$

and the corresponding a_{2n} values are calculated via the definition in Equation 4.22. To accomplish this integration we make use of the `AdaptiveSimpson` and `LegendreP` methods included with the Matpack C++ Numerics and Graphics Library (Gammel, 2005). Given a means of calculating the a_{2n} values for a particular model, we can also attempt to approximate them by regarding them *only* as functions of the dimensionless quantity

$$x \equiv \Omega_\star^2 R^3/(GM); \tag{4.24}$$

$2n$	s_{2n}	t_{2n}	u_{2n}
0	-0.074 ± 0.011	-0.1495 ± 0.0033	1.00003 ± 0.00013
2	-0.001 ± 0.022	-0.3152 ± 0.0063	0.00015 ± 0.00024
4	0.1578 ± 0.0030	-0.01622 ± 0.00089	$(6.1 \pm 3.4) \times 10^{-5}$

Table 4.6: Using a set of 60 stellar models, we have obtained quadratic fits to the coefficients a_{2n} which describe the stellar oblateness. We have fitted the quadratic polynomial $f_{2n}(x)$, with x defined by Equation 4.24, to the data a_{2n} so that $a_{2n} \approx f_{2n}(x)$.

that is, we're seeking functions f_{2n} such that

$$f_{2n}(x) \approx a_{2n}. \tag{4.25}$$

To accomplish this, we calculated the a_{2n} coefficients for the 60 models such that EOS $\in \{\mathrm{A}, \mathrm{APR}, \mathrm{L}\}$, $M/M_\odot \in \{1.4, 1.6, 1.8, 2.0\}$, and $\Omega_\star \in \{100, 200, 300, 400, 600\}$ Hz. Such a set consists of models spanning a reasonable range of compactness, frequency, and mass. With the exact a_{2n} in hand for these 60 models, we used the `fit` routine in the Gnuplot Plotting Utility (Williams and Kelley, 2004) to fit the data points to the quadratic polynomials

$$f_{2n}(x) = s_{2n}x^2 + t_{2n}x + u_{2n}. \tag{4.26}$$

The results of the fits for orders $n = 0 \ldots 2$ are tabulated in Table 4.6. By discarding the fitted coefficients which are approximately 0 within the standard error, we obtain the simplified model

$$f_0(x) = -0.074x^2 - 0.15x + 1 \tag{4.27}$$

$$f_2(x) = -0.315x \tag{4.28}$$

$$f_4(x) = 0.158x^2 - 0.0162x. \tag{4.29}$$

Figure 4.16 shows the a_{2n} data compared to the fitted polynomial models for the $f_{2n}(x)$.

To understand the level at which this model of oblateness applies, we can look at a plot of the next order terms, a_6, for each of these 60 models as a function of $\Omega_\star$ in Figure 4.17. As one expects, the truncation error in the expansion is higher as the frequency increases, but is at worst 0.3% of the equatorial radius. The polynomial models above describe the data well enough that we can take this

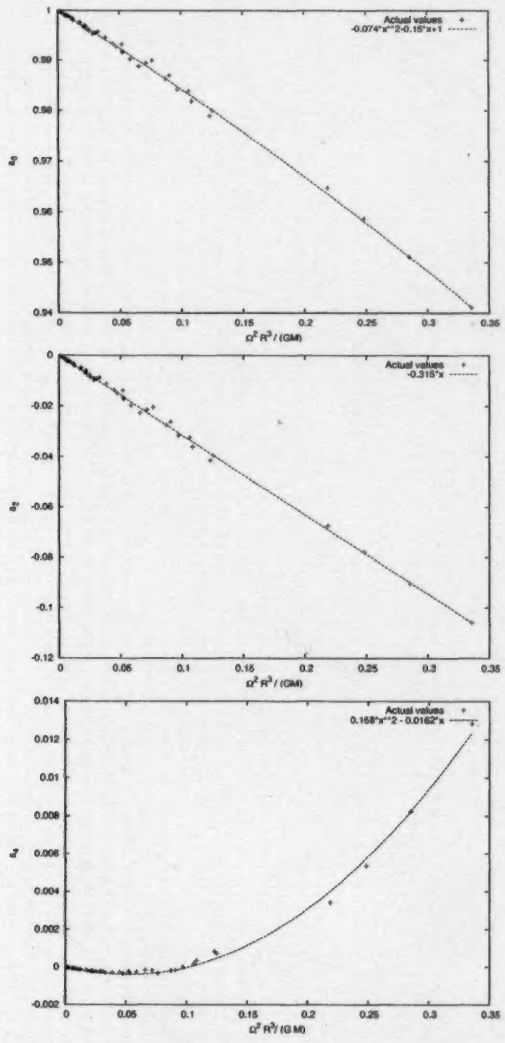

Figure 4.16: Quadratic polynomial models for oblateness coefficients a_{2n} for $n = 0 \ldots 2$: The top panel shows the a_0 data points compared to the fitted polynomial model $a_0 \approx f_0(x) = -0.074x^2 - 0.15x + 1$. The middle panel shows the a_2 data points compared to the fitted polynomial model $a_2 \approx f_2(x) = -0.315x$. The bottom panel shows the a_4 data points compared to the fitted polynomial nodel $a_4 \approx f_4(x) = 0.158x^2 - 0.0162x$.

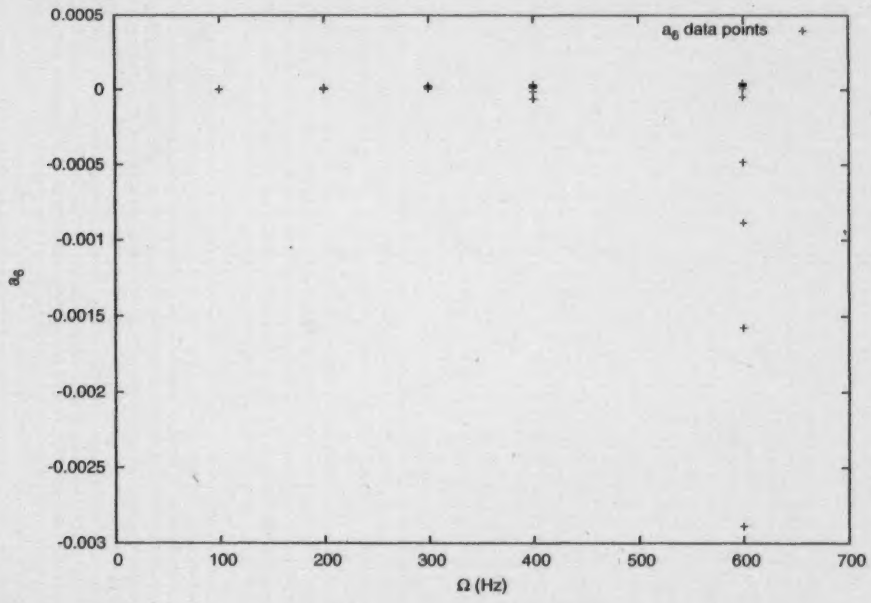

Figure 4.17: Leading truncation term in polynomal oblateness model: The a_6 coefficients of the 60 models we considered to develop the fitted polynomials to the lower-order terms are plotted versus $\Omega_\star$. Note that the absolute truncation error increases with frequency, but is at worst only 0.3% of the equatorial radius.

as an indicator of the worst accuracy of $r_s(\mu)$ obtained from the model compared to the true values. Figure 4.18 is a plot of $r_s(\mu)$ showing the worst-performing case for this model compared to the true values, and a level of error consistent with the truncation error is observed.

4.5.1 Adaptation of Schwarzschild light curve calculation to incorporate oblateness

In Section 3.5.2, it was observed that the light curve from the OS calculation was related to the light curve from the SS calculation by a factor of $\cos\alpha_{\text{obl.}}/\cos\alpha_{\text{sph.}}$, where α is the zenith angle as measured at the surface in the observer's frame, when r_i and r_f are equal. This can be understood as an observation that the projection of solid angle onto the observer's sky involves a factor of $\cos\alpha$ as measured at the surface; Poutanen and Gierliński (2003) make use of this observation in their calculation. Now that we have a numerical model for oblateness, it should be possible to incorporate this factor into the Schwarzschild formulation of the light

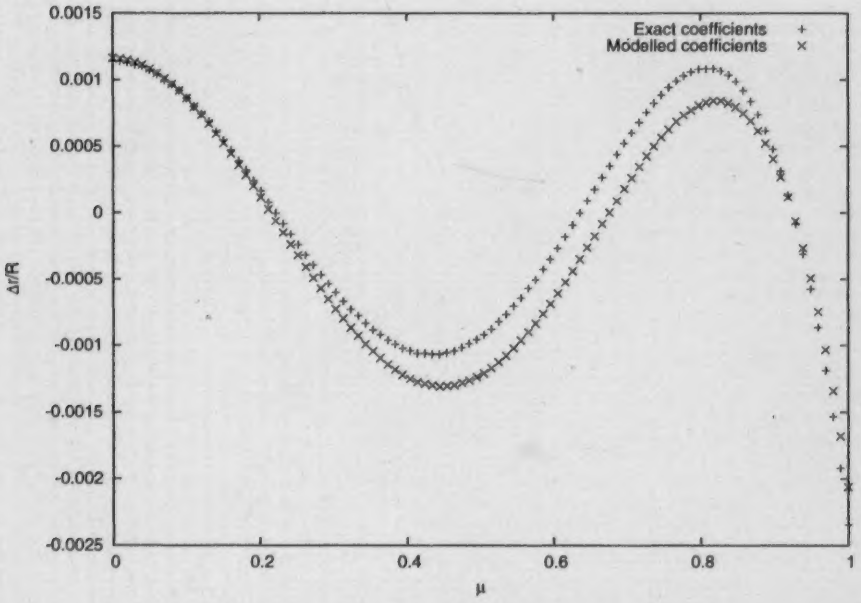

Figure 4.18: The oblateness of the EOS L, $1.4M_\odot$, 600 Hz model is most poorly described by the fitted polynomial model. In this plot $\Delta r_s(\mu)/R = (r_s(\mu)_{\rm true} - r_s(\mu)_{\rm series})/R$ is plotted versus μ using the series in Equation 4.21 truncated after the a_4 term using both the exact coefficients for this model ($a_0 = 0.9411$, $a_2 = -0.1058$, $a_4 = 0.01282$), and those obtained via the polynomial fits ($a_0 = 0.9413$, $a_2 = -0.1058$, $a_4 = 0.01237$). The worst error is about 0.24% of the equatorial radius of $R = 16.376$ km, which is consistent with the size of the next order term in the series.

curve calculation, given in Section 2.5. The main difficulty of doing this is that the numerical model of oblateness is set out in terms of the angle θ measured from the spin axis of the star, whereas the Schwarzschild formulation takes place in a coordinate system chosen so as always to maintain the origin, emission region, and observer in the same coordinate plane, $\theta' = \pi/2$. As we pointed out in Section 2.3.4, the calculation of the zenith angle involves an inner product between the normal of the surface and the initial four-momentum of the emitted light ray, and so to carry through this calculation we need to re-express the normal to the surface in terms of the coordinates used in the Schwarzschild formulation of the problem.

The transformation between coordinate systems is given by an appropriate composition of rotation matrices. In particular,

$$\begin{bmatrix} \sin\theta'\cos\phi' \\ \sin\theta'\sin\phi' \\ \cos\theta' \end{bmatrix} = \begin{bmatrix} 1 & 0 & 0 \\ 0 & \cos\sigma & -\sin\sigma \\ 0 & \sin\sigma & \cos\sigma \end{bmatrix} \begin{bmatrix} \cos\zeta & 0 & \sin\zeta \\ 0 & 1 & 0 \\ -\sin\zeta & 0 & \cos\zeta \end{bmatrix} \begin{bmatrix} \sin\theta\cos\phi \\ \sin\theta\sin\phi \\ \cos\theta \end{bmatrix}. \tag{4.30}$$

The parameters ζ and σ can be found by requiring that the observer, at $\theta = \theta_o$, $\phi = 0$, and the emission region, at $\theta = \theta_e$, $\phi = \phi_e$, be both located at $\theta' = \pi/2$ in the new coordinate system. The impact parameter b in the Schwarzschild formulation is related to the conserved ϕ' momentum. One obtains

$$\zeta = \pm\pi/2 - \theta_o \tag{4.31}$$

$$\tan\sigma = \frac{\pm\cos\theta_o\sin\theta_e\cos\phi_e \mp \sin\theta_o\cos\theta_e}{\sin\theta_e\sin\phi_e}. \tag{4.32}$$

To obtain the desired continuity, choose + above when $\phi_e \in [0, \pi]$, and − otherwise. The explicit transformation into the primed angular coordinates is

$$\begin{bmatrix} \sin\theta'\cos\phi' \\ \sin\theta'\sin\phi' \\ \cos\theta' \end{bmatrix} = \begin{bmatrix} \cos\zeta\sin\theta\cos\phi + \sin\zeta\cos\theta \\ \sin\zeta\sin\sigma\sin\theta\cos\phi + \cos\sigma\sin\theta\sin\phi - \cos\zeta\sin\sigma\cos\theta \\ -\sin\zeta\cos\sigma\sin\theta\cos\phi + \sin\sigma\sin\theta\sin\phi + \cos\zeta\cos\sigma\cos\theta \end{bmatrix} \tag{4.33}$$

If n^a is the normal to the surface as given by the numerical model, then the zenith angle in the observer's frame is obtained by evaluating

$$\cos\alpha = \frac{h_{ab}\ell^a n^b}{|\ell^a|_h |n^a|_h}, \tag{4.34}$$

at the surface, with $h_{ab} = g_{ab} + u_a u_b$ and $u_a = t_a/W$. This becomes

$$\cos\alpha = \frac{n^r\sqrt{1-(1-2M/r)b^2/r^2} + n^{\phi'}(1-2M/r)b}{((n^r)^2 + (1-2M/r)r^2(n^\theta)^2)^{1/2}}. \tag{4.35}$$

In the limit of a spherical star, n^θ and $n^{\phi'}$ tend toward zero and this equation reduces to the familiar

$$\sin\alpha = (1-2M/r)^{1/2}b/r. \tag{4.36}$$

Given the function $r_s(\theta)$, which is obtained from the oblateness model, we know that the components of the normal vector in the unprimed system are

$$n^r = 1, \tag{4.37}$$

$$n^\theta = -\frac{1}{r^2(1-2M/r)}\frac{\mathrm{d}r_s}{\mathrm{d}\theta}. \tag{4.38}$$

To evaluate $n^{\phi'}$, we use the transformation of vector components relation

$$n^{\gamma'} = n^\gamma \frac{\partial x^{\gamma'}}{\partial x^\gamma}. \tag{4.39}$$

In this situation, this means that

$$n^{\phi'} = n^\theta \frac{\partial \phi'}{\partial \theta}. \tag{4.40}$$

Using the explicit coordinate transformation from Equation 4.33, we have

$$\frac{\partial\phi'}{\partial\theta} = \csc^2\theta'(\sin\sigma\cos\phi + \sin\zeta\cos\sigma\sin\phi). \tag{4.41}$$

The only element that remains is to calculate $\mathrm{d}r_s/\mathrm{d}\theta$ in terms of the polynomial oblateness model. Our model is the series

$$r_s(\cos\theta) = R\sum_{n=0}^{2} f_{2n}(x)P_{2n}(\cos\theta), \tag{4.42}$$

where R is the equatorial radius of the star, and x defined via Equation 4.24. Then we have that

$$\frac{\mathrm{d}r_s}{\mathrm{d}\theta} = R\sin\theta\sum_{n=1}^{2} f_{2n}(x)P'_{2n}(\cos\theta). \tag{4.43}$$

At these low orders, it is easiest to directly work out the derivatives of the Legendre

polynomials

$$P_0(x) = 1 \tag{4.44}$$
$$P_2(x) = \frac{1}{2}(3x^2 - 1) \tag{4.45}$$
$$P_4(x) = \frac{1}{8}(35x^4 - 30x^2 + 3), \tag{4.46}$$

which are

$$P_0'(x) = 0 \tag{4.47}$$
$$P_2'(x) = 3x \tag{4.48}$$
$$P_4'(x) = \frac{x}{2}(35x^2 - 15). \tag{4.49}$$

At this stage, we have enough that a computer code based on the Schwarzschild formulation given in Section 2.5, such as the one used in the verification of the general code in Section 3.5.2, can be modified to account (to an extent) for rapid rotation by building in an oblateness term. This is done by including a correction factor of the form $\cos\alpha_{\text{obl.}}/\cos\alpha_{\text{sph.}}$ in the integral. This approach only works for those data described by rays visible in *both* the spherical and oblate cases. All we are seeking here is proof-of-concept for an application of the above oblateness model and zenith angle calculation, so this is satisfactory. The modified calculation proceeds by choosing an initial *equatorial* radius R, mass M, frequency $\Omega_\star$, and emission colatitude θ_e. Then $r(\theta_e)$ is calculated via the model; this is the initial radius for the $\psi(b)$ and $T(b)$ integrals, and the radius that enters into the relavent redshift and velocity factors. Finally, at every step of the calculation the factor $\cos\alpha_{\text{obl.}}/\cos\alpha_{\text{sph.}}$ is computed and multiplied with the flux calculated via the standard Schwarzschild formulation.

We have made this trivial modification to our computer code based on the Schwarzschild formulation of Section 2.5, and show in Figure 4.19 how the resulting light curve compares to a calculation done with our more general method. For the chosen parameters, introducing this correction factor makes the light curve track the Exact and OS calculations much more closely than the one produced by assuming a spherical surface. The key difference is that the simpler method has no knowledge of the initial structure beyond the oblateness model given above, and the mass, equatorial radius, and frequency of the exact model. The modified computer code takes only seconds to compute a light curve, compared to several hours for the exact calculation using the general code.

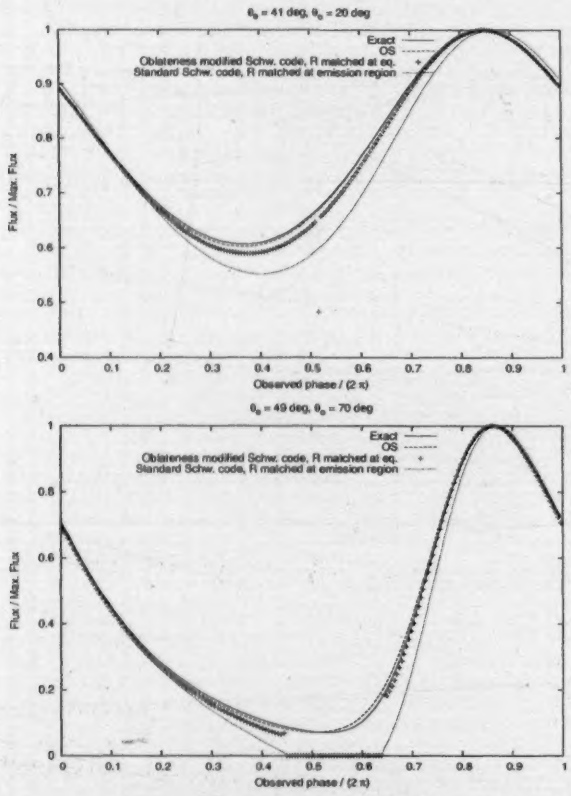
θe = 41 deg, θo = 20 deg
Exact
OS
Oblateness modified Schw. code, R matched at eq.
Standard Schw. code, R matched at emission region
Flux / Max. Flux
Observed phase / (2 π)
θe = 49 deg, θo = 70 deg
Exact
OS
Oblateness modified Schw. code, R matched at eq.
Standard Schw. code, R matched at emission region
Flux / Max. Flux
Observed phase / (2 π)

Figure 4.19: Incorporating oblateness model into calculations: We made a minor modification to our simple computer code based on the Schwarzschild formulation to incorporate a factor of $\cos\alpha_{\rm obl.}/\cos\alpha_{\rm sph.}$ to attempt to incorporate the effect of oblateness on the observed light curve. Both graphs were calculated for the EOS L, $1.4\,M_\odot$, 600 Hz model which is the most oblate model we are considering. Each graph shows the light curve as calculated by the general code running in the exact configuration (the "true" value) and in the OS configuration, the light curve calculated by the oblateness-modified code with the equatorial radius set to agree with the true model, and the light curve calculated by the spherical Schwarzschild code where the radius is set to agree with the true value at the emission region. The top graph is for emission at $\theta_e = 41°$ and observation at $\theta_o = 20°$; the bottom graph has $\theta_e = 49°$ and observation at $\theta_o = 70°$. The oblateness modified code cannot calculate the flux arising when the emission region is not visible, as there is nothing to apply the correction factor to. The improvement is significant enough that this idea should be further developed beyond this prototype.

Incorporating the oblateness model via a correction factor seems to improve the performance of codes based on the Schwarzschild formulation given in Section 2.5 which assume a spherical surface, but the formulation itself needs to be modified in order to account for the changed visible region when oblateness is included. Having given the required oblateness model and worked out the modification to the zenith angle when oblateness is included above, the remainder of the details on this point are left to future work.

Chapter 5

Conclusion

Summary

The discovery of millisecond-period X-ray pulsars within the last decade (Wijnands and van der Klis, 1998), and the related discovery of coherent oscillations in the cooling tails of Type I X-ray bursts (Strohmayer *et al.*, 1996), offers a tantalising opportunity to use these new observations to unravel the physics of neutron stars. In contrast to radio pulsars, the pulsed light from these objects is understood to arise from on or near the surface of the neutron star, and so it provides a direct probe of the neutron star's gravitational field. Moreover, their short rotation periods imply relativistic velocities at the equator. The possibility of determining the neutron star mass and radius using the observed phase-resolved flux from these systems offers a potential route to constraining the state of matter in neutron star cores. The main result of this work is that the rapid rotation of neutron stars in millisecond-period X-ray pulsars has important consequences for models of the pulsed emission, and by extension, the analysis of observations of these objects. We have argued in this dissertation that the most useful models of millisecond-period pulsed emission will account for the phase-dependent times-of-flight of photons from the star to the observer, and the rotation-induced "flattening" of rapidly rotating neutron stars. Of these effects, the former is accounted for more often than the latter, although neither consideration is universally applied to treatments of this problem, and it is important to understand what impacts this might have in applications of these models to data.

The structure of rapidly rotating neutron stars and the spacetimes they inhabit are not well-approximated by their static and spherically symmetric counterparts. Furthermore, precise descriptions of the situation, both interior and exterior to

the star, are only known numerically. The reduced symmetry requires that the light rays joining the star and the observer are described in more generality than is commonly seen in the literature (Chapter 2). In the spherically symmetric case, obtaining a definite description of these rays requires only the numerical inversion of a straightforward quadrature. In contrast, the more general situation requires much more computational work (Chapter 3).

Using observations of these new systems to make statements about neutron star parameters, such as mass and radius, involves finding the best fit of a calculable model of the pulsed emission to data. This is the basic methodology followed in work on classical X-ray pulsars (e.g., Leahy (2004b)), and more recently, attempts have been made to apply similar techniques with some corrections to account for the speed of these objects (Poutanen and Gierliński, 2003; Bhattacharyya *et al.*, 2005). Finding the best fit model will typically involve many evaluations of the model over a region of its parameter space, and so from a practical point of view, it is best to use a model of the pulsed emission which is quickly computed. A formally correct pulse profile model would be cumbersome for this purpose, because a general step in the parameter space will typically require a solution of the field equations for the model corresponding to the new parameter values.

After implementing a computer code to calculate the pulsed emission from the surface of a neutron star in the context of realistic stellar structure and precisely-solved spacetime metric, we investigated the extent to which one could interpret these light curves using a least-squares fitting method which compared our synthetic "data" with approximate, but easily evaluated pulse profiles for a spherical star and the Schwarzschild spacetime metric (Chapter 4). Such a procedure is analogous to methods that have recently appeared in the literature with application to observational data. The goal was to investigate how successful such a procedure would be in an idealised situation where there was no random noise added to the signal.

First, we considered the question of fitting using light curves which additionally ignore the variation in the photon times-of-flight, which may be at the level of several tens of microseconds (representing up to about 5% of a rotation period). We also restricted ourselves to the worst-case situation, where both the observer and emission are in the equatorial plane. For 300 and 600 Hz models, for both soft and stiff equations of state, large errors at the level of tens of percent were found for the obtained fitted values of M and R, although the fitted value M/R was within less than 10% of the true values in 3 of the 4 cases we tried. The most problematic

case was also the largest star.

Our next experiment was similar, except we did not restrict ourselves to the equatorial plane. We generated synthetic data for fitting using the full calculation, and to these we fit a light curve calculated using the formula for the Schwarzschild case with all time-of-flight effects included. We found that it was difficult to obtain reliable results for M or R individually when $\Omega_\star \gtrsim 200\,\mathrm{Hz}$.

Future directions

Using fitted models of stellar oblateness

By comparing pulse profiles calculated using various approximations, we found that stellar oblateness can have a significant impact on the resulting pulse shape, and that this was often more significant than the choice of exterior metric (whether Schwarzschild, Kerr, or exact). This is surprising, because generally there is more focus in the literature on using rotating metrics in this kind of calculation than in using improved descriptions of the stellar structure.

At the end of Chapter 4, it was shown that in an approximate way, one can escape the necessity of computing stellar models to obtain a description of oblateness. This addresses the importance of efficient calculations for the purpose of calculating the forward problem during fitting. We exhibited a simple polynomial which captures the oblateness of a wide range of models for three equations of state spanning a range of stiffness. There is still work to do on this, because we only examined a limited number of candidate equations of state, and have not shown that all other reasonable equations of state yield models that are well-approximated by the same polynomial. We also showed that in principle it would be possible to take this polynomial model and use it to correct the basic Schwarzschild calculation of the light curve for oblateness. Since this was only demonstrated by inserting a correction factor one expects to enter the expression, it still remains to treat the problem carefully and properly account for the changed visibility of these polynomial oblateness models in the context of the basic Schwarzschild formalism.

We have demonstrated that there is a level of error introduced when millisecond-period pulsar data are analysed from the point of view of spherical stars and the Schwarzschild metric. A thorough treatment of the idea at the end of Chapter 4 may lead to a *practical* way to incorporate the effect of rotation on stellar structure in such analyses.

Computer code improvements

During the development of the general computer code that was used to calculate the pulse profiles in the precise spacetime, we initially took the view that it was best to perform the calculation using formulas that expressed what an observer would measure if they had knowledge of the light rays which extended from them to the visible part of the star. Our motivation was to leave out formulas and assumptions that may only be valid for a spherical star in the Schwarzschild metric. For example, the projection of a two-dimensional emission region onto the observer's sky was calculated in terms of the angle formed between pairs of light rays received by an observer (Section 2.4.1). With four rays extending from the corners of a small quadrilateral on the surface of the star to the observer, the area of the quadrilateral projected onto the observer's sky could be calculated (Figure 2.2). We also argued in Section 2.4.2 that, similar to the case in special relativity (Penrose, 1959; Terrell, 1959), the motion of the emitting region impacts the visible portion of the emitting region at an instant of observer time. The emitting region will appear to be stretched by an amount related to the rate of change of the photon times-of-flight. The importance of this effect in the context of X-ray pulsars has been pointed out by, e.g., Poutanen and Gierliński (2003) and Viironen and Poutanen (2004).

Initially, the required term involving the derivative of the times-of-flight was only known numerically for the general case, although the additional symmetry in the Schwarzschild spacetime allows this quantity to be written down analytically (Equation 2.132 and the expressions that follow). The computer code was therefore designed to compute times-of-flight accurately enough that the derivative could be numerically calculated by finite differences, which results in long integration times. After numerical investigations, we discovered that it was generally true that a similar expression as for the Schwarzschild case holds in complete generality. This surprising *analytical* result is discussed at the end of Section 2.4.2. In principle, it might be possible to avoid the slow computation of the times-of-flight in the manner described in Section 3.2.1; certainly, the accuracy can be reduced if the analytical expression is used for the derivative rather than numerical differencing. In circumstances where rays originating from a single latitude are being considered, it might be possible to skip the time-of-flight calculation altogether in favour of using the much faster procedure used to find the initial conditions for rays linking specific star and observer coordinates (Section 3.3), and using the analytical form of the time-of-flight derivative $\mathrm{d}T/\mathrm{d}\phi = -b$ to compute their relative times-of-flight.

Additionally, it would be desirable to improve upon the described method to

compute the projection of a small emitting region onto the observer's sky. The method we used relies on accurately integrating the final values of the direction ℓ^θ of the rays reaching the observer, and accurately enough that it can be used for differencing when evaluating the angle formed by two rays at the observer (see Equations 2.73 and 2.74). This places a practical lower limit on the size of the angular patches we used to cover the star's surface. We know that the projection of the emission region on the observer's sky should be $\sim \cos(\alpha)$, if α is the angle formed between the emitted ray and the normal to the surface of the star, but we are missing a convincing argument that this is identically true in general. If this quantity could be generally written down in terms of only the locations of the emission region and observer, and the initial conditions for the ray, additional efficiencies can be realised. Nevertheless, the method we used agrees well with an independent analytical treatment of the problem for the Schwarzschild scenario and was seen to have the expected behaviour (Section 3.5.2).

Finally, it may also be desirable to incorporate elements present in more realistic models of the pulsed emission and to depart from our idealisation of bolometric flux from an infinitesimal, isotropic emitting region. Such enhancements would include allowing for multi-component emission spectra, different detector energy bands, and extended emission regions on the surface. These problems were not considered in depth since we wished to isolate the fundamental issues arising from rapid rotation.

Realising these future goals and improvements would require significant time. The route we took to obtain a means to consider the implications of rapid rotation on pulse profile models of millisecond X-ray pulsars was testable in many respects and led to interesting conclusions which are understandable in simple terms and indicate a need to account for effects unique to this relatively young category of objects.

References

Alpar, M. A., A. F. Cheng, M. A. Ruderman, and J. Shaham, 1982, Nature **300**, 728.

Andersson, N., 1998, Astrophys. J. **502**, 708.

Andersson, N., K. Kokkotas, and B. F. Schutz, 1999, Astrophys. J. **510**, 846.

Arnett, W. D., and R. L. Bowers, 1977, Astrophys. J. Supp. Ser. **33**, 415.

Baade, W., and F. Zwicky, 1934, Phys. Rev. **45**, 138, abstract #38 in the Proceedings of the American Physical Society for the meeting at Stanford, 15–16 December 1933.

Backer, D. C., S. R. Kulkarni, C. Heiles, M. M. Davis, and W. M. Goss, 1982, Nature **300**, 615.

Baez, J., 2000, The virial theorem made easy, Online article at `http://math.ucr.edu/home/baez/virial.html`.

Balbus, S. A., and J. F. Hawley, 1991, Astrophys. J. **376**, 214.

Balbus, S. A., and J. F. Hawley, 1998, Rev. Mod. Phys. **70**, 1.

Barcons, X., and I. Negueruela, 2003, Boletín Sociedad Española de Astronomía (10), 21.

Barret, D., J.-F. Olive, and M. C. Miller, 2006, Mon. Not. R. Astron. Soc. **370**, 1140.

Belian, R. D., J. P. Conner, and W. D. Evans, 1976, Astrophys. J. **206**, L135.

Beloborodov, A. M., 2002, Astrophys. J. **566**, L85.

Bhattacharya, D., 1995, in *X-ray binaries*, edited by W. H. G. Lewin, J. van Paradijs, and E. P. J. van den Heuvel (Cambridge University Press), volume 26 of *Cambridge Astrophysics Series*, chapter 5, pp. 175–232.

Bhattacharya, D., 2002, J. Astrophys. Astr. **23**, 67.

Bhattacharya, D., and G. Srinivasan, 1995, in *X-ray binaries*, edited by W. H. G. Lewin, J. van Paradijs, and E. P. J. van den Heuvel (Cambridge University Press), volume 26 of *Cambridge Astrophysics Series*, chapter 12, pp. 495–522.

Bhattacharyya, S., D. Bhattacharya, and A. V. Thampan, 2001, Mon. Not. R. Astron. Soc. **325**, 989.

Bhattacharyya, S., T. E. Strohmayer, M. C. Miller, and C. B. Markwardt, 2005, Astrophys. J. **619**, 483.

Bildsten, L., 1998, Astrophys. J. **501**, L89.

Binney, J., and S. Tremaine, 1987, *Galactic Dynamics* (Princeton University Press).

Bisnovatyi-Kogan, G. S., and B. V. Komberg, 1974, Sov. Astr. **18**, 217.

Boriakoff, V., R. Buccheri, and F. Fauci, 1983, Nature **304**, 417.

Boyer, R. H., and R. W. Lindquist, 1967, J. Math. Phys. **8**(2), 265.

Bradt, H., R. E. Rothschild, and J. H. Swank, 1993, Astron. Astrophys. Suppl. Ser. **97**, 355.

Braje, T. M., and R. W. Romani, 2001, Astrophys. J. **550**, 392.

Braje, T. M., R. W. Romani, and K. P. Rauch, 2000, Astrophys. J. **531**(1), 447.

Butterworth, E. M., and J. R. Ipser, 1976, Astrophys. J. **204**, 200.

Cadeau, C., D. A. Leahy, and S. M. Morsink, 2005, Astrophys. J. **618**, 451.

Cadeau, C., S. M. Morsink, D. A. Leahy, and S. S. Campbell, 2006, Light curves for rapidly-rotating neutron stars, Astrophys. J., accepted. Available as astro-ph/0609325.

Campbell, S., 2003, *Photon propagation near rapidly-rotating neutron stars*, Master's thesis, University of Alberta.

Canal, R., J. Isern, and J. Labay, 1990, Ann. Rev. Astron. Astrophys. **28**, 183.

Canal, R., and E. Schatzman, 1976, Astron. Astrophys. **46**, 229.

Carter, B., 1968, Phys. Rev. **174**(5), 1559.

Chadwick, J., 1932, Nature **129**, 312.

Chakrabarty, D., 2005, in *Binary Radio Pulsars*, edited by F. A. Rasio and I. H. Stairs (Astronomical Society of the Pacific), volume 328, p. 279, available as astro-ph/0408004.

Chakrabarty, D., and E. H. Morgan, 1998, Nature **394**, 346.

Chang, P., S. Morsink, L. Bildsten, and I. Wasserman, 2006, Astrophys. J. **636**, L117.

Chen, K., and J. Shaham, 1989, Astrophys. J. **339**, 279.

Clark, G. W., 1975, Astrophys. J. **199**, L143.

Clausius, R., 1870, Ann. Phys. Lpz. **141**, 124.

Cook, G. B., S. L. Shapiro, and S. A. Teukolsky, 1992, Astrophys. J. **398**, 203.

Cook, G. B., S. L. Shapiro, and S. A. Teukolsky, 1994a, Astrophys. J. **424**, 823.

Cook, G. B., S. L. Shapiro, and S. A. Teukolsky, 1994b, Astrophys. J. **422**, 227.

Cook, G. B., S. L. Shapiro, and S. A. Teukolsky, 1994c, Astrophys. J. **423**, L117.

Cornelisse, R., J. Heise, E. Kuulkers, F. Verbunt, and J. J. M. in't Zand, 2000, Astron. Astrophys. **357**, L21.

Cottam, J., F. Paerels, and M. Méndez, 2002, Nature **420**, 51.

Cui, W., E. H. Morgan, and L. G. Titarchuk, 1998, Astrophys. J. **504**, L27.

Cumming, A., and L. Bildsten, 2000, Astrophys. J. **544**, 453.

Cumming, A., S. M. Morsink, L. Bildsten, J. L. Friedman, and D. E. Holz, 2002, Astrophys. J. **564**, 343.

Cumming, A., E. Zweibel, and L. Bildsten, 2001, Astrophys. J. **557**, 958.

Davidson, K., and J. P. Ostriker, 1973, Astrophys. J. **179**, 585.

Dirac, P. A. M., 1926, Proc. Roy. Soc. London Ser. A **112**, 661.

Eckel, B., 2000, *Thinking in C++* (Prentice-Hall), second edition, available at `http://www.BruceEckel.com`.

Eddington, A. S., 1924, Mon. Not. R. Astron. Soc. **84**, 308.

Fabian, A. C., J. E. Pringle, and M. J. Rees, 1975, Mon. Not. R. Astron. Soc. **172**, 15P.

Faulkner, J., 1971, Astrophys. J. **170**, L99.

Flannery, B. P., and E. P. J. van den Heuvel, 1975, Astron. Astrophys. **39**, 61.

Ford, E. C., 1999, Astrophys. J. **519**, L73.

Ford, E. C., 2000, Astrophys. J. **535**, L119.

Fowler, R. H., 1926, Mon. Not. R. Astron. Soc. **87**, 114.

Frank, J., A. King, and D. Raine, 2002, *Accretion Power in Astrophysics* (Cambridge University Press), third edition.

Friedman, J. L., and S. M. Morsink, 1998, Astrophys. J. **502**, 714.

Fruchter, A. S., D. R. Stinebring, and J. H. Taylor, 1988, Nature **333**, 237.

Fujimoto, M. Y., T. Hanawa, and S. Miyaji, 1981, Astrophys. J. **247**, 267.

Fushiki, I., and D. Q. Lamb, 1987, Astrophys. J. **323**, L55.

Galloway, D. K., D. Chakrabarty, E. H. Morgan, and R. A. Remillard, 2002, Astrophys. J. **576**, L137.

Galloway, D. K., C. B. Markwardt, E. H. Morgan, D. Chakrabarty, and T. E. Strohmayer, 2005, Astrophys. J. **622**, L45.

Gammel, B. M., 2005, Matpack C++ Numerics and Graphics Library, available at `http://www.matpack.de`.

Ghisellini, G., 1999, Special relativity at action in the universe, pre-print astro-ph/9905181. Invited paper at the XIII national meeting on General Relativity (SIGRAV).

Ghosh, P., and F. K. Lamb, 1978, Astrophys. J. **223**, L83.

Giacconi, R., H. Gursky, E. Kellogg, E. Schreier, and H. Tananbaum, 1971, Astrophys. J. **167**, L67.

Gibson, W., 1984, *Neuromancer* (The Berkley Publishing Group, New York, USA), chapter 4, p. 68, quotation on frontispiece from Ace Books paperback edition, 24th printing.

Gierliński, M., C. Done, and D. Barret, 2002, Mon. Not. R. Astron. Soc. **331**, 141.

Glendenning, N. K., 2000, *Compact stars: nuclear physics, particle physics, and general relativity*, Astronomy and Astrophysics Library (Springer-Verlag, New York), second edition.

Gold, T., 1968, Nature **218**, 731.

Goldstein, H., 1950, *Classical Mechanics* (Addison-Wesley, Reading, Massachusetts, USA).

Grindlay, J. E., H. Gursky, H. Schnopper, D. R. Parsignault, J. Heise, A. C. Brinkman, and J. Schrijver, 1976, Astrophys. J. **205**, L127.

Gunn, J. E., and J. P. Ostriker, 1969, Astrophys. J. **157**, 1395.

Gunn, J. E., and J. P. Ostriker, 1970, Astrophys. J. **160**, 979.

Haensel, P., and A.-Y. Potekhin, 2004, Astron. Astrophys. **428**, 191.

Hansen, C. J., and H. M. van Horn, 1975, Astrophys. J. **195**, 735.

Hawley, J. F., and J. H. Krolik, 2001, Astrophys. J. **548**, 348.

Heindl, W. A., R. E. Rothschild, W. Coburn, R. Staubert, J. Wilms, I. Kreykenbohm, and P. Kretschmar, 2004, in *X-ray Timing 2003: Rossi and Beyond*, edited by P. Kaaret, F. K. Lamb, and J. H. Swank (American Institute of Physics, Melville, New York, USA), volume 714 of *AIP Conf. Proc.*, available as astro-ph/0403197.

Hessels, J. W. T., S. M. Ransom, I. H. Stairs, P. C. C. Freire, V. M. Kaspi, and F. Camilo, 2006, Science **311**(5769), 1901.

Hewish, A., S. J. Bell, J. D. H. Pilkington, P. F. Scott, and R. A. Collins, 1968, Nature **217**, 709.

Heyl, J. S., 2002, Astrophys. J. **574**, L57.

Heyl, J. S., 2004, Astrophys. J. **600**, 939.

Hills, J., 1983, Astrophys. J. **267**, 322.

Hirose, S., J. H. Krolik, and J. M. Stone, 2006, Astrophys. J. **604**, 901.

Hulse, R. A., and J. H. Taylor, 1975, Astrophys. J. **195**, L51.

Ibrahim, A. I., S. Safi-Harb, J. H. Swank, W. Parke, S. Zane, and R. Turolla, 2002, Astrophys. J. **574**, L51.

Illarionov, A. F., and R. A. Sunyaev, 1975, Astron. Astrophys. **39**, 185.

in 't Zand, J. J. M., J. Heise, J. M. Muller, A. Bazzano, M. Cocchi, L. Natalucci, and P. Ubertini, 1998, Astron. Astrophys. **331**, L25.

Israel, W., 1968, Nature **218**, 755.

Jacoby, B. A., A. Hotan, M. Bailes, S. Ord, and S. R. Kulkarni, 2005, Astrophys. J. **629**, L113.

Jahoda, K., J. H. Swank, A. B. Giles, M. J. Stark, T. Strohmayer, W. Zhang, and E. H. Morgan, 1996, in *Proc SPIE: EUV, X-Ray, and Gamma-Ray Instrumentation for Astronomy VII*, edited by O. H. Siegmund and M. A. Gummin (International Society for Optical Engineering), volume 2808, pp. 59–70.

Joss, P. C., and F. K. Li, 1980, Astrophys. J. **238**, 287.

Kaaret, P., E. H. Morgan, R. Vanderspek, and J. A. Tomsick, 2006, Astrophys. J. **638**, 963.

Kalogera, V., and R. F. Webbink, 1998, Astrophys. J. **493**, 351.

Kapoor, R. C., 1991, Astrophys. J. **378**, 227.

Kapoor, R. C., and B. Datta, 1986, Astrophys. J. **311**, 680.

King, A., 1995, in *X-ray binaries*, edited by W. H. G. Lewin, J. van Paradijs, and E. P. J. van den Heuvel (Cambridge University Press), volume 26 of *Cambridge Astrophysics Series*, chapter 10, pp. 419–456.

King, A. R., 2006, in *Compact Stellar X-Ray Sources*, edited by W. H. G. Lewin and M. van der Klis (Cambridge University Press), volume 39 of *Cambridge Astrophysics Series*, chapter 13, preprint available as astro-ph/0301118.

Komatsu, H., Y. Eriguchi, and I. Hachisu, 1989, Mon. Not. R. Astron. Soc. **237**, 355.

Kraus, U., 2001, Astrophys. J. **563**, 289.

Kraus, U., C. Zahn, C. Weth, and H. Ruder, 2003, Astrophys. J. **590**, 424.

Krolik, J. H., and J. F. Hawley, 2002, Astrophys. J. **573**, 754.

Kuulkers, E., P. R. den Hartog, J. J. M. in't Zand, F. W. M. Verbunt, W. E. Harris, and M. Cocchi, 2003, Astron. Astrophys. **399**, 663.

Lattimer, J. M., and M. Prakash, 2001, Astrophys. J. **550**, 426.

Lattimer, J. M., and M. Prakash, 2004, Science **304**, 536.

Leahy, D. A., 1990, Mon. Not. R. Astron. Soc. **242**, 188.

Leahy, D. A., 1991, Mon. Not. R. Astron. Soc. **251**, 203.

Leahy, D. A., 2003a, Astrophys. J. **596**(2), 1131.

Leahy, D. A., 2003b, Pulse shape model with Doppler effects, private communication.

Leahy, D. A., 2004a, Mon. Not. R. Astron. Soc. **348**(3), 932.

Leahy, D. A., 2004b, Astrophys. J. **613**(1), 517.

Leahy, D. A., 2005, Email regarding fit results, private communication.

Leahy, D. A., W. Darbro, R. F. Elsner, M. C. Weisskopf, S. Kahn, P. G. Sutherland, and J. E. Grindlay, 1983, Astrophys. J. **266**, 160.

Leahy, D. A., and L. Li, 1995, Mon. Not. R. Astron. Soc. **277**, 1177.

Lewin, W. H. G., J. van Paradijs, and R. E. Taam, 1995, in *X-ray binaries*, edited by W. H. G. Lewin, J. van Paradijs, and E. P. J. van den Heuvel (Cambridge University Press), volume 26 of *Cambridge Astrophysics Series*, chapter 4, pp. 175–232.

Lorimer, D. R., 2005, Living Rev. Relativity **8**, URL (cited on 1 May 2006): `http://www.livingreviews.org/lrr-2005-7`.

Ludlam, T., and L. McLerran, 2003, Physics Today **56**, 48, available at `http://www.physicstoday.org/vol-56/iss-10/p48.html`.

Lynden-Bell, D., and J. E. Pringle, 1974, Mon. Not. R. Astron. Soc. **168**, 603.

Markwardt, C. B., M. Juda, and J. H. Swank, 2003a, XTE J1807-294 — precise position and orbit determination, ATEL #127.

Markwardt, C. B., E. Smith, and J. H. Swank, 2003b, Discovery of a fourth accreting millisecond pulsar, XTE J1807-294, ATEL #122.

Markwardt, C. B., T. E. Strohmayer, and J. H. Swank, 2003c, Revised orbit and burst oscillations from the millisecond pulsar XTE J1814-338, ATEL #164.

Markwardt, C. B., and J. H. Swank, 2003, IAUC #8144.

Markwardt, C. B., J. H. Swank, and T. E. Strohmayer, 2004, IGR J00291+5934 is a 598 Hz X-ray pulsar, ATEL #353.

Markwardt, C. B., J. H. Swank, T. E. Strohmayer, J. J. M. in 't Zand, and F. E. Marshall, 2002, Astrophys. J. **575**, L21.

McMillan, S. L. W., P. N. McDermott, and R. E. Taam, 1987, Astrophys. J. **318**, 261.

Méndez, M., M. van der Klis, and E. C. Ford, 2001, Astrophys. J. **561**, 1016.

Mereghetti, S., and J. E. Grindlay, 1987, Astrophys. J. **312**, 727.

Mészáros, P., and W. Nagel, 1985, Astrophys. J. **299**, 138.

Mészáros, P., and H. Riffert, 1988, Astrophys. J. **327**, 712.

Miller, K. A., and J. M. Stone, 2000, Astrophys. J. **534**, 398.

Miller, M. C., and F. K. Lamb, 1998, Astrophys. J. **499**, L37.

Miller, M. C., F. K. Lamb, and D. Psaltis, 1998, Astrophys. J. **508**, 791.

Misner, C. W., K. S. Thorne, and J. A. Wheeler, 1973, *Gravitation* (W. H. Freeman and Company).

Morsink, S., 2000, Science **290**(5493), 945.

Morsink, S. M., 2005a, Modified version of rns code, equil.c, private communication.

Morsink, S. M., 2005b, Photon deflection & TOA, private communication.

Muno, M. P., 2002, *Millisecond oscillations during thermonuclear X-ray bursts*, Ph.D. thesis, Massachusetts Institute of Technology.

Muno, M. P., D. Chakrabarty, D. K. Galloway, and D. Psaltis, 2002a, Astrophys. J. **580**, 1048.

Muno, M. P., D. W. Fox, E. H. Morgan, and L. Bildsten, 2000, Astrophys. J. **542**, 1016.

Muno, M. P., F. Özel, and D. Chakrabarty, 2002b, Astrophys. J. **581**, 550.

Nagel, W., 1981, Astrophys. J. **251**, 278.

Nath, N. R., T. E. Strohmayer, and J. H. Swank, 2002, Astrophys. J. **564**, 353.

Nice, D. J., E. M. Splaver, I. H. Stairs, O. Löhmer, A. Jessner, M. Kramer, and J. M. Cordes, 2005, Astrophys. J. **634**, 1242.

Nollert, H.-P., H. Ruder, H. Herold, and U. Kraus, 1989, Astron. Astrophys. **208**, 153.

Novikov, I. D., and Y. B. Zel'dovich, 1966, Nuovo Cimento **4**, 810.

Oppenheimer, J. R., and G. M. Volkoff, 1939, Phys. Rev. **55**(4), 374.

Ostriker, J. P., 1976, in *Structure and Evolution of Close Binary Systems*, edited by P. P. Eggleton et al. (Reidel, Dordrecht), p. 206.

Pacini, F., 1968, Nature **219**, 145.

Paczyński, B., 1976, in *Structure and Evolution of Close Binary Systems*, edited by P. P. Eggleton et al. (Reidel, Dordrecht), p. 75.

Paczyński, B., 1983, Nature **304**, 421.

Papitto, A., M. T. Menna, L. Burderi, T. Di Salvo, F. D'Antona, and N. R. Robba, 2005, Astrophys. J. **621**, L113.

Pechenick, K. R., C. Ftaclas, and J. M. Cohen, 1983, Astrophys. J. **274**, 846.

Penrose, R., 1959, Proc. Cambridge Phil. Soc. **55**, 137.

Poutanen, J., and M. Gierliński, 2003, Mon. Not. R. Astron. Soc. **343**, 1301.

Press, W. H., S. A. Teukolsky, W. T. Vetterling, and B. P. Flannery, 1988, *Numerical Recipes in C: the art of scientific computing* (Cambridge University Press, Cambridge), second edition.

Psaltis, D., 2006, in *Compact Stellar X-Ray Sources*, edited by W. H. G. Lewin and M. van der Klis (Cambridge University Press), volume 39 of *Cambridge Astrophysics Series*, chapter 1, preprint available as astro-ph/0410536.

Psaltis, D., and D. Chakrabarty, 1999, Astrophys. J. **521**, 332.

Ray, A., A. K. Kembhavi, and H. M. Antia, 1987, Astron. Astrophys. **184**, 164.

Renka, R. J., 1988, Transactions on Mathematical Software **14**(2), 149, Algorithm 660.

Riffert, H., and P. Mészáros, 1988, Astrophys. J. **325**, 207.

Romanova, M. M., A. Kulkarni, M. Long, R. V. E. Lovelace, J. V. Wick, G. V. Ustyugova, and A. V. Koldoba, 2006, Advances in Space Research **38**, 2887.

Rybicki, G. B., and A. P. Lightman, 1979, *Radiative processes in astrophysics* (Wiley, New York).

Salpeter, E. E., 1964, Astrophys. J. **140**, 796.

Saslaw, W. C., 1985, *Gravitational physics of stellar and galactic systems* (Cambridge University Press).

Savonije, G. J., 1983, Nature **304**, 422.

Schiffer, J. P., S. M. Austin, G. A. Baym, T. W. Donnelly, B. Filippone, S. Freedman, W. C. Haxton, W. F. Henning, N. Isgur, B. Jacak, W. Nazarewicz, V. R. Pandharipande, *et al.*, 1999, *Nuclear Physics: The Core of Matter, The Fuel of Stars* (National Academy Press, Washington, D.C., USA).

Schwarzschild, M., and R. Härm, 1965, Astrophys. J. **142**, 855.

Scott, D. M., D. A. Leahy, and R. B. Wilson, 2000, Astrophys. J. **539**, 392.

Shakura, N. I., and R. A. Sunyaev, 1973, Astron. Astrophys. **24**, 337.

Shapiro, S. L., and S. A. Teukolsky, 1983, *Black holes, white dwarfs, and neutron stars* (John Wiley & Sons, Inc.).

Shepard, D., 1968, in *Proceedings of the 1968 23rd ACM national conference*, ACM (Association for Computing Machinery) (ACM Press, New York, NY, USA), pp. 517–524.

Shklovskii, I., 1967, Astrophys. J. **148**, L1.

Shu, F. H., 1991, *The physics of astrophysics*, volume 1 (University Science Books, Mill Valley, California, USA).

Smarr, L. L., and R. D. Blandford, 1976, Astrophys. J. **207**, 574.

Spergel, D. N., R. Bean, O. Doré, M. R. Nolta, C. L. Bennett, G. Hinshaw, N. Jarosik, E. Komatsu, L. Page, H. V. Peiris, L. Verde, C. Barnes, *et al.*, 2006, Wilkinson Microwave Anisotropy Probe (WMAP) three year results: Implications for cosmology, Astrophys. J., submitted. Available as astro-ph/0603449.

Spitkovsky, A., Y. Levin, and G. Ushomirsky, 2002, Astrophys. J. **566**, 1018.

Stergioulas, N., 2003, Living Rev. Relativity **6**, URL (cited on 3 July 2006): `http://www.livingreviews.org/lrr-2003-3`.

Stergioulas, N., and J. L. Friedman, 1995, Astrophys. J. **444**, 306, the RNS code is available at `http://www.gravity.uwm.edu/rns`.

Strohmayer, T. E., and L. Bildsten, 2006, in *Compact Stellar X-Ray Sources*, edited by W. H. G. Lewin and M. van der Klis (Cambridge University Press), volume 39 of *Cambridge Astrophysics Series*, chapter 3, preprint available as astro-ph/0301544.

Strohmayer, T. E., K. Jahoda, A. B. Giles, and U. Lee, 1997, Astrophys. J. **486**, 355.

Strohmayer, T. E., and U. Lee, 1996, Astrophys. J. **467**, 773.

Strohmayer, T. E., and C. B. Markwardt, 1999, Astrophys. J. **516**, L81.

Strohmayer, T. E., W. Zhang, J. H. Swank, A. Smale, L. Titarchuk, and C. Day, 1996, Astrophys. J. **469**, L9.

Stroustrup, B., 1997, *The C++ Programming Language* (Addison-Wesley), third edition.

Sunyaev, R. A., and L. G. Titarchuk, 1980, Astron. Astrophys. **86**, 121.

Sutantyo, W., 1975, Astron. Astrophys. **44**, 227.

Tananbaum, H., H. Gursky, E. M. Kellogg, R. Levinson, E. Schreier, and R. Giacconi, 1972, Astrophys. J. **174**, L143.

Tauris, T. M., and G. J. Savonije, 1999, Astron. Astrophys. **350**, 928.

Tauris, T. M., and R. J. Takens, 1998, Astron. Astrophys. **330**, 1047.

Tauris, T. M., and E. P. J. van den Heuvel, 2006, in *Compact Stellar X-Ray Sources*, edited by W. H. G. Lewin and M. van der Klis (Cambridge University Press), volume 39 of *Cambridge Astrophysics Series*, chapter 16, preprint available as astro-ph/0303456.

Terrell, J., 1959, Phys. Rev. **116**(4), 1041.

Thorsett, S. E., and D. Chakrabarty, 1999, Astrophys. J. **512**, 288.

Urpin, V., and U. Geppert, 1995, Mon. Not. R. Astron. Soc. **275**, 1117.

Urpin, V., U. Geppert, and D. Konenkov, 1998, Astron. Astrophys. **331**, 244.

van der Klis, M., 1995, in *X-ray binaries*, edited by W. H. G. Lewin, J. van Paradijs, and E. P. J. van den Heuvel (Cambridge University Press), volume 26 of *Cambridge Astrophysics Series*, chapter 6, pp. 252–307.

van der Klis, M., 2006, in *Compact Stellar X-Ray Sources*, edited by W. H. G. Lewin and M. van der Klis (Cambridge University Press), volume 39 of *Cambridge Astrophysics Series*, chapter 2, preprint available as astro-ph/0410551.

van Paradijs, J., 1978, Nature **274**, 650.

van Paradijs, J., 1979, Astrophys. J. **234**, 609.

van Paradijs, J., and W. H. G. Lewin, 1987, Astron. Astrophys. **172**, L20.

Vaughan, B. A., M. van der Klis, K. S. Wood, J. P. Norris, P. Hertz, P. F. Michelson, J. van Paradijs, W. H. G. Lewin, K. Mitsuda, and W. Penninx, 1994, Astrophys. J. **435**, 362.

Verbunt, F., 1988, in *The Physics of Compact Objects*, edited by N. E. White and L. Fillipov (Pergamon Press, Oxford), p. 529.

Verbunt, F., 1993, Annu. Rev. Astron. Astrophys. **31**, 93.

Verbunt, F., and W. H. G. Lewin, 2006, in *Compact Stellar X-Ray Sources*, edited by W. H. G. Lewin and M. van der Klis (Cambridge University Press), volume 39 of *Cambridge Astrophysics Series*, chapter 8, preprint available as astro-ph/0404136.

Verbunt, F., and E. P. J. van den Heuvel, 1995, in *X-ray binaries*, edited by W. H. G. Lewin, J. van Paradijs, and E. P. J. van den Heuvel (Cambridge University Press), volume 26 of *Cambridge Astrophysics Series*, chapter 11, pp. 457–494.

Viironen, K., and J. Poutanen, 2004, Astron. Astrophys. **426**, 985.

Wang, Y. M., and G. L. Welter, 1981, Astron. Astrophys. **102**, 97.

Weinberg, N., M. C. Miller, and D. Q. Lamb, 2001, Astrophys. J. **546**, 1098.

Whelan, J., and I. Iben, 1973, Astrophys. J. **186**, 1007.

White, N. E., F. Nagase, and A. N. Parmar, 1995, in *X-ray binaries*, edited by W. H. G. Lewin, J. van Paradijs, and E. P. J. van den Heuvel (Cambridge University Press), volume 26 of *Cambridge Astrophysics Series*, chapter 1, pp. 1–57.

Wijnands, R., and M. van der Klis, 1998, Nature **394**, 344.

Williams, T., and C. Kelley, 2004, The Gnuplot Plotting Utility, available at `http://sourceforge.net/projects/gnuplot/files`.

Wood, K. S., J. P. Norris, P. Hertz, B. A. Vaughan, P. F. Michelson, K. Mitsuda, W. H. G. Lewin, J. van Paradijs, W. Penninx, and M. van der Klis, 1991, Astrophys. J. **379**, 295.

Zane, S., and R. Turolla, 2005, Advances in Space Research **35**, 1162.

Zavlin, V. E., G. G. Pavlov, Y. A. Shibanov, and J. Ventura, 1995, Astron. Astrophys. **297**, 441.

Zel'dovich, Y. B., 1964, Sov. Phys. Doklady **9**, 195.

Zel'dovich, Y. B., and O. H. Guseynov, 1966, Astrophys. J. **144**, L840.

Zel'dovich, Y. B., and I. D. Novikov, 1964, Doklady Academii Nauk SSSR **158**(4), 811, english translation: 1965, Sov. Phys. Dokl., **9**, 834.